2017

Printable Carbon Nanotube Based Multifunctional Nanocomposites for Strain Sensing and Self-heating

Xin Wang
University of Central Florida

PRINTABLE CARBON NANOTUBE BASED MULTIFUNCTIONAL NANOCOMPOSITES FOR STRAIN SENSING AND SELF-HEATING

by

XIN WANG
B.S. Donghua University, 2012
M.S. University of Central Florida, 2014

A dissertation submitted in partial fulfillment of the requirements
for the degree of Doctor of Philosophy
in the Department of Materials Science and Engineering
in the College of Engineering and Computer Sciences
at the University of Central Florida
Orlando, Florida

Summer Term
2017

Major Professor: Jihua Gou

ABSTRACT

The unique properties of carbon nanotubes (CNTs) represent a potential for developing a piezo-resistive strain sensor and a resistive heating sheet with a smart structure. Conventional fabrication techniques of CNT based nanocomposites such as molding, casting or spray coating lack the ability to control the geometry and properties of fabricated composites. In order to meet the various requirements of strain sensing or self-heating applications, nanocomposites with complex geometry and controllable properties are in high demand. Digital printing technique is able to fabricate CNT films with precisely controlled geometry with the help of computer aided design, and their properties could also be controlled by adjusting the printing parameters. The objective of this study is to investigate the printing-structure-property relationship of CNT based multifunctional nanocomposites fabricated by digitally controlled spray deposition process for strain sensing and self-heating. A spray deposition modeling (SDM) printer that uses a 12-array inkjet nozzle attached to an x-y plotter was developed for the fabrication of CNT layers.

Most of previously-reported CNT based nanocomposite strain sensors only have limited stretchability and sensitivity for measuring diverse human motions. Additionally, strain sensors fabricated by traditional techniques are only capable of measuring strain in a single direction, but for monitoring human motion with complicated strain condition, strain sensors that can measure strain from multi-direction are favorable. In this dissertation, highly stretchable (in excess of 45% strain) and sensitive (gauge factor of 35.75) strain sensors with tunable strain gauge factors were fabricated by incorporating CNT layers into polymer substrate using SDM printing technique. The cyclic loading-unloading test results revealed that the composite strain sensors exhibited excellent long-term durability. Due to the flexibility of the printing technique, rosette-typed sensors were

fabricated to monitor complicated human motions. These superior sensing capabilities of the fabricated nanocomposites offer potential applications in wearable strain sensors.

Resistive heating properties of CNT based nanocomposites were also investigated. The electrically resistive heating of these composites can be a desirable stimulus to activate the shape memory effect of polymer matrix. CNT based nanocomposites fabricated by traditional techniques showed a slow heating rate and same shape recovery ratio at different locations in nanocomposites. However, from the practical applications like smart skin or smart tooling perspective, programmable shape recovery ratio at specified locations are desirable. In this dissertation, the CNT based nanocomposites with a fast heating rate and controllable maximum surface temperature were fabricated using SDM technique. The study on the shape memory effect of nanocomposites showed that their shape recoverability was approximately 100% taking 30s under a low voltage of 40V. It is worth noting that through programming the number of printed CNT layers at different locations, the shape recovery rate could be controlled and localized actuation with the desired recovery ratio was achieved. The high efficiency of heating coupling with wide adjustability of surface temperature and shape recovery ratio at specified locations make the fabricated nanocomposites a promising candidate for electrical actuation applications.

ACKNOWLEDGMENTS

First and foremost, I would like to express my sincere gratitude to my academic advisor, Dr. Jihua Gou, for his guidance, encouragement, and patience through five years of study at University of Central Florida (UCF). I'm extremely grateful that he has provided the great opportunity to join the top level research group. This dissertation would not have been possible without his guidance and support. I have received many insightful suggestions from him. I would also like to express my appreciation to my PhD committee members, Dr. Olusegun Ilegbusi, Dr. Yuanli Bai, Dr. Hyoung Jin Cho and Dr. Nina Orlovskaya for providing valuable comments and suggestions on different aspects of my dissertation and for their cooperation in a different field assignment. I would also like to extend my thanks to those who offered collegiate guidance and support over the years, Dr. Yuanli Bai, Dr. Yunjun Xu, Dr. Olusegun Ilegbusi, Dr. Helen Huang and Dr. Haibao Lv. Without them, many experiments of this dissertation could have been impossible.

I am also indebted to the members of Composites Materials and Structure Lab, with whom I have interacted during my graduate studies. I would like to thank Dr. Fei Liang and Dr. Jason Gibson for their help during the beginning of my work. They provide me a lot of foundational knowledge in my research fields. Particularly I would like to acknowledge John Sparkman, our lab manager, for the assistance of all related machine design and materials testing. I am grateful for all of my colleagues' contributions to my work. Thank you, Donovan Lui and Hongjiang Yang. Thanks to Jeffery Gambrell and Amy Callaghan for their initial design of the deposition machine.

Furthermore, my gratitude is also extended to Mr. Kirk Scammon, staff of Materials Characterization Facility, for the help on materials characterization. I would be remiss if I did not

thank Jeanine Clements, who deserves credit for providing needed assistance with administrative tasks.

For the ancestors who paved the path before me upon whose shoulders I stand. This is dedicated to my family and many friends who supported me on this memorable journey. Thank you.

TABLE OF CONTENTS

LIST OF FIGURES

LIST OF TABLES

CHAPTER ONE: INTRODUCTION

1.1. Motivation

Carbon Nanotube(CNT) is described as a graphene sheet that has been rolled to form CNT[1]. The Young's modulus of multi-walled carbon nanotubes is estimated to be 1.28TPa[2]. The thermal conductivity along the axis of SWCNTs is about $3500W^{-1}mK^{-1}$[3] and the electrical conductivity along their axis is in the range of $1.0x10^6$ to $3x10^6$ S/m[4]. Due to their excellent mechanical, thermal and electrical properties (as shown in Table 1), CNTs have attracted great attention in both academic and industrial field. Polymer matrix composites could combine the matrix and reinforcements to achieve a system with more useful structural or functional properties non attainable by any of the constituent alone[5].

Table 1. Carbon nanotube properties comparison to properties of other materials

Materials	Specific density	Young's modulus(TPa)	Strength (GPa)	Thermal Conductivity (W/mK)	Electrical Conductivity(S/m)
Carbon Nanotube	1-2	1	10-60	3500	10^6-10^7
HS-Steel	7.8	0.2	4.1	54	7 x 10^6
Carbon Fiber	1.7-2	0.2-0.6	1.7-5	1000	2-5 x 10^6
Aluminum	2.7	0.07	0.3	230	3.5 x 10^7

Incorporation of CNT reinforcements into polymers permits the fabrication of polymer matrix composites with by high mechanical performance and excellent functionality. For example, the electrical characteristic of CNTs coupled with their high mechanical strength makes them a

promising material for strain sensors. Piezo-resistive strain sensors are an interesting area of industrial and academic research due to the growing demand for flexible and wearable electronics [6-9], smart textiles [10] and structural health monitoring [11]. Carbon nanotube reinforced polymer composites have also attracted extensive attentions for their potential application as an electrical heater due to their light weight, oxidization resistance, low manufacturing cost and high energy efficiency [12-17]. Incorporating CNTs into shape memory polymers (SMPs) can also make them into conductive composites and the electrically resistive heating of these composites can be a desirable stimulus to activate their shape memory effect without an external heater.

Conventional fabrication techniques of composites such as molding, casting and machining create polymer composites with complex geometry through material removal processes[18]. While the manufacturing process and performance of composites in these methods are well-controlled and understood, the ability to control the geometry and properties of fabricated composites is limited. Digital printing technique is able to fabricate complex composite structures without the typical waste. The size and geometry of composites can be precisely controlled with the help of computer aided design. Additionally, the properties could also be controlled and adjusted due to the flexibility of digital printing process.

Therefore, the motivation of this study is to fabricate CNT based polymer nanocomposites through digital printing technique, study the processing-structure-property-performance relationship of carbon nanotube based nanocomposites multifunctional application and eventually improve the functional performance of CNT based nanocomposites by optimizing the processing parameter and materials design.

1.2. Research Method

The methodology behind this research consists of the incorporating of CNTs into various polymeric matrix by digital printing technique. CNT layers were printed on polymer substrates first to prepare the nanocomposites. The strain sensing and resistive heating properties of fabricated polymer nanocomposites were investigated.

In this research, multi-walled carbon nanotubes were introduced to thermoplastic polyurethane resin, PDMS and shape memory polyurethane by a home-made spray deposition modeling printing technique. Traditionally, researchers fabricated CNT composites by directly mixing CNT into polymer matrix. However, CNT have strong tendency to aggregate to form bundles because of their high aspect ratio and strong Van der Waals interaction among CNTs. It is very difficult to uniformly disperse CNTs into polymer matrix, especially for high loading of CNTs (>10wt%) in composites. To overcome dispersion problem, CNT layers were printed on polymer substrate for high density CNT networks. Good dispersion and dense packing of carbon nanotube in polymer matrix can be realized by fabricating CNT layers first.

Nowadays, all the fabrication methods of carbon nanotube films are not able to create the desired sensing or heating geometry. This study developed a spray deposition modeling method that are able to produce carbon nanotube film based nanocomposite for sensing and seld-heating. The spray deposition modeling technique is a digital fabrication process that uses evaporative techniques to disperse the nanomaterials in a defined location. This process has the ability to produce carbon nanotube films with controlled pattern on variable substrates.

This research study focuses on examining the manufacturing process and resulting performance of carbon nanotube film based nanocomposites. High sensitivity carbon nanotube strain sensors with

wide sensing strain scale will be fabricated. Spray deposition modeling digital processing ensures the created strain sensor is geometrically accurate. This process is also additive, which enables the strain sensor to be built layer by layer and has minimum loss of the supplied material. The effectiveness of fabricated MWCNTs as strain sensors will be measured by investigating real-time strain response of MWCNTs sensors under tensile load. On the mircro-scale, we will use scanning electron microscope imaging to evaluate the crack morphology of CNT based strain sensors. Multi-directional strain sensors will also be investigated in the future. Self-heating behavior of carbon nanotube films based nanocomposite will be investigated too. The electrical resistivity determining the heat produced with the addition of voltage will be measured through four point probe resistivity test. Electrical heating performance will be measured by the maximum surface temperature and heating rate of carbon nanotube films based nanocomposites under varied voltage. Potential application such as the precise heating control of the actuation of shape memory polymer in each location, deicing and nanocomposites with thermal gradient will be explored in the future.

1.3. Structure of the Dissertation

The main body of the dissertation from Chapter 2 to Chapter 6 is organized by the following sequence. Chapter 2 reviews the typical CNT film processing approaches, the research and development of the CNT reinforced polymer composites as strain sensors and electric heating element, and the electrical actuation of CNT reinforced shape memory composites. In Chapter 3, the discussion focuses on the processing of CNT reinforced nanocomposites, namely, how to print CNT on various substrate with homemade spray deposition modeling equipment. The strain sensing properties of CNT/Polyurethane nanocomposites were investigated and discussed in

Chapter 4. Different types of substrates were used to fabricate strain sensors with optimized sensing properties. The sensing properties of strain sensors with PDMS substrate were discussed in Chapter 5. Chapters 6 focused on the resistive heating properties of CNT/polyurethane nanocomposites. Chapter 7 focuses on the electrical actuation of CNT based shape memory nanocomposites. The shape recovery ratio and shape recovery speed were evaluated. Especially, due to the flexibility of printing technique, honeycomb structured shape memory nanocomposites were also fabricated and investigated. The dissertation ends in Chapter 8, where conclusion and future improvement are proposed.

CHAPTER TWO: LITERATURE REVIEWS

2.1. Digital Fabrication of Polymer Matrix Nanocomposites

Digital printing, also referred to as additive manufacturing(AM), rapid prototyping(RP), or solid-freeform(SFF), is the 'process of joining materials to make objects from 2D/3D model data, usually layer by layer'[19], which was first described in 1986 by Charles Hull[20]. This technology creates objects by adding materials to reduce waste while reaching satisfactory geometric accuracy[21]. It begins with a meshed computer model that can be created by acquired image data or structures built in computer-aided design (CAD) software.

Digital printing of polymer composites has found their possible applications in aerospace industries for creating complex lightweight structures[22], architectural industries for structural models[23], art fields for artifact replication or education[24], and medical fields for printing tissues and organs[25]. Conventional fabrication techniques of composites such as molding, casting and machining create products with complex geometry through material removal processes[18]. While the manufacturing process and performance of composites in these methods are well-controlled and understood, the ability to control the complex internal structure is limited. Digital printing is able to fabricate complex composite structures without the typical waste. The size and geometry of composites can be precisely controlled with the help of computer aided design. Thus, digital printing of composites attains an excellent combination of process flexibility and high performance products.

Digital printing is a methodology that produces 3D haptic physical models layer by layer based on CAD models[26]. Various printing techniques have been employed to fabricate polymer composites. Among them, some techniques are well-established, such as fused deposition

modeling, selective laser sintering, inkjet 3D printing, stereolithography and 3D plotting whereas others are still in development or used only by small groups of researchers. Each technique has its own advantages and limitations in producing composite products. The selection of fabrication technique depends on the starting materials, requirements of processing speed and resolution, costs and performance requirements of final products.

2.1.1 Fused deposition modeling(FDM)

Fused deposition modeling(FDM) printers are the most commonly used printer for fabricating polymer composites. Thermoplastics such as PC, ABS and PLA, are commonly used due to their low melting temperature. FDM printers work by controlled extrusion of thermoplastic filaments, as shown in Figure 1(a). In FDM, filaments melt into a semi-liquid state at nozzle and are extruded layer by layer onto the build platform where layers are fused together and then solidify into final parts. The quality of printed parts can be controlled by altering printing parameters, such as layer thickness, printing orientation, raster width, raster angle and air gap. The effect of processing parameters have been discussed by Sood et al.[27].

One common drawback of FDM printing is that the composite materials have to be in a filament form to enable the extrusion process. It is difficult to homogeneously disperse reinforcements and remove the void formed during the manufacturing of composite filaments. Another disadvantage of FDM printers is that the usable material is limited to thermoplastic polymers with suitable melt viscosity. The molten viscosity should be high enough to provide structural support and low enough to enable extrusion. Also, complete removal of the support structure used during printing may be difficult. Notwithstanding these drawbacks, FDM printers also offer advantages, including low cost, high speed and simplicity. Another advantage of FDM printing is the potential to allow

deposition of diverse materials simultaneously. Multiple extrusion nozzles with loading of different materials can be set up in FDM printers, so printed parts can be multi-functional with designed composition.

2.1.2 Powder bed and inkjet head 3D printing(3DP)

Powder-liquid 3D printing technology was developed at the Massachusetts Institute of Technology (MIT) in 1993 as a rapid-prototyping technology[28]. This technology is based on powder processing, as shown in Figure 1(b). Powders are first spread on the build platform and then selectively joined into a patterned layer by depositing a liquid binder through inkjet printhead, which is able to move in X-Y direction. After a desired 2D pattern is formed, the platform lowers and the next layer of powder is spread. This process is repeated and finally unbounded powder should be removed to get final products. The internal structure can be controlled by altering the amount of deposited binder. Factors that determine the quality of final products are powder size, binder viscosity, interaction between binder and powder, and the binder deposition speed. The effect of processing parameters has been discussed in detail in a review by Ben et al.[29].

The key advantages of this technology are the flexibility of material selections and room temperature processing environment. Theoretically, any polymer materials in powder state could be printed by this technology. Removal of support structure is also relatively easy with this technique. However, the binder used may incorporate other contaminations and the printing resolution is very limited for this technology.

2.1.3 Stereolithography(SLA)

Stereolithography uses photopolymers that can be cured by UV laser. An UV-laser is controlled in a desired path to shoot in the resin reservoir, and the photocurable resin will polymerize into a

2D patterned layer. After each layer is cured, the platform lowers and another layer of uncured resin is ready to be patterned[30], as shown in Figure 1(c). Typical polymer materials used in SLA are acrylic and epoxy resins.

Understanding the curing reactions occurring during polymerization is critical to control the quality of final printed parts. Intensity of laser power, scan speed and duration of exposure affect the curing time and printing resolution[31]. Photoinitiators and UV absorbers can be added to the resin to control the depth of polymerization[32]. The main advantage of SLA printing technology is the ability to print parts with high resolution. Additionally, because SLA is a nozzle-free technique, the problem of nozzle clogging can be avoided. Despite these advantages, the high cost of this system is a main concern for industrial application. Possible cytotoxicity of residual photoinitiator and uncured resin is another concern.

2.1.4 Selective laser sintering(SLS)

Selective laser sintering technique is similar to previously mentioned 3DP technique and they are both based on powder processing. Instead of using a liquid binder, in SLS, a laser beam with a controlled path scans the powders to sinter them by heating, as shown in Figure 1(d). Under high power lasers, neighboring powders are fused together through molecular diffusion and then processing of next layer starts. Unbounded powder should be removed to get final products[33]. The feature resolution is determined by powder particle size, laser power, scan spacing and scan speed[34].

Although theoretically any thermoplastic polymer in powder form could be processed by SLS technique, the complex consolidation behavior and molecular diffusion process during sintering

have limited the choice of materials used in SLS process[35]. To the date now, polycaprolactone(PCL) and polyamide(PA) are widely used laser sintering materials.

2.1.5 3D plotting/Direct-Write

3D plotting is based on extruding a viscous material from a pressurized syringe to create 3D shape of materials, as shown in Figure 1(e). The syringe head can move in three dimensions, while the platform keeps stationary where extruded materials are joint together layer by layer. Curing reactions can be performed by dispensing two reactive components using mixing nozzles or be induced either by heat or UV light[36]. In certain cases, materials can be delivered to a plotting medium to finish the curing reaction. Material viscosity and deposition speed correlate with the quality of final printed parts[25].

The key advantage of this technique is material flexibility. Solution, paste and hydrogels can all be loaded into 3D plotting printers. A temporary, sacrificial material may be needed to support the printed structure since raw viscous materials have low stiffness that may result in the collapse of complex structures.

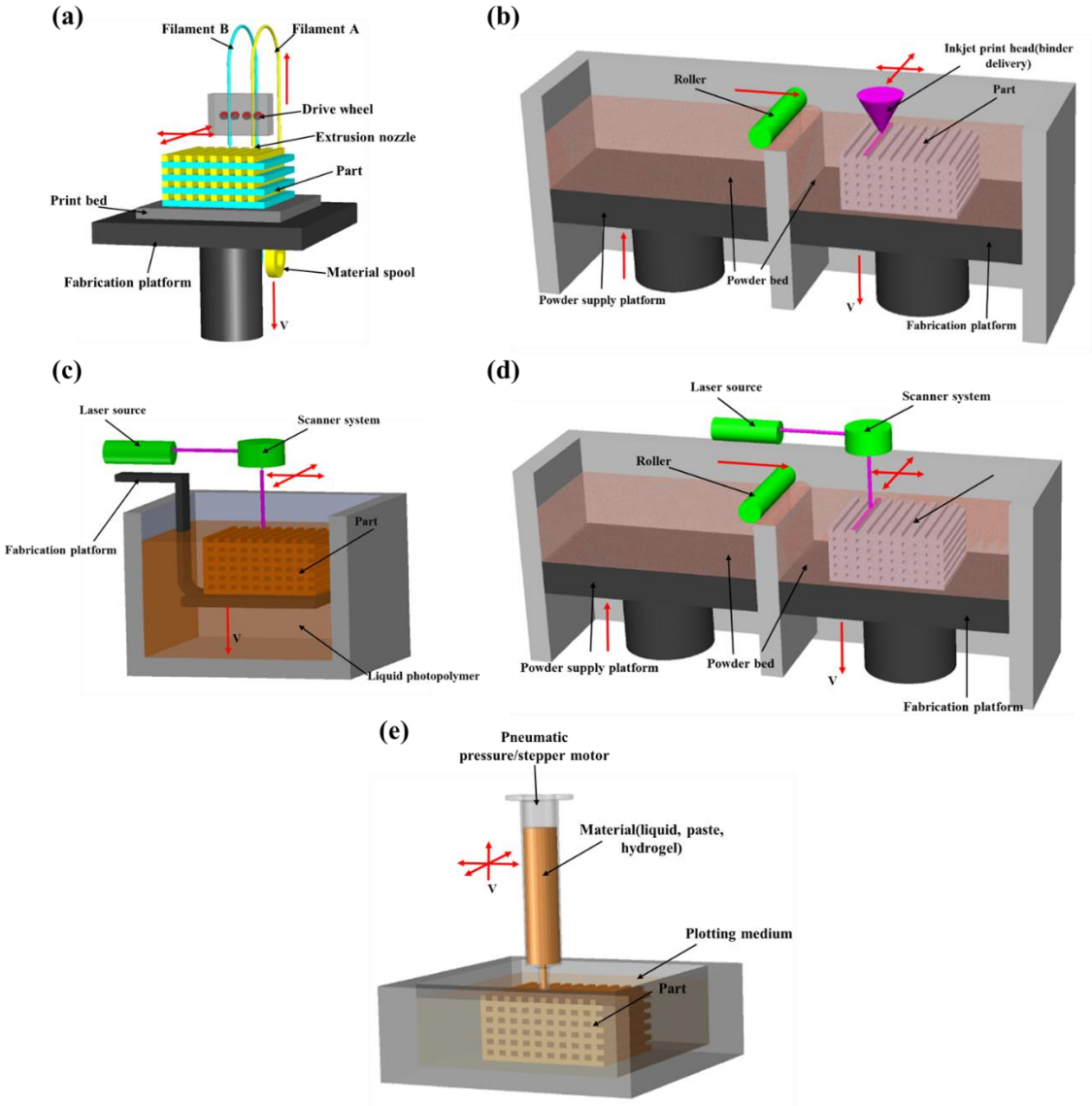

Figure 1. Schematic representation of a typical (a) FDM setup (b) 3DP setup (c) SLA setup (d) SLS setup (e) 3D plotting setup.

Nanomaterials such as carbon nanotube[37-39], graphene[40, 41], graphite[41, 42], ceramic[43, 44] and metal nanoparticle[45, 46] often exhibit unique mechanical, electrical and thermal properties. Thus, the addition of nanomaterials into polymers for printing could enable the creation of high-performance functional composites.

Nanomaterials have been utilized for improving the mechanical properties of printed composite parts. The addition of 5wt% nano-titanium dioxide(TiO_2)[47], 10wt% carbon nanofiber[48] or 10wt% multi-walled carbon nanotube[49] showed a 13.2%, 39% and 7.5% increase in the tensile strength of printed composite parts compared with unfilled polymer parts, respectively, but all printed composite parts showed reduced elongation and more brittle feature. Lin et al.[50]demonstrated a SLA fabricated graphene oxide/photopolymer composites with a good combination of increased strength and increased ductility. Their specimens showed a 62.2% increasing of tensile strength and a 12.8% increasing of elongation with only 0.2% GOs. The authors claimed that the increased ductility was due to the increasing in crystallinity of graphene oxide in reinforced polymers. Except for the mechanical properties improvement, enhanced electrical properties could be obtained by the addition of carbon-based nanomaterials like carbon nanotube[51, 52], carbon nanofiber[53], carbon-black[54] and graphene[55]. Wei et al. [55]demonstrated for the first time, a graphene reinforced ABS composite could be FDM printed into computer-designed models and the enhanced electrical conductivity was observed. With the loading of 5.6wt% graphene, the electrical conductivity of ABS nanocomposites showed four orders of magnitude improvement. Furthermore, incorporation of nano-TiO_2[56] and nano-clay[57] into polymer matrix could greatly improve the thermal stability of printed nanocomposites. In another study, He et al.[58] produced a thermoelectric composite by blending $Bi_{0.5}Sb_{1.5}Te_3$(BST) into photoresins using SLA process, and the resulting composites exhibited an ultralow thermal conductivity of 0.2 $Wm^{-1}K^{-1}$, which is favorable for thermoelectric applications.

2.2. Fabrication of Carbon Nanotube Films

Carbon nanotube films are made from the entangled and aggregated carbon nanotubes. The generally accepted way of making CNT films is vacuum filtration method. In vacuum filtration method, CNTs were usually dispersed in solution with the aid of surfactant by ultrasonication. These CNT suspensions can then be filtered through different membranes under pressure to yield uniform CNT films with entangled carbon nanotubes network[59]. This method is regarded as a simple process for the fabrication of ultrathin, transparent, optically homogeneous, electrically conducting films composed of pure CNTs. An alternative to vacuum infiltration is pressure filtration. The mechanism of pressure filtration is pretty similar with vacuum infiltration. Pressure is applied instead of vacuum. However, these two techniques both use surfactant that is difficult to remove after processing, which may decrease the performance of CNT films. Another novel technology to get rid of surfactant is frit compression method[60]. Using this way, the adverse side-effects from the surfactants can be avoided, but the thickness of CNT films are typically much larger than that of CNT films made through filtration method. Generally, the CNT films made from frit compression method have thickness range from 120um to 650um. ‘Domino pushing’ technique is another simple and effective method to manipulate aligned CNT arrays into CNT films[61]. This technique can efficiently ensure that most of CNTs are well aligned tightly in the films. The technique mentioned above are usually used for fabrication of thick carbon nanotube films and it is difficult to precise control the thickness of CNT films through these technique. Figure 2 shows a schematic of each fabrication method.

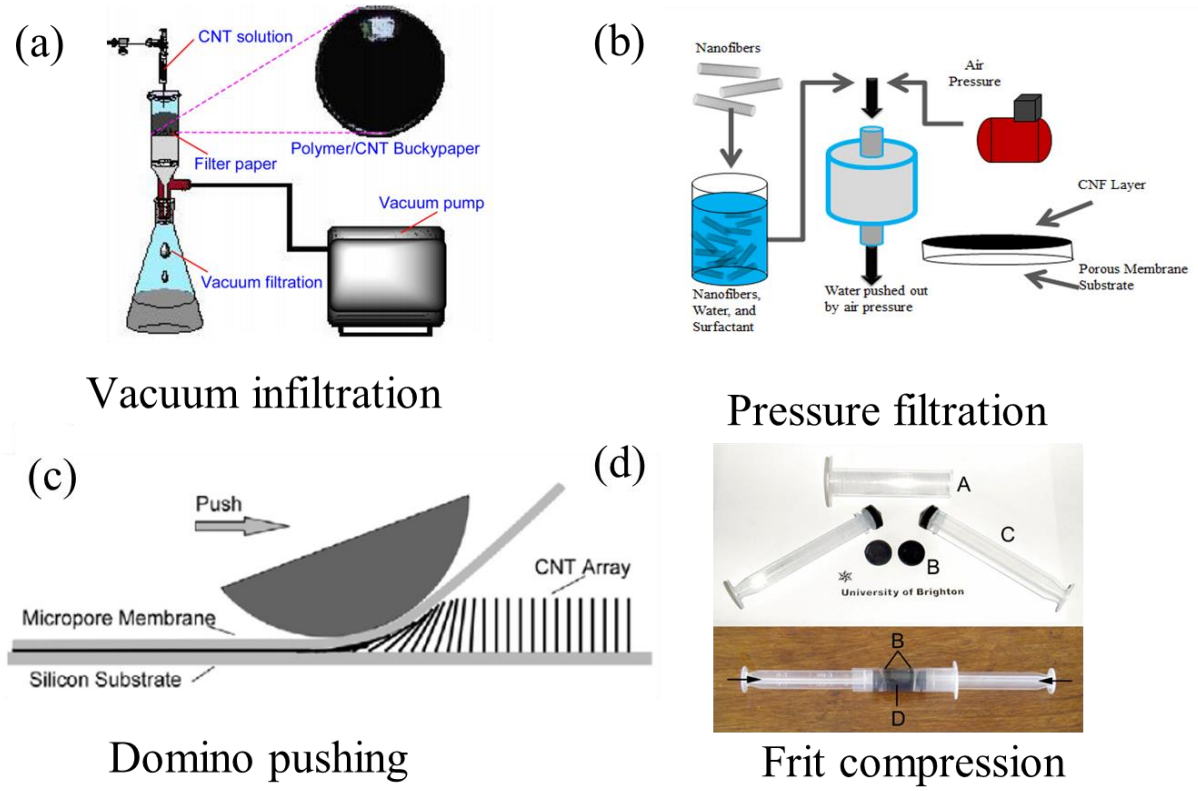

Figure 2. Depiction of various CNT films fabrication method (a) Vacuum infiltration[59]; (b) Pressure filtration; (c) Domino pushing[61]; (d) Frit compression[60].

Most technique for fabrication of CNT thin films are solution-based. The prepared CNT suspensions will then be deposited on to a substrate. A method called 'Langmuir Blodgett(LB)' is based on the hydrophobic behavior of CNTs[62]. Firstly, CNTs spread on the surface of water and then deposition can be achieved through a horizontal lifting or a vertical dipping method. It is a slow process, so that it is only suitable for fabrication of monolayers or submonolayers CNT films. Spin coating is another way to fabricate CNT thin films. A small amount of solutions is dropped onto a substrate followed by high-speed spinning of the substrate[63]. CNT films made by spin coating method have very precisely controlled thickness. However, spin coating is a method with

high cost and it is difficult to be scaled up. Electrophoretic deposition has also been used to deposit CNT films on conductive substrate[63]. EPD is fundamentally a combination of two processes, electrophoresis and deposition. In the first step, particles suspended in a liquid are forced to move toward an electrode by applying an electric field. In the second step, the particles collect at the electrode and form a coherent deposited film. This process allows continuous production of CNT thin films and the typical deposition time is only a few seconds, but the substrate must be conductive, which is the biggest limitation. Spray coating is a simple and quick method to make CNT films[64]. Typically, the CNT suspensions are sprayed onto a heated substrate. The set temperature for the substrate is adjusted by the choice of solvent. By using diluted solution and multiple spray coating steps, homogeneous films can be obtained. For many application, non-solution based technique are required. CNT film transfer is a good technique[65]. CNT films could be transferred to a target substrate, and during the transfer step, patterning could also be done. Pressure, heat and laser could be used to help the transfer of CNT films.

Digital fabrication is a common work used to describe CNC machine that is based off of MIT's 1952 numerically controlled mill[66]. These machines usages range from large to small and cover many different areas. The digital fabrication techniques allow researcher to produce CNT films with different patterns and the geometry accuracy of CNT films are improved. Screen-printing could be used to digital fabricate CNT films[67]. It is a printing technique whereby a mesh is used to transfer ink onto a substrate and a blade is moved across the screen to fill the open mesh apertures with ink. Screen printing of CNT films can have large scale mass production of highly reproducible and mechanical stable. Despite their promising performance, this technique pose several fabrication challenge. For instance, mask and blade need to be used in screen printing, so

it is a contact technique which may bring contamination. In additional, the manufacturing of masks may increase the overall cost and limits the scalability of this process.

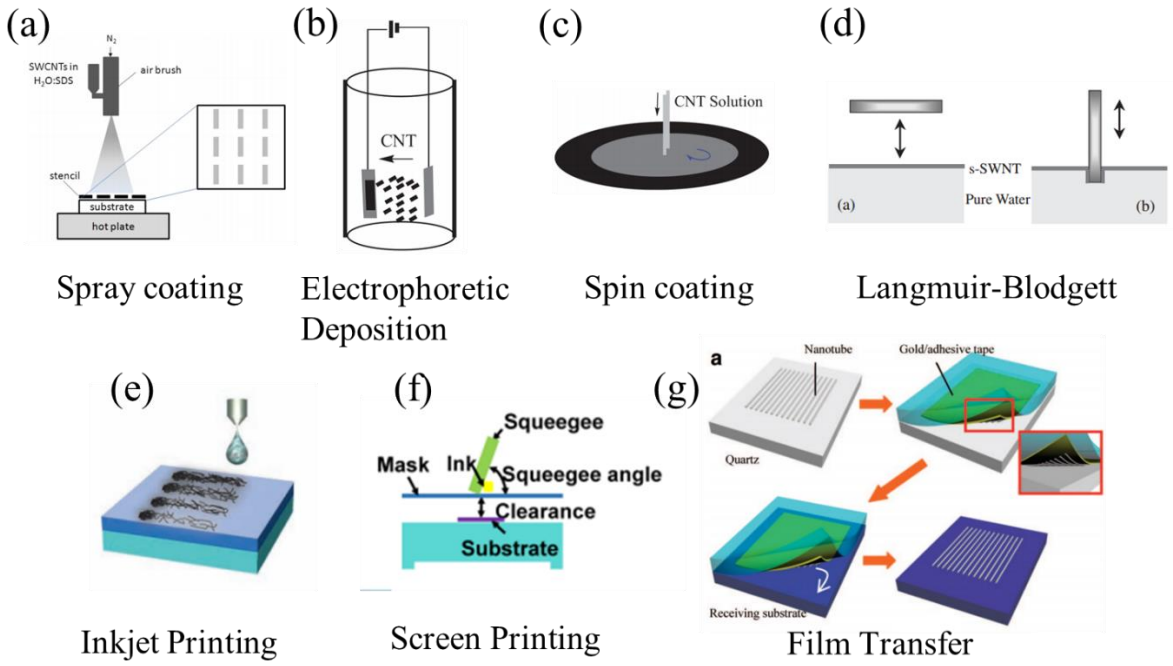

Figure 3. Depiction of various CNT thin films fabrication method. (a) Spray coating[64]; (b) Electrophoretic deposition[63]; (c) Spin coating[63]; (d) Langmuir-Blodgett[62]; (e) Inkjet printing[68] (f) Screen printing[67] (g) Film transfer[65].

Inkjet printing is also a popular technique due to its ability to print fine and easily controllable patterns, noncontact, solution saving and scalability[68]. It is a type of printing that recreates a digital image by propelling droplets of ink on to variable substrate. Based on different printing nozzles, inkjet printer can be split into two categories, namely thermal and piezoelectric[69]. Thermal inkjet printers, sometimes referred to bubble jet printers, contain a thin film resistor in the nozzle. In order to eject a droplet, this thin film resistor is heated by passing current through it. This causes the ink in the nozzle to vaporize, creating a bubble and a large increase in pressure,

which forces ink droplets out of the nozzle. Piezoelectric inkjet printers contain a piezoelectric transducer in the nozzle. When voltage is applied to the piezoelectric transducer, it deforms and causes an increase in pressure, which forces ink droplets out of the nozzle. The difficulty of inkjet printing is the formulating of ink. It is difficult to uniform disperse the carbon nanotube within the ink. In addition, the ink must maintain a low surface tension as well as a low viscosity.

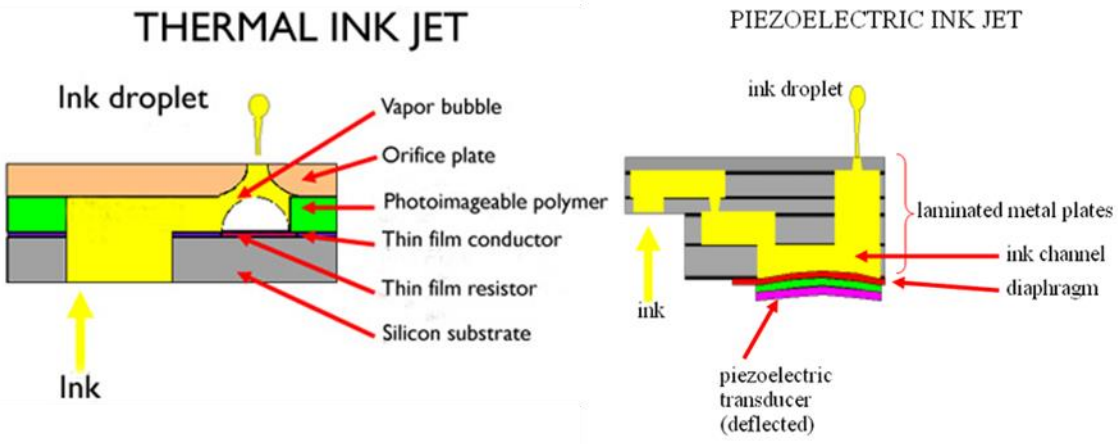

Figure 4. Depiction of two types of inkjet printing head

2.3. Carbon Nanotube Based Strain Sensors

In recent years, mechanical structures are designed with lighter materials and more slender shapes, which brings a huge saving in materials cost. However, when long-time subjected to high stress, these progressive designed mechanical structures have higher tendency to encounter cracking and failure. In order to improve the safety level of mechanical structures, structural health monitoring(SHM) has become a very important research field.

CNTs have been considered as a promising candidate for strain sensors, due to their dependence of electrical properties on mechanical deformation[70]. In CNT strain sensors, there is a reversible

correlation between the mechanical deformations and the electrical resistance, which is called piezo-resistive effect[71].

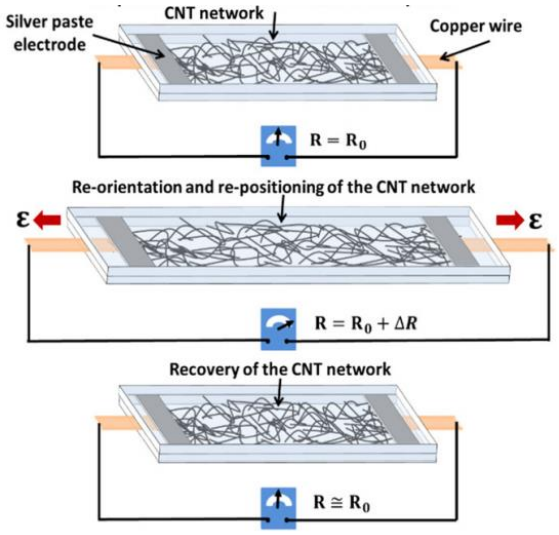

Figure 5. Structure and basic working principles of the CNT–based strain sensors [72]

Figure 5[72] illustrates the structure and basic principle of CNT-based strain sensors. When the strain sensors are stretched out, re-orientation and re-positioning of CNTs within the CNT network increases the base resistance of the strain sensors. Moreover, upon relaxation of the strain sensors, reestablishment of the CNT network inspired by the elastic force of substrate. Tradition strain sensors were fabricated through non-digital technique, such as spray coating[72] and molding[73] technique, as shown in Figure 6 and 7, which could only produce strain sensors with simple geometry. X Li et al[74] studied the capabilities of multi-walled carbon films as strain sensors. The MWCNT films were prepared by a solution/filtration method. Their results indicated that the change in resistance of the MWCNT film was proportional to the applied stain. Y Li et al[75] also investigated the piezo-resistive effect of carbon nanotube thin films. The strain gauge factor was found to be 65. Their results indicated that CNT films are potentially useful for structural health

monitoring. A novel strain sensor made of single walled carbon nanotube was developed by Dongil.Lee et al[76] through spray coating process. Their batch-fabricated SWCNT strain sensos showed the linear relationship between resistance changes and externally applied strain. The sensitivity of this strain sensor was measure to be approximately 30 times higher than that of commercial foil-type strain sensors.

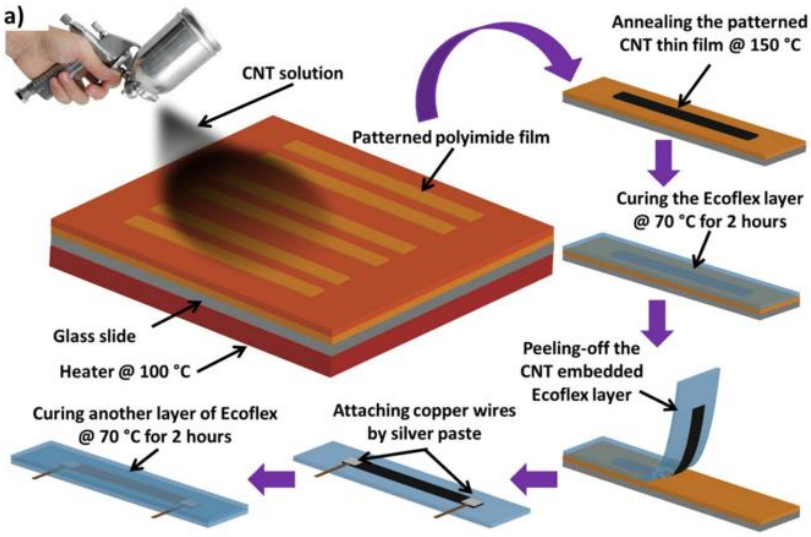

Figure 6. Spray coating fabrication of carbon nanotube based strain sensors[72]

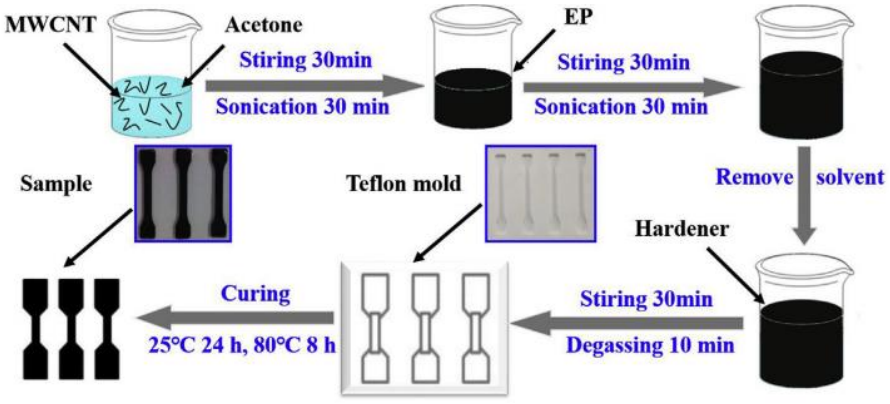

Figure 7. Molding fabrication of carbon nanotube based strain sensors[73]

Stretchable and flexible strain sensors have attracted considerable attentions for human motion analysis. Traditional metallic and semiconducting strain sensors are not suitable for stretchable applications because they can only withstand very limited strain (<5%) before fracture[77]. Today's most common approach for fabrication of highly stretchable piezoresistive strain sensors are depositing carbon nanotubes on the surface of a stretchable substrate using various methods such as contact transfer printing[6] and screen printing[78]. A simple and rapid micropatterning method for fabricating CNT-based stretchable strain sensor was proposed by Jeong-Ho Kong[79]. The piezoresistive responses of the fabricated strain sensors were revealed to be highly linear up to 10% tensile strain and fully stabilized without significant hysteretic behavior after transient cycles. Takeo Yamada[80] reported a wearable and stretchable strain sensor fabricated from thin films of aligned single-wall carbon nanotubes. When stretched, the nanotube films fracture into gaps and islands, and bundles bridging the gaps. This mechanism allows the films to act as strain sensors capable of measuring strains up to 280% (50 times more than conventional metal strain gauges), with high durability, fast response and low creep. Film transfer and embedment of carbonized patterns created through selective laser pyrolization of thermoset polymers into elastomeric substrates were employed by Rahim Rahimi to fabricate strain sensors[77]. The strain sensors were highly stretchable (up to 100% strain) and sensitive (gauge factor of up to 20 000). These strain sensors were also very stable even after 1000 load cycles.

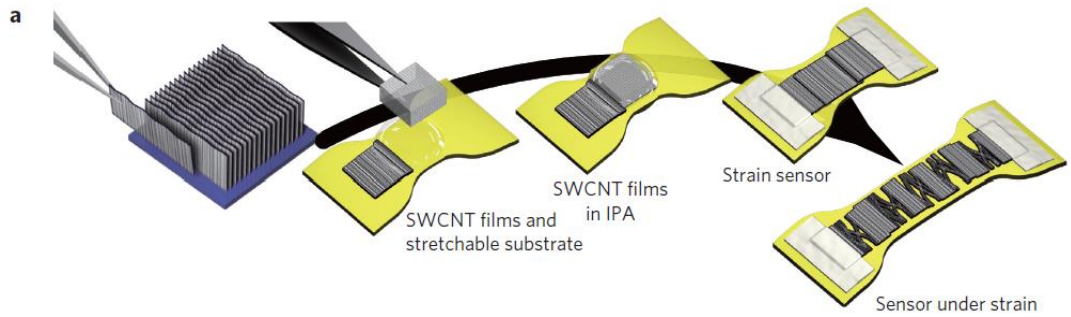

Figure 8. Key steps in fabricating the stretchable CNT strain sensor[80]

Table 1 summarized and compared the stretchability and sensitivity of previously reported strain sensors. Most of them could not have high stretchability as well as high sensitivity. Recently, several sensors have been reported with high stretchability and sensitivity, but the response time is long in these sensors[77], as shown in Figure 9. Additionally, these sensors also have hysteresis behavior[81] (Figure 10), which is not good for monitoring the human motions. Therefore, there is a high demand for developing strain sensors with high stretchability and sensitivity as well as good linearity and negligible hysteresis.

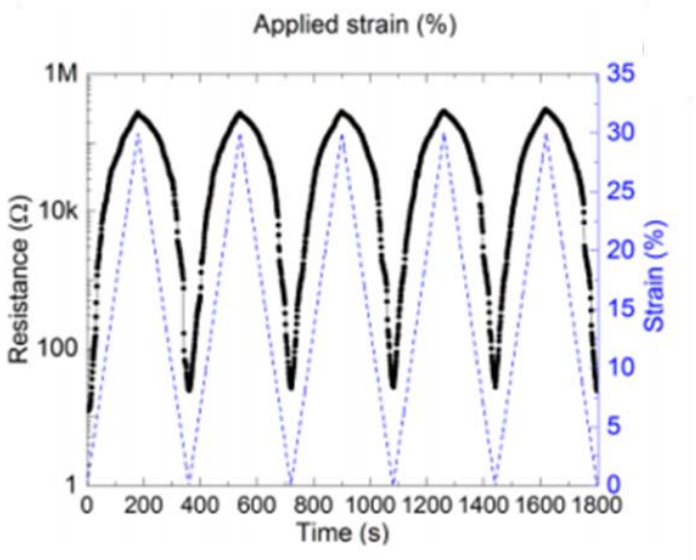

Figure 9. Response time for the fabricated strain sensors[77]

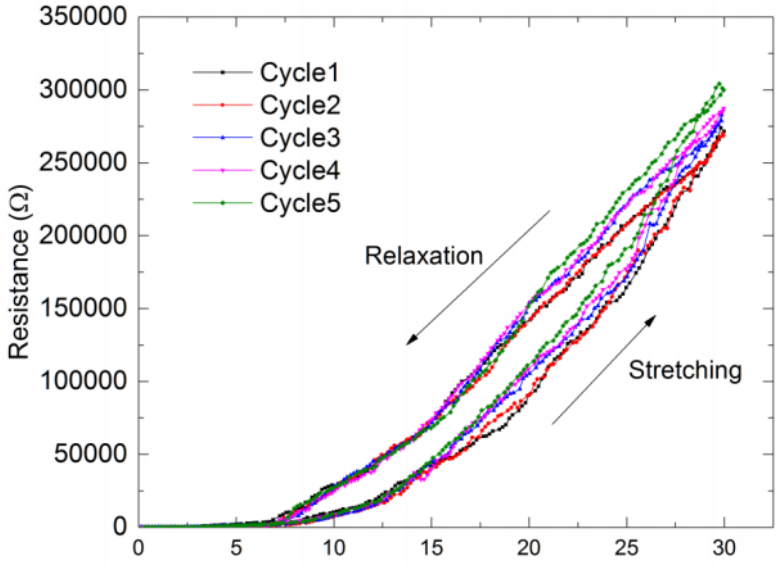

Figure 10. Hysteresis behavior of fabricated strain sensors[81]

Table 2. Previously reported carbon nanotube strain sensors

Materials	**Fabrication Method**	**Strain Level**	**Gauge Factor**	**Ref**
MWCNT/EFTE	Inkjet printing	0.4%	0.98	[82]
VACNT/PDMS	CVD deposition	0.9%	4793	[83]
MWCNT/SBS	Extrusion	20%	30	[84]
MWCNT/TPU	Casting	20%	30	[85]
MWCNT/TPU	Compression molding	30%	35	[86]
MWCNT/Ecoflex	Spray coating	100%	1.75	[72]
CNT	Film transfer	100%	20000	[77]
SWCNT/PDMS	Molding	50%	10^7	[73]

2.4. Self- Heating Properties of Carbon Nanotube Based Nanocomposites

Due to their excellent electrical properties, carbon nanotubes are used to prepare conductive polymer composites[87]. Self-heating is one of many applications for conductive polymer compoistes[12, 14]. In the case of electrical heating materials, electrical energy can be converted into heat energy through the Ohmic joule heating[88]. Usually, electrical heating elements are

made by metallic materials and used for plane heater, wire heater, water heater and so on[89]. However, metal-based electrical heating devices have several drawbacks such as easy oxidization, emission of electromagnetic wave, and high manufacturing costs. Therefore, polymer composites containing carbon nanotubes have attract interest for preparing self-heating or electrical heating materials due to their light weight, easy processing, and high energy efficiency[90]. Setsuko Isaji[14] investigated the heating performance of polyethylene/carbon nanotube composite films under electric field at constant voltage. The composite films were prepared by gelation/crystallization from dilute solution. The filler content was 10 wt% of MWNTs. When a certain voltage was applied to the composite, the surface temperature of film reaches the equilibrium value within less than 100 s. The quick heating suggested its good application to high efficient plane heater. A carbon nanotube paper based self-heating polymer composite were fabricated by Hetao Chu[15]. The electric heating performance was verified by deicing a certain amount of ice at different heat flux densities. The deicing time under the two conditions were less than 220s, as shown in Figure 11. The results indicated this material is a promising candidate as an electric heating material for deicing. Most of previously reported electrical heating sheets all have heating patterns with a very simple geometry like the rectangular shape[15, 91] (Figure 12), which is not good for meeting the various requirements. Table 3 summarized and compared the heating performance of previously reported carbon nanotube based nanocomposites.

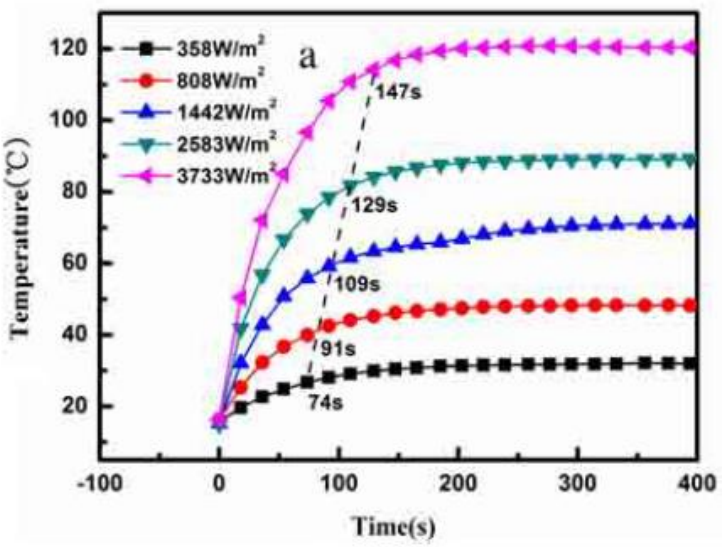

Figure 11. The electric heating process curves of the rectangle shaped CNT based composites[15]

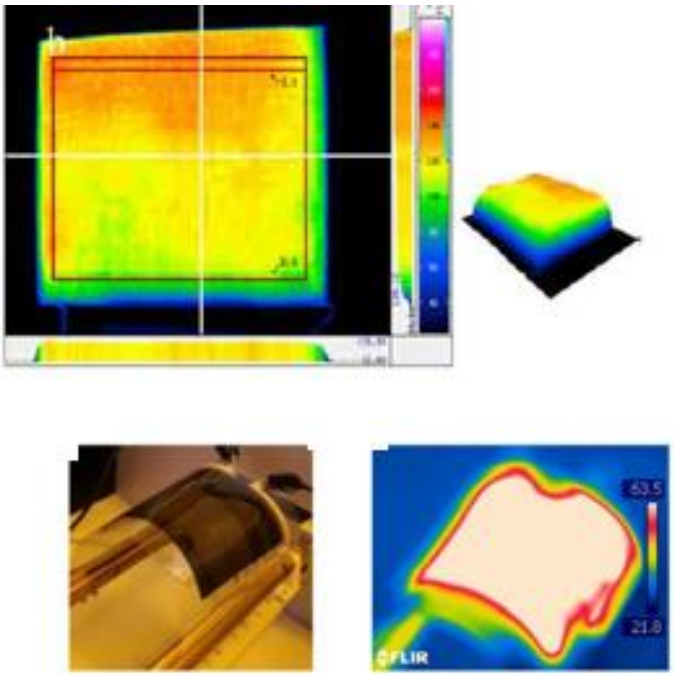

Figure 12. Heating patterns with simple rectangular shape[15, 91]

Table 3. Previously reported carbon nanotube based heating element

Materials	**Fabrication Method**	**Maximum temperature and heating rate under similar 0.2 W/cm^{2}power density**	**Ref**
MWCNT/PDMS	Solution casting	50°C in 30s	[17]
CNT/PE	Molding	Over150°C in 200s	[90]
MWCNT/Epoxy	Molding	80°C in 130s	[13]
MWCNT/Aramid	Solution Casting	150°C in 30s	[12]
MWCNT/PE	Solution Casting	50°C in 50s	[14]
MWCNT/Cellulose	Dip coating	75°C in 40s	[92]
MWCNT/PDMS	Hot press	130°C in 30s	[93]

2.5. Electrical Actuation of Carbon Nanotube/Shape Memory Polymer Nanocomposites

Carbon nanotubes can also be added into shape memory polymers to make them conductive. By applying voltage, shape memory effect of shape memory polymer can be triggered. Incorporating CNTs into shape memory polymers(SMPs) can make them into conductive composites and the

electrically resistive heating of these composites can be a desirable stimulus to activate their shape memory effect without an external heater.

Table 4. Previously reported electrical actuation of carbon nanotube based shape memory polymer composites

Materials	**Fabrication Method**	**Shape recovery ratio and time**	**Ref**
MWCNT/Epoxy	Mold casting	100% in 80s under 60V	[94]
CNT/Epoxy	Mold casting	90% in 50s under 5V	[95]
MWCNT/Epoxy	Mold casting	90% in 20s under 5V	[96]
MWCNT/PVA	Solution Casting	100% in 35s under 60V	[97]
CNT/PU	Compression molding	88% in 60s under 50V	[98]
MWCNT/PU	Solution Casting	96% in 30s under 50V	[99]
MWCNT/PBSPCL	Solution Casting	96% in 45s under 75V	[100]

As a typical smart material, SMP can be deformed into a temporary shape and then recover to its original (or permanent) shape upon exposure to the heat stimuli[101-103]. Therefore, besides acting as an electric heater, due to their superior structural versatility, CNT/SMPs can also be used in many other fields, including smart tooling[104], deployable medical device[105] and morphing

aircraft[106]. Many efforts have been proposed focusing on the electrical actuation of CNT/SMP composites. Electro-active multi-walled carbon nanotubes filled polyurethane shape memory composites were prepared by Mahapatra et al.[107]. The resultant composites showed more than 98% shape recovery ratio and a rapid recovery time of 9s under a voltage of 40V. Lu et al.[108] investigated the shape memory behaviors of CNT nanopaper/SMP composites. Owing to the excellent electrical conductivity of nanopaper, their composites showed a fully shape recovery at a low voltage of 8.4V. Table 4 summarized and compared the previously reported electrical actuation of carbon nanotube based shape memory polymer composites. All of them showed global actuation of shape memory polymer composites[109], as shown in Figure 13. However, for smart skin or morphing structure applications, localized actuation is preferred.

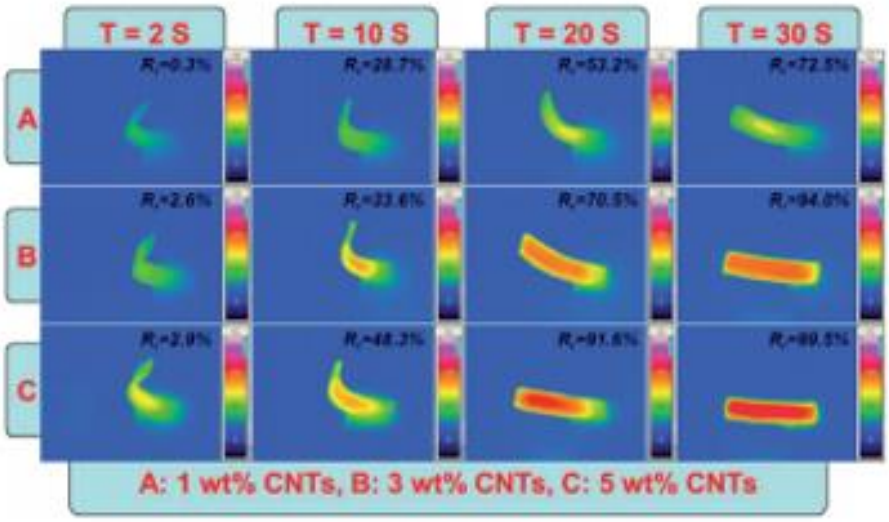

Figure 13. Electrical actuation of rectangular shaped carbon nanotube based shape memory nanocomposites[109]

CHAPTOR THREE: SYNTHESIS AND PROSESSING OF CARBON NANOTUBE BASED POLYMER NANOCOMPOSITES

3.1. Spray Deposition Modeling

All of nanocomposites in this study were fabricated by home-made spray deposition modeling printer. Spray deposition modeling(SDM) is a digital fabrication process in which the CNT ink droplets are supplied in the form of a stream to any desired location because the nozzle is connected to a computer controlled x and y axis, as shown in Figure 14. SDM is similar to an ink jet printer, but SDM has the ability to model over the same area with precision accuracy.

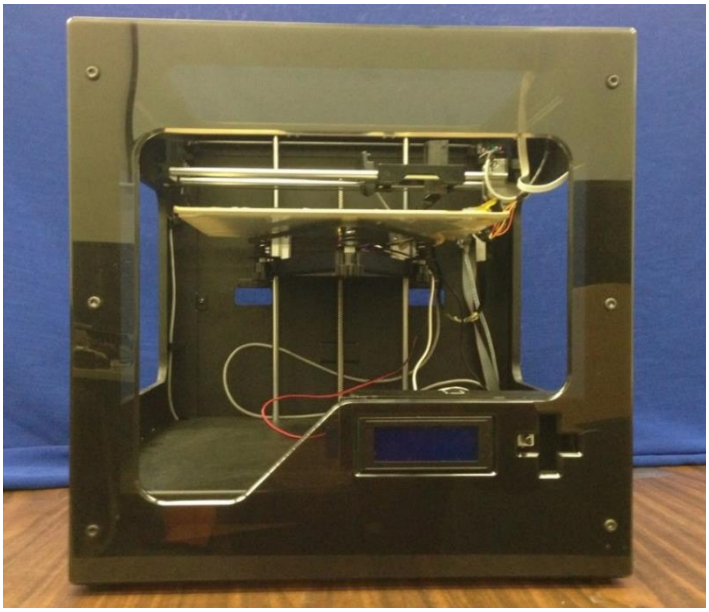

Figure 14. Physical image of the SDM printer

Thermal jet nozzle is used in SDM machine. This nozzle is desirable because it is controllable by a frequency and is manufactured with multiple nozzle outlets to increase productivity. A thermal jet nozzle with a 12 nozzle outlet array and 235 μm pore size is used in SDM. This allows for a large enough pore size to keep the nozzles form clogging while creating particles that are small

enough to ensure the high resolution. The highest frequency for this nozzle is 1250 Hz. Spray deposition modeling uses computer numeric controls (CNC) to move the nozzles into position and allows the thermal jet nozzle to lay down the material properly. The machine runs on G-code, which is a type of code that can be translated into machine code easily. A MATLab code was made to bring in 2D images and generate G-code interoperation of the image. To simplify the process only black and white images were used. Figure 15 shows a plot generated by the MATLab code. It shows each location that the droplets will be released. Products produced by spray deposition modeling are shown in Figure 16, which shows the capabilities of printing strain sensors on different substrates. The digital control of the stream is also capable of creating digital composites that are able to have more functionality and enhance material properties. This digital processing ensures the created composite is geometrically accurate. This process is also additive, which enables the composite to be built layer by layer. Each layers and location could have different composition of materials. The functionality could be realized by the materials design.

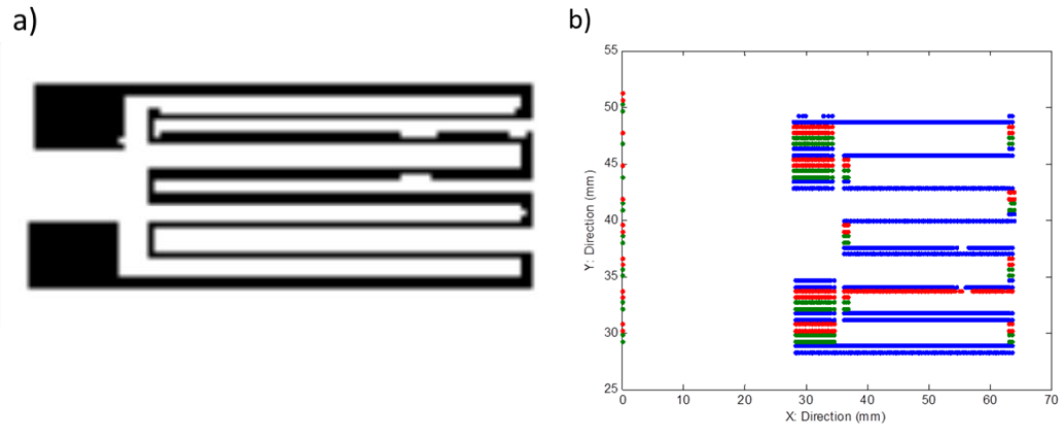

Figure 15. a) Black and white image of strain sensor model b) Droplet pattern

Figure 16. Left) Printed pattern on aluminum plate Middle) Printed pattern on copper foil c) Printed pattern on polyurethane film substrate

3.2. Processing of Carbon Nanotube/Polyurethane Strain Sensor

Multi-walled carbon nanotubes were used as printing materials. The purity of MWCNT is higher than 90%. Substrates materials used in this work were polyurethane film. Most of the MWCNTs have 30-50nm outer diameter and 1~10um length. Thermoplastic polyurethane utilized in this work was supplied by SMP Technologies Inc. in pellet form. DMF solvent can be used to dissolve pellets into solution. The pellets have a specific gravity of 1.25g/cm^3.

The carbon nanotube powder needed to be dispersed in water to form a suspension for digital printing. Generally, 0.1g MWCNT material was initially dispersed in 150ml water using a sonication tip((1375-watts sonicator from Qsonica. LLC.). The surfactant X-100 was added to the solvent to help dispersion. Good quality dispersion was achieved by sonication for 1h. It is important to control the input energy and sonication time carefully to achieve optimized dispersion quality. Since short sonication time and less energy cannot fully disperse HCNT in solvent, while too long sonication time and too much power may damage MWCNT. The received CNT ink after sonication has a stability for at least 1 week, as shown in Figure 17. Figure 18 shows the SEM

images of carbon nanotube before and after sonication. It shows that the carbon nanotubes are separated from the entangled state and formed a uniform conductive network.

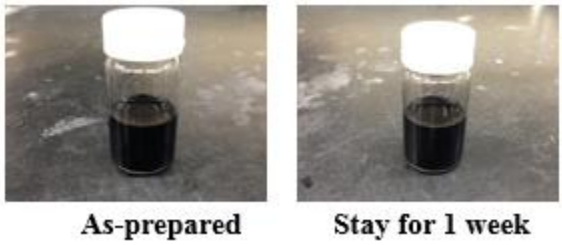

Figure 17. Physical images of carbon nano-inks

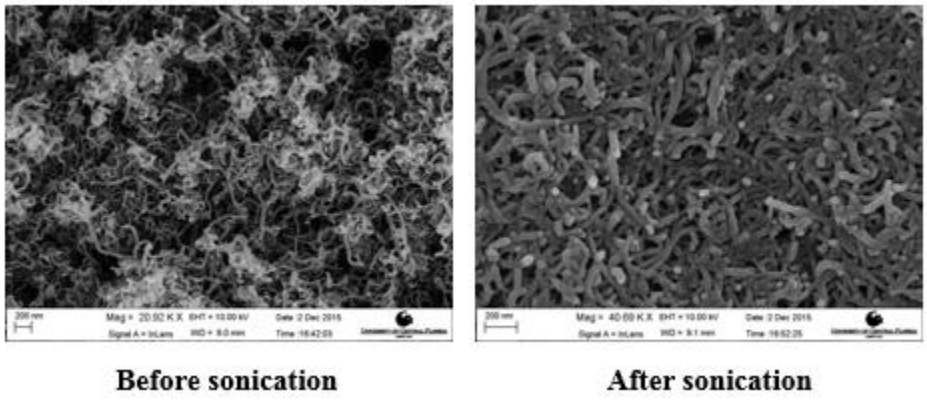

Figure 18. SEM images of carbon nanotubes before and after sonication

MWCNTs/TPU strain sensors was processed through spray deposition modeling technique.

The process began with MWCNT water suspensions. After sonication, the suspension was then placed into the thermal jet nozzle to be sprayed on to the substrate. While the substrate was heated, the nozzle sprayed the material in the order given by the G-code. During the spraying process, water evaporated and MWCNTs were deposited on the substrate. The digital fabrication of CNT strain sensors is achieved by the process shown in Figure 19. For test simplicity, unidirectional

strain sensors were fabricated with different numbers of printed layers from 10 to 50 layers (interval is 10), as shown in Figure 20. Polyurethane films were used as substrates.

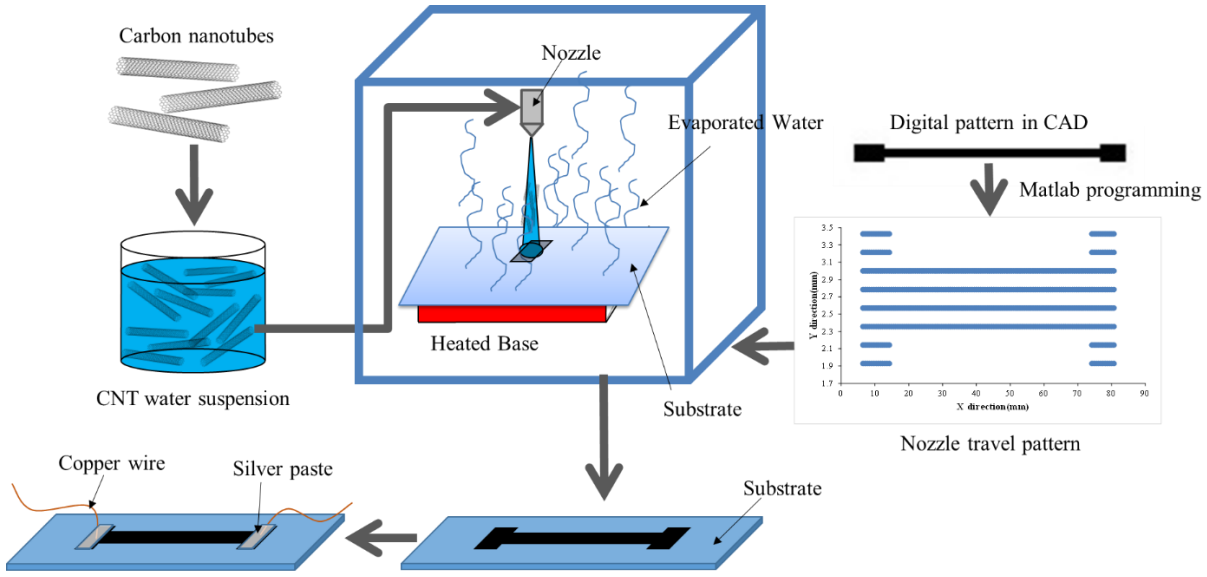

Figure 19. Schematic of the digital fabrication of CNT strain sensors through the SDM technique

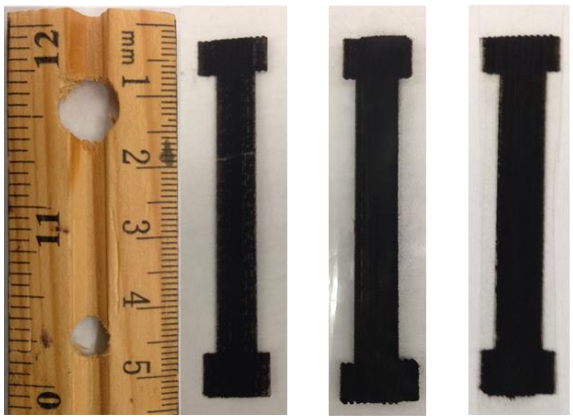

Figure 20. Fabricated strain sensor with different printed CNT layers

3.3. Processing of Highly Flexible Carbon Nanotube/PDMS Strain Sensor

First, PDMS and its curing agent (Sylgard 184 Silicone Elastomer Kit, Dow Corning) were mixed in 10:1 weight ratio and cured in oven at 100°C for 1.5 hrs. Acid treatment (H_2O_2:H_2SO_4 = 1:3, H_2O_2 30%; H_2SO_4 98%; purchased from Sigma-Aldrich) was performed to increase the hydrophilicity of PDMS substrate for aqueous ink printing. PDMS substrate was treated in acid for 5min and then rinsed with deionized water, and dried in the oven. After the surface modification process, PDMS were obtained as a substrate with a thickness of 0.4mm and used for the further printing process. Secondly, the prepared CNT ink was printed on the PDMS substrate using a home-made spray deposition modeling printer. The pattern design of sensors was done in a CAD software. Ink preparation, printer set-up and printing parameters are same as those mentioned in previous section. After the printing process, copper wires were attached to the end of CNT patterns and finally another layer of PDMS was cured on top of printed patterns to obtain the composite strain sensors. Figure 21 schematically depicts the digital fabrication process of composite strain sensors carried out through deposition CNT on PDMS substrate using SDM printing process.

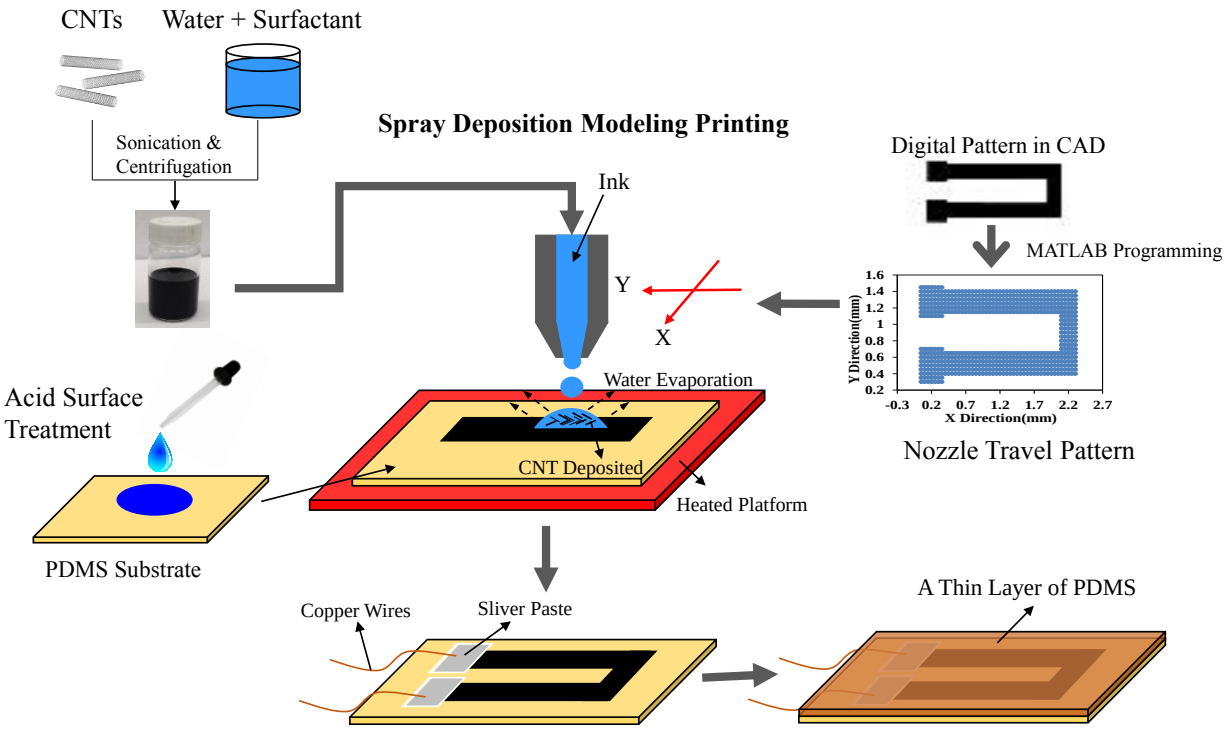

Figure 21. Schematic of the digital fabrication of composite strain sensors through the SDM technique

3.4. Processing of Carbon Nanotube/Polyurethane Nanocomposites with Self-Heating Properties

A three-step procedure was used to fabricate the CNT/SMP nanocomposites, as shown in Figure 22. First, SMP was dissolved in DMF at 70°C for 6hrs and after that, the hot solution was poured into petri dishes. Samples were then dried in a vacuum oven at 90°C for 12hrs. The samples were obtained as transparent films with a thickness of 70μm and used as substrates for the further printing process. Second, the prepared CNT ink was printed on to the SMP substrate using spray deposition modeling process, which is same as the process described in previous section. Finally, the obtained nanocomposite was pressed at 140°C for 3min in a hot press to infiltrate thermoplastic polyurethane into the CNT layers.

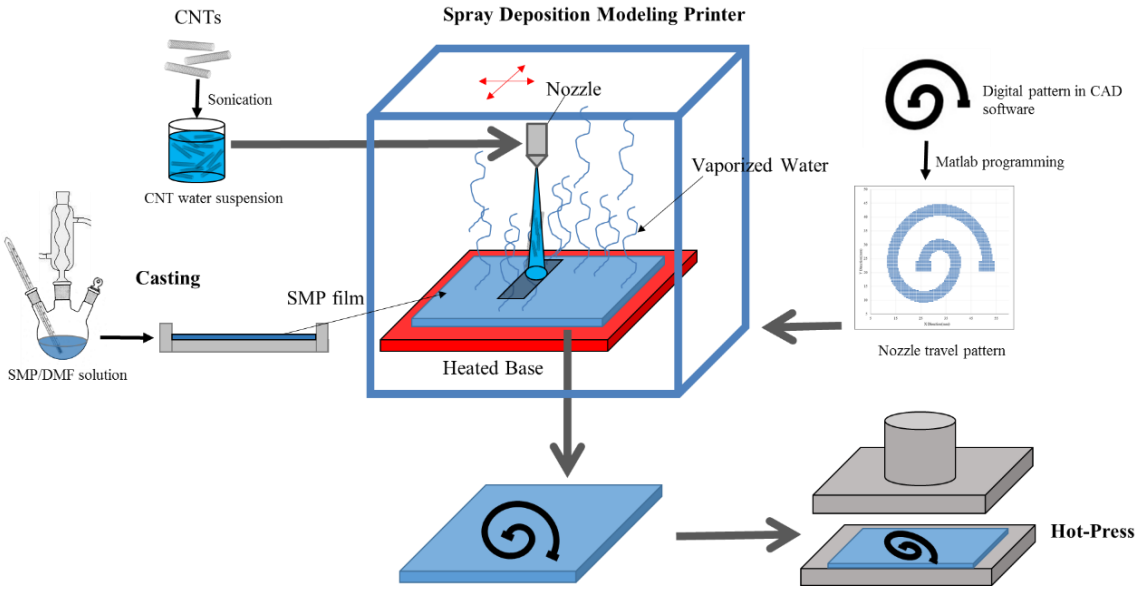

Figure 22. Schematic of the fabrication process of CNT/TPU nanocomposites

3.5. Processing of Carbon Nanotube/Shape Memory Polymer Nanocomposites

Shape memory thermoplastic polyurethane pellets with a glass transition temperature(T_g) of 55°C (SMP Technologies Inc.) were obtained from commercial sources and used as received. MWCNT inks were printed on two types of substrate to produce CNT/SMP nanocomposites. One type of substrate is SMP thin film. SMP was dissolved in DMF at 70°C for 6hrs and after that, the hot solution was poured into petri dishes to produce thin film substrate. To test the shape recovery performance, a 'U' shape CNT film was printed on polyurethane substrate. The left half side of 'U' shape has 20 printed CNT layers and the right half side of 'U' shape has 50 printed CNT layers. Another substrate is honeycomb structured substrate. Shape memory polymer filaments were fabricated through single-screw extruder and fused deposition modeling 3D printer was used to print the CAD designed honeycomb structured substrate. A home-made single-screw extruder used

in this study is shown in Figure 23. The raw materials used in this study were virgin SMP thermoplastic pellets. During the extrusion process, extrusion temperature and extrusion speed were set at 170°C and 8.7 mm/s. The extruded SMP filament was shown in Figure 24. The FDM 3D printer (Mbot printer) was used to fabricate honeycomb SMP structure. The nozzle temperature was set at 210°C and the printing speed was set at 60mm/s for printing of all layers. 5 layers were printed with each layer thickness of 0.2mm. The infill pattern deposition directions for different layers were 45° and 135°, alternatively. The infill density was set at 100%. Then the prepared CNT inks were printed on these honeycomb substrates.

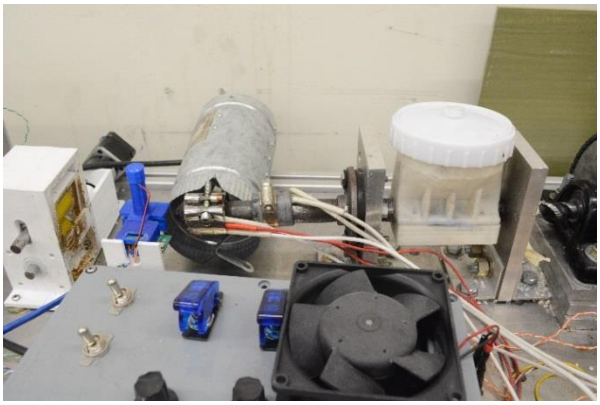

Figure 23. Home-made single-screw extruder for SMP filament fabrication

Figure 24. Raw SMP pellet materials and extruded filament

CHAPTOR FOUR: STRAIN SENSING PERFORMANCE EVALUATION OF THE CNT/TPU NANOCOMPOSITES

4.1. Introduction

Carbon nanotubes (CNTs) have attracted extensive attentions in the research community due to their unique electrical and mechanical properties [110-112]. The electrical resistance of CNTs is interestingly correlated to their mechanical deformation, which is called piezo-resistive effect [113]. This electrical characteristic of CNTs coupled with their high mechanical strength makes them a promising material for strain sensors. Piezo-resistive strain sensors are an interesting area of industrial and academic research due to the growing demand for flexible and wearable electronics [6-9], smart textiles [10] and structural health monitoring [11].

To create CNT based strain sensors with desired properties, various fabrication techniques have been employed to date, including compression molding [86], solution casting [114], contact film transfer [77, 115], screen printing [116, 117] and spray coating [76, 118]. Liu et al. [86] prepared a carbon nanotube/graphene/polyurethane strain sensor by compression molding method. The strain gauge factors were calculated to be 5.1 and 152.93 at 5 % and 30 % strain, respectively. A higher strain sensitivity was obtained at a larger strain. Michelis et al. [82] employed inkjet printing technique to fabricate a carbon nanotube based strain sensor. The gauge factor was found to be 0.9, which is comparable to the gauge factor of commercially available metallic foil strain gauges.

While these techniques are able to create sensors, some challenges in fabrication have prevented their widespread industrial applications. For instance, although the contact film transfer technique is able to produce CNT strain sensors with good sensitivity, transferring film to substrate is time-consuming and complex, often requiring a surface treatment of the substrate and multiple

fabrication steps, which increase the overall cost of and limit the manufacturing scalability of this technique. Conventional spray deposition processes often use an airbrush with large spray area to fabricate strain sensors, but they are not able to deliver CNT materials to desired locations, thus the materials cost increases during the fabrication process. Additionally, these techniques such as film transfer and solution casting lack the ability to produce strain sensors with controlled strain gauge factors.

To address some of the above-mentioned problems, this study reports a scalable and low-cost method, known as spray deposition modeling (SDM), for fabricating carbon nanotube strain sensors with desired gauge factors. SDM is a digital-controlled additive manufacturing process in which the CNT ink droplets are supplied in the form of a stream to any desired location through an x-y axis movable nozzle. Thus, as nozzle moves, the CNT patterns could be printed continuously at different locations. The highest resolution of SDM is 100 dots per inch, which enables the CNT patterns to be printed over the same area with precision and accuracy. The SDM is also an additive manufacturing process, which enables the strain sensor to be built layer by layer and has a minimum loss of the supplied material. Conventional film transfer, spray deposition or solution casting technique do not have the layer-by-layer additive characteristics and manufacturing accuracy, thus SDM is a more efficient method to produce CNT patterns. In this study, CNT strain sensors on polyurethane substrate with high sensitivity were fabricated through the SDM technique and the resulting sensing performance was examined.

4.2. Materials Characterization

The electrical sheet resistance of printed strain sensors was measured at room temperature with a four-point probe apparatus (Signatone Quadpro system). In order to investigate the effect of applied strain on the electrical resistance of the fabricated strain sensors, three types of experiments were performed using a MTS hydraulic 100kN test system including: (1) monotonic tensile test; printed CNT strain sensors were stretched at a constant velocity of 2 mm/min (2) monotonic compression test; Compression specimen was a 12.7 by 12.7 by 25.4 mm prism. The strain sensor was bonded by adhesives to one face of this prism and aligned with the loading direction. The compression specimens were compressed at a constant velocity of 2 mm/min (3) cyclic tensile test; specimens were stretched/released at a constant displacement speed of 0.48 mm/min. Each cycle takes 150 s, and after each cycle, the test system will hold on 20 s to allow for the recovery of residual resistance change. Electrical resistance was measured in situ during tensile loading employing a Fluke 45 digital multimeter that connected to PC to receive data. Copper wires were attached to the two ends of printed CNT strain sensors with silver paste to ensure the accurate electrical resistance test.

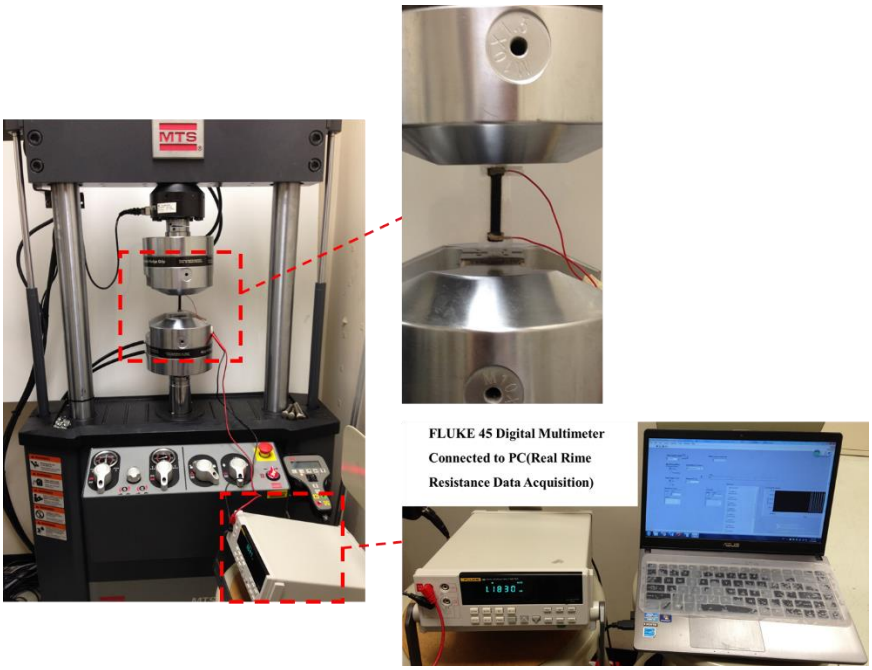

Figure 25. Photograph of experimental set-up for acquisition of mechanical strain and electrical resistance data

4.3. Results and Disscusions

4.3.1 Electrical resistance measurement

The electrical sheet resistance of printed carbon nanotube strain sensors were tested at different locations. Eight locations were chosen to determine the sheet resistance of tested samples, as shown in Figure 26 (a). The sheet resistance of strain sensors with different printed CNT layers at each location was plotted in Figure 26 (b). In the experiments, it was found that the sheet resistance for one sample at different locations does not have many variations, which confirms the uniformity of printed CNT strain sensor. The average values of sheet resistance and the thickness of tested samples with different printed CNT layers were plotted in Figure 26 (c). With the increasing of number of layers, the thickness of CNT layers increase whereas the sheet resistance of printed

sensors showed an exponential decrease. It is expected that the more carbon nanotubes in the sensors, the more conductive paths are formed so the sheet resistance decreases a lot. Further compacting and distribution of the nanotube network also contribute to the decrease of sheet resistance. With 50 layers CNT printed, the sheet resistance of CNT layers is 18.76 Ω /sq. which is much lower than the value ~760 Ω /sq [119] and ~78 Ω /sq [120] of fabricated CNT films in previously published articles. The uniformity and low sheet resistance of printed strain sensors can be attributed to the homogeneous dispersion of CNT in the aqueous solution and the effectiveness of the optimized SDM process.

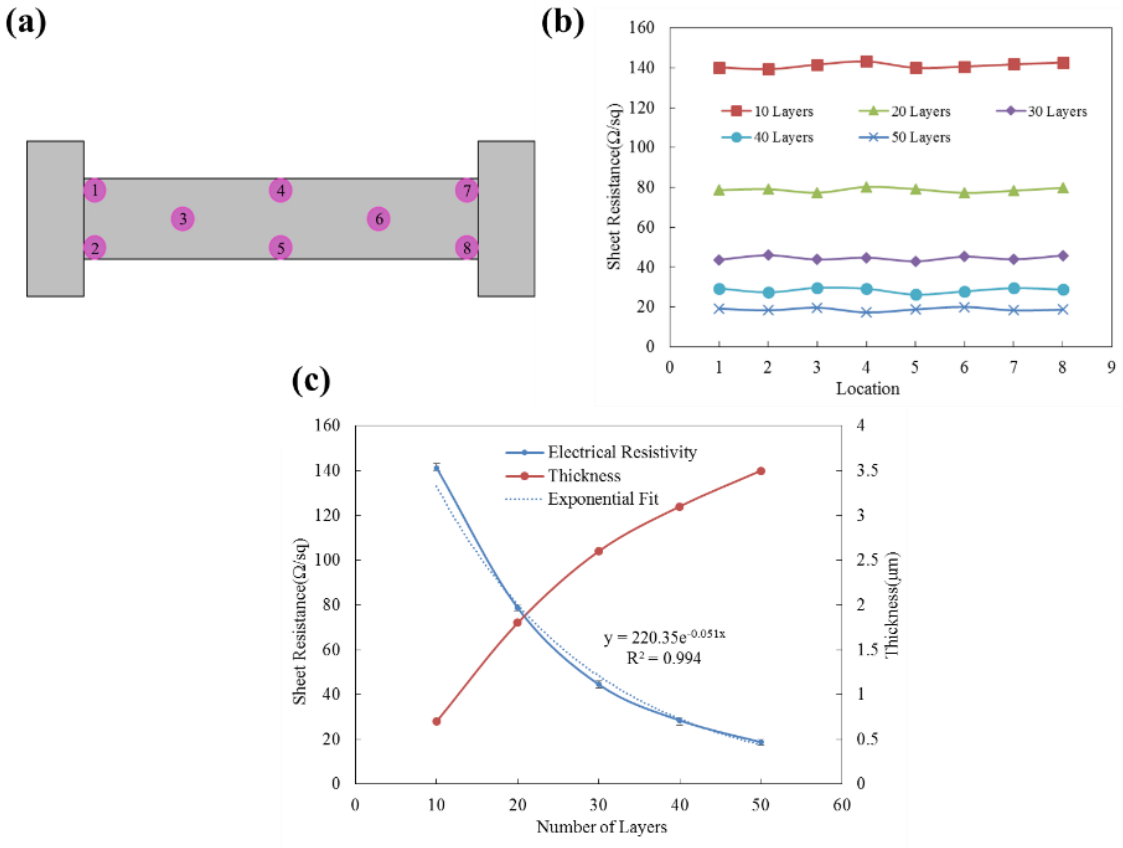

Figure 26. (a) Schematic illustration of location selected for measuring sheet resistance. (b) Sheet resistance of sensors at different locations. (c) Sheet resistance curve of sensors with different printed CNT layers

4.3.2 Strain sensing capabilities

Strain sensors with different number of printed CNT layers were tested to examine the effect of the number of printed CNT layers on the sensitivity of strain sensors. The density of the CNT networks could be controlled by altering the number of printed CNT layers.

The representative resistance change-strain data recorded under tension for the CNT strain sensors is shown in Figure 27. It was found that there is a slight nonlinear relationship between the increasing of resistance and strain. It seems that as strain increases, the increasing of electrical resistance is a little bit faster. That is possibly due to the CNT networks were damaged inhomogenously at a higher strain and thus the resistance increases faster. Additionally, the CNT network was only stretched slightly in the loading direction at low strain, and the other conduction networks may form in other directions due to the compression in the perpendicular direction, so the resistance change may be slow at the beginning of stretching. Therefore, a small nonlinearity was observed in these strain sensors, but overall the resistance could be seen as increasing linearly with the strain (R^2>0.96) for all the sensors. A gauge factor was used to characterize the strain sensing properties of carbon nanotube strain sensor [121]:

$$K = \frac{\Delta R/R_0}{\varepsilon} \quad (1)$$

where: R_0 is the resistance of carbon nanotube strain sensor without strain, ΔR is the resistance change under strain, ε is the strain and K is the gauge factor. Figure 28 (a) showed the linear fit of resistance change – strain relationship for sensors with 50 printed CNT layers. The gauge factors was obtained as the slope of fitted lines.

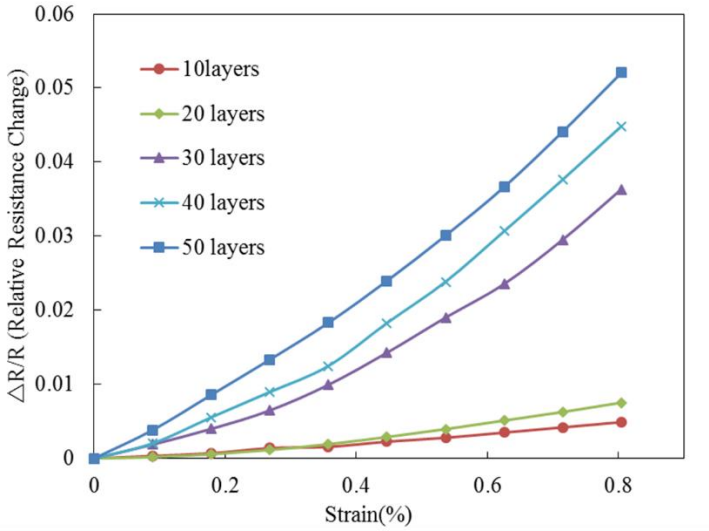

Figure 27. Resistance change–strain relationship of printed CNT sensors with different number of printing layers

As shown in Figure 28 (b), strain sensors with more printed CNT layers showed a larger strain gauge factor indicating that the sensor sensitivity could be tuned by simply altering the number of printed CNT layers. For the strain sensor with small number of CNT layers, the resistance at an un-stretched state is high due to the loose CNT network. Compared with this original resistance value, the resistance change is small which can explain why this sensor has a low gauge factor. In addition, a loose network could cause an inefficient load transfer within the CNT network. Therefore, the sensor with thin CNT layers has a lower sensitivity than the one with thick CNT layers. This behavior was also observed in previous reports [122, 123]. For each kind of samples, a group of five samples was tested. A variation of less than 10 % was observed, which indicated the good repeatability of strain sensors fabricated by SDM process. The highest gauge factor obtained in this study is 6.42, which is higher than the value of ~2 [124] reported for conventional metallic foil strain gauges, the value of ~0.9 [82] and ~2.8 [125] reported for strain sensors

fabricated by conventional spray-based technique. The gauge factors calculated in this study are lower than those high values of sensors fabricated by contact film transfer [77] or compression molding method [86], because the carbon nanotube strain sensors fabricated by those methods could have denser CNT network or stronger interfacial bonding with polymer due to the applied pressure during fabrication process. Thus, the sensor may show higher sensitivity in those cases. Overall, although the strain gauge factors of sensors we developed by SDM are lower than those value of sensors fabricated by contact film transfer and compression molding, these values are high among those of sensors fabricated by spray-based method, which is a method that could fabricate sensors continuously with lower cost.

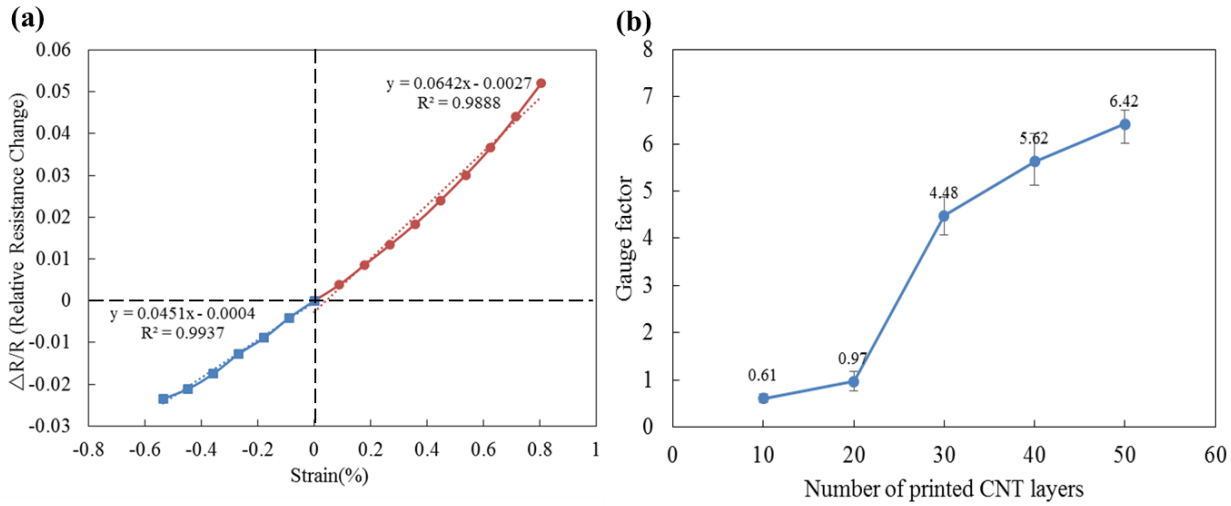

Figure 28. (a) Linear fit of the resistance change–strain plot for the sensor with 50 printed CNT layers (b) Gauge factors of sensors with different printed CNT layers

Figure 28 (a) also shows the compressive elastic piezoresistive response of fabricated strain sensors. In the elastic region under compression, carbon nanotube networks were further compacted resulting in more conductive paths to reduce the electrical resistance of composite

sensors. It can be seen that under compression, the resistance of strain sensors also increased linearly with the strain indicating that these strain sensors are capable of measuring strain under compression condition. The gauge factor of sensors under compression is 4.51, which is lower than the gauge factor obtained at tension condition. One possible reason is that when carbon nanotube networks were further compacted under compression, the decreasing of overall electrical resistance resulting from the reducing of contact resistance between carbon nanotubes is limited, whereas the intrinsic electrical resistance of carbon nanotubes become more dominant to determine the overall resistance [126]. At this elastic strain range, the intrinsic electrical resistance of carbon nanotube will not decrease a lot, thus the fabricated sensors showed less sensitivity under compression state than under tension state.

To examine the strain-dependence behavior under a cyclic loading, strain profiles in Figure 29 (a) were applied to the CNT strain sensor with 50 printed layers. As shown in Figure 29 (b), the printed strain sensor exhibits a hysteretic behavior at the stretching/releasing cycle possibly due to a hysteretic behavior of the polymer substrate [79]. Creep and relaxation have been reported in the tensile properties of polyurethane [127], thus during stretching/releasing cycle, it is possible that the polymer substrate cannot react rapidly as the strain changes, so the breakdown and re-connection of contacts within the CNT network may occur at disparate time scales. Hysteresis may also be caused by the friction and poor interfacial adhesion between CNTs and the polymer substrate [113]. Additionally, the intrinsic hysteretic behavior of CNTs may also be a possible reason for the hysteretic behavior of piezoresistive strain sensors [128]. During the releasing cycle of stress, the CNTs try to regain their original stretched state, so there may be a time difference between the change of strain and the change of electrical resistance. However, the resistance recovers to its original value in less than 20 s. A shorter delay time was found compared to the

previous study [129]. Moreover, non-recoverable resistance has not been found in the printed sensor, which is better than other reported sensors [79, 85].

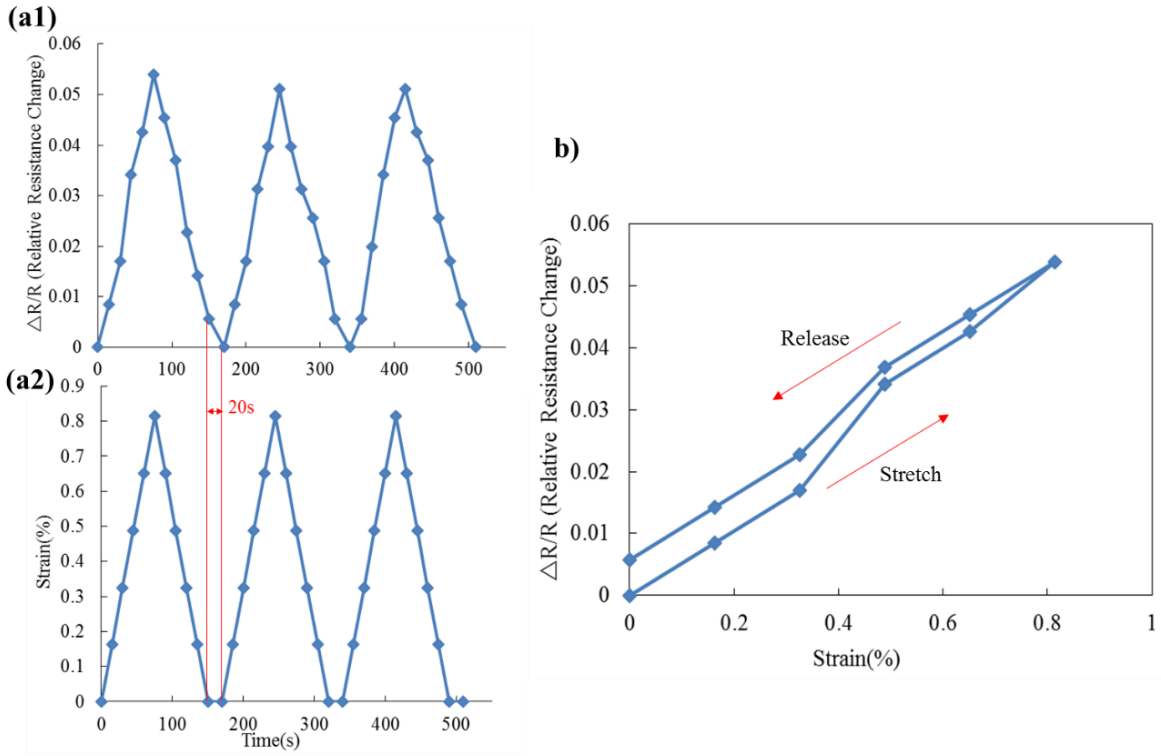

Figure 29. Relative resistance change history of sensors with 50 printed CNT layers at (a) Cyclic stretching/releasing (a1) Relative resistance change versus time (a2) Strain versus time (b) first stretching/releasing cycle

The resistance responses of first 5 cycles and cycle 26-30 are shown in Figure 30 (a). Figure 30 (b) shows the resistance change plotted as a function of the number of cycles. During the first 5 cycles, the electrical resistance change decreases, possibly because the breakdown of original CNT networks results in an inefficient load transfer in CNT networks thus affects their sensitivity. However, after 5 cycles, the electrical resistance change was nearly stabilized. In all thirty cycles, the sensor shows a good sensitivity to the applied strain and a full recovery of resistance after

releasing of strain. These results indicated that the printed carbon-nanotube strain sensor exhibited good durability and stability under cyclic loading.

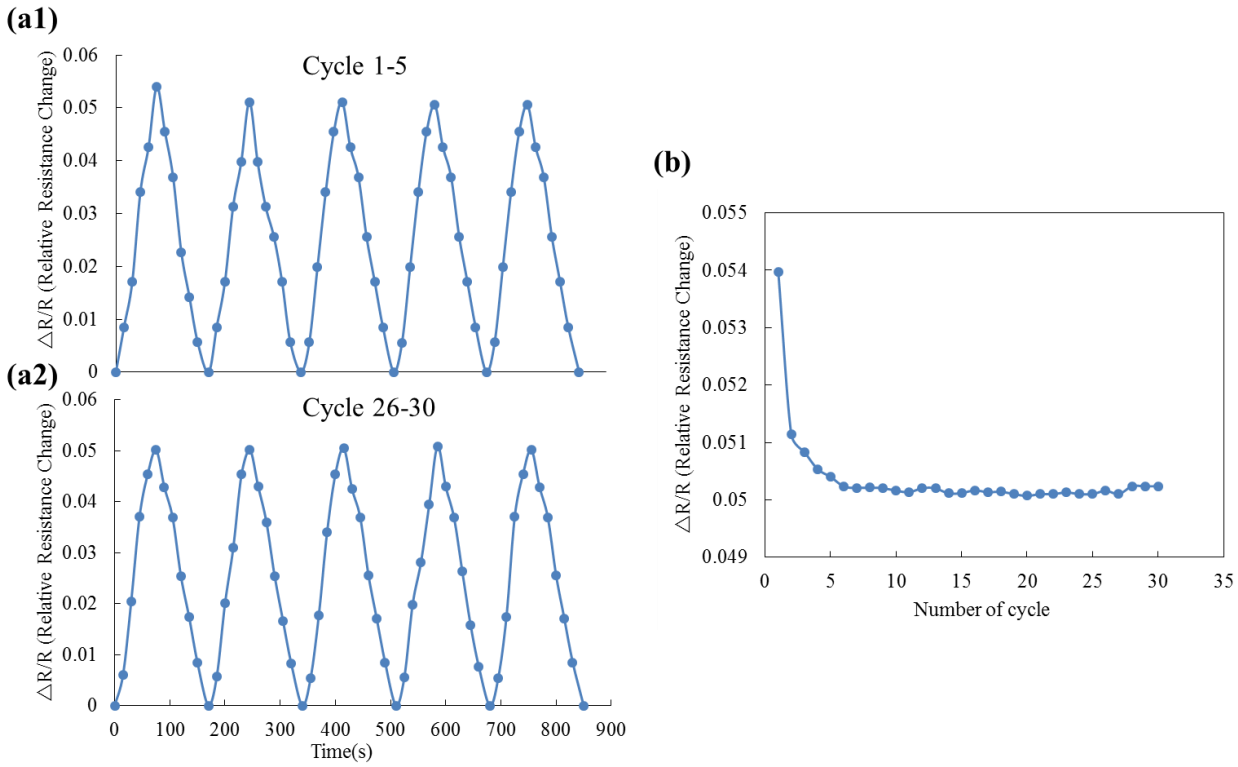

Figure 30. Relative resistance change history of sensors with 50 printed CNT layers at (a1) first 5 and (a2) 26-30 loading cycles (b) Maximum resistance change ratio for each loading cycle

4.4. Conclusion

This study employed a new spray deposition modeling technique to fabricate carbon nanotube strain sensors to monitor the strain based on the piezo-effect of carbon nanotubes. This fabrication technique has an exquisite print path control that enables the fabrication of CNT sensors with desired geometries and strain gauge factors. The additive characteristic of this fabrication technique has an advantage of saving material. A large scale production could be realized by

applying multiple spraying nozzles. Therefore, this SDM technique can overcome the drawbacks of the conventional fabrication technique of CNT strain sensors and provide an efficient way to manufacture CNT strain sensors that could work with high sensitivity. Due to the flexibility of this SDM fabrication technique, the properties of strain sensors could be easily tuned by controlling the number of printing layers of CNT sensors.

The relationship between the change in electrical resistance and the applied strain of carbon nanotube sensors was studied. All the printed sensors exhibited good linearity of electro-mechanical response and high sensitivity. Strain sensors were fabricated with different numbers of printed carbon nanotube layers from 10 to 50 layers and strain gauge factors were measured in a range of 0.61-6.42. It was concluded that as the number of printed CNT layers increases, the sensitivity of CNT strain sensors increases. The highest gauge factor of is 6.42, which is higher than that of metallic foil strain sensors. Moreover, upon the dynamic cyclic loading, all the printed carbon-nanotube strain sensors exhibited excellent durability and stability at cyclic strain. Particularly, the printed strain sensors are soft thin films that could either be embedded in structures or on the surface of structures, which coupled with their superior sensing capabilities prepare them for practical applications.

CHAPTOR FIVE: STRAIN SENSING PERFORMANCE EVALUATION OF THE HIGHLY FLEXIBLE CNT/PDMS NANOCOMPOSITES

5.1. Introdcution

Stretchable and flexible sensors have attracted considerable attention for their potential applications in wearable electronics[130], smart textiles[131], soft robotics[132] and structural health monitoring[11]. Monitoring human body motion has drawn great interests for developing artificial skin and healthcare-related wearable electronics [133-135]. Strain sensors that allow the mechanical deformations to be quantified through corresponding electrical signals have been a promising engineering tool for human body motion detection. Commercially available metal based strain sensors have limited stretchability (typically ~5%) and sensitivity(~2 of gauge factor) to detect large-scale human motions like bending of arms or hands[80]. As such, there is a pressing need to develop stretchable and wearable strain sensors with high sensitivity for monitoring human motions. Composites have attracted considerable attention due to their ability to combine the matrix and reinforcement to achieve excellent functional properties[102, 103], and composites consist of flexible polymer matrix and piezo-resistive filler have been a promising candidate for flexible and wearable strain sensors[136, 137].

To fabricate strain sensors with desired properties, various piezo-resistive filler have been used to date, including metal nanomaterials[138], graphene[139, 140], and carbon nanotubes(CNT)[82, 141]. In particular, CNTs have been used extensively for flexible strain sensors due to their unique electrical and mechanical properties[110, 111]. The high aspect ratio of carbon nanotubes makes them entangled to form internal conductive network, and the network could breakdown when stretched and reconstruct when the strain released, showing a measurable electrical resistance

change. Several studies have been conducted on the flexible strain sensors based on carbon nanotube and elastomers. For instance, CNTs were spray-deposited on a PDMS substrate to prepare a strain sensor, which could accommodate strain up to 150% for detection of large-scale human motions[141]. Besides this, strain sensors based on carbon nanotube and graphene were fabricated by compression molding method to investigate the synergistic effect of bifiller on strain sensing. The produced strain sensors exhibited a high sensitivity with a gauge factor of 152.93 at 30 % strain[86].

However, most of previously-reported sensors were fabricated through expensive and complex processes without controllable sensitivity or good response linearity for measuring diverse human motions. Additionally, these techniques such as film transfer and solution casting are only capable of producing strain sensors with simple rectangle geometry to measure strain in a single direction, but for monitoring human motion with complicated strain condition, strain sensors that can measure strain from multi-direction are favorable. Furthermore, in most of previous reports, the ability of strain sensors to detect human motion was just demoed and the accuracy of the strain data obtained from the sensors has rarely been reported.

To overcome these problems, in this work, we develop highly stretchable and wearable strain sensors with adjustable sensitivity by using a digitally-controlled spray deposition modeling (SDM) printer to incorporate CNT layers into PDMS substrate. The CNT layers were printed on the PDMS substrate by SDM technique which is an additive and layer-by-layer method for producing CNT layers with controllable thickness and desired patterns[142]. Strain sensors with different printing cycles of CNT layer were fabricated to investigate the effect of CNT thickness on the sensing properties. Two types of flexible strain sensors, unidirectional-type and rosette-type sensors, were fabricated to investigate the ability of strain sensors to detect human motions and their performance

was characterized. Moreover, to demonstrate the feasibility and accuracy of fabricated strain sensors for monitoring human motions, strain information obtained from the fabricated strain sensors was compared with the measured human muscle-induced strain recorded by camera system. In comparison with previously reported CNT/elastomer composite strain sensors, our sensors possesses remarkable advantages, such as high stretchability, high sensitivity as well as high accuracy, and especially, the rosette-typed sensors are able to elaborate complex strain condition. Additionally, the sensors are fabricated with the help of digital additive printing technique which is cost-effective and scalable. Such properties can give these strain sensors great application potential in wearable electronics, human-machine interaction and other related areas.

5.2. Characterization

Scanning electron microscopy (SEM, Zeiss-Ultra 55) was used to examine the morphology of the composite strain sensors under an accelerating voltage of 10kV. The strain sensing test were carried out on a MTS hydraulic 100kN test system. Specimens were stretched/released at a constant frequency of 0.2 Hz. Real-time electrical resistance was measured during the tests using a Fluke 45 digital multi-meter connected to a PC that records data through LabView software. Silver paste electrodes were coated to the two ends of sensors to reduce the contact resistance.

5.3. Result and Discussion

In this study, polydimethylsilicone (PDMS) was utilized as flexible substrate for composite strain sensors owing to their high elasticity and fast response speed to strain[136]. However, the surface of PDMS substrate is highly hydrophobic with very low surface energy[143]. Therefore,

appropriate surface modification of PDMS is required to increase the wetting of aqueous CNT ink. In this work, we used an inexpensive approach involving chemical treatment in acid solution to render the hydrophilicity of PDMS surface. Static contact angles were measured with water by using a calibrated syringe and a digital camera. The contact angle value measured is shown in Figure 31. It is observed that with 5 mins treatment, the contact angle reduced from 95° to 54°, which is beneficial for printing of aqueous ink. The hydrophilicity improvement of PDMS surface could be attribute to an oxidized surface where Si-CH_3 bonds was attacked by the strong acid oxidizer to form a hydrophilic Si-OH group[144].

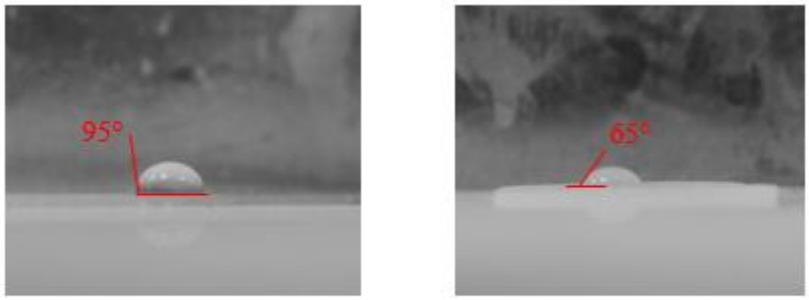

Figure 31. The contact angle between water and PDMS substrate before and after acid treatment

To control the thickness of CNT layer in composites, different numbers of printing cycles were performed. Figure 32 shows the CNT layers that fabricated with different numbers of printing cycles from 10 to 50 with an interval of 10 layers. It shows that the CNT layer became darker as printing cycle increases, indicating the increasing of thickness of CNT layer. It should be noticed that when the printing number is small, the deposited CNT layer is not perfectly uniform because of the “coffee ring” effect with CNT dispersion[145], but as the printing number increases, more

homogenous CNT layer is formed. The fabricated strain sensors are shown in Figure 32(b), which indicating the excellent stretchability.

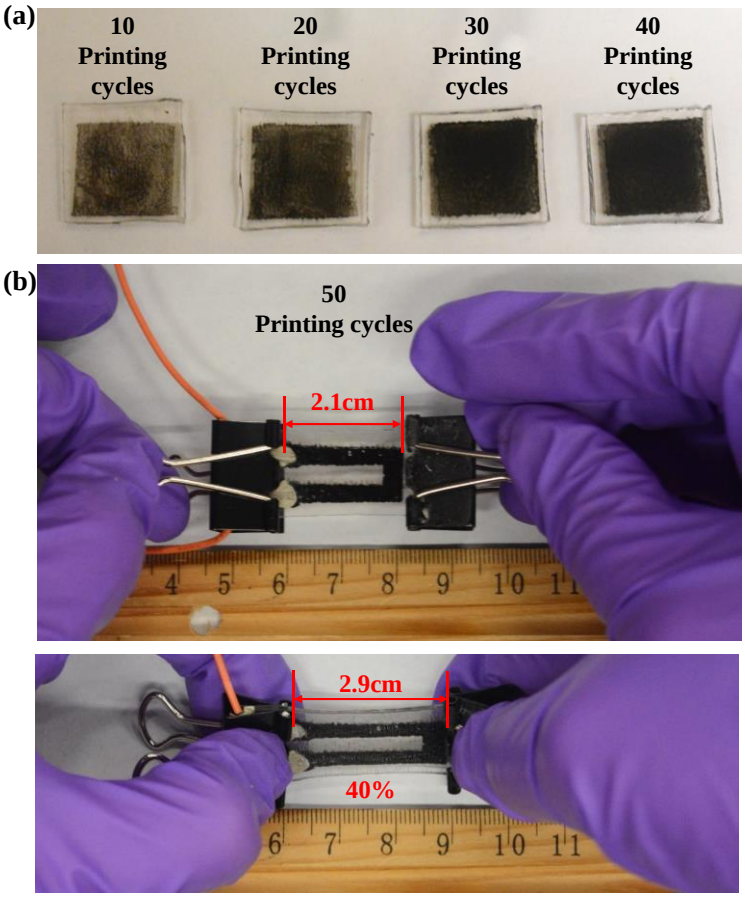

Figure 32. (a) Optical images of CNT layers printed with 10, 20, 30, 40 cycles; (b) photograph of the strain sensor subjected to 40% strain

To identify the morphology of the printed pristine CNT layer on PDMS substrate, cross-section SEM images of CNT layers obtained by 10 and 50 printing cycles were shown in Figure 33(a) and (b), respectively. Figure 33(c) clearly shows that CNTs were uniformly deposited on PDMS substrate to form a dense and continuous conductive network without the agglomeration of CNTs, owing to the homogenous dispersion of CNTs in water as well as the optimized and effective SDM

printing process. The thickness of CNT layers obtained by different number of printing cycles could be acquired from the SEM images, as plotted in Figure 34(a). As the number of printing cycles increase, the CNT layer becomes thicker correspondingly, indicating the tunable CNT layer thickness by controlling the number of printing cycles. The thickness of CNT layers was 1.6, 3.2, 5.4, 7.2, 8.4μm, which corresponds to 10, 20, 30, 40, 50 printing cycles. Figure 34(b) and (c) shows the morphology of the fractured surface of CNT/PDMS composite, where the PDMS resin fully impregnated throughout CNT networks indicating a good interfacial bonding between matrix and fillers. The "sandwich" layered structure with one CNT embedded composite layer was also confirmed from Figure 34(b).

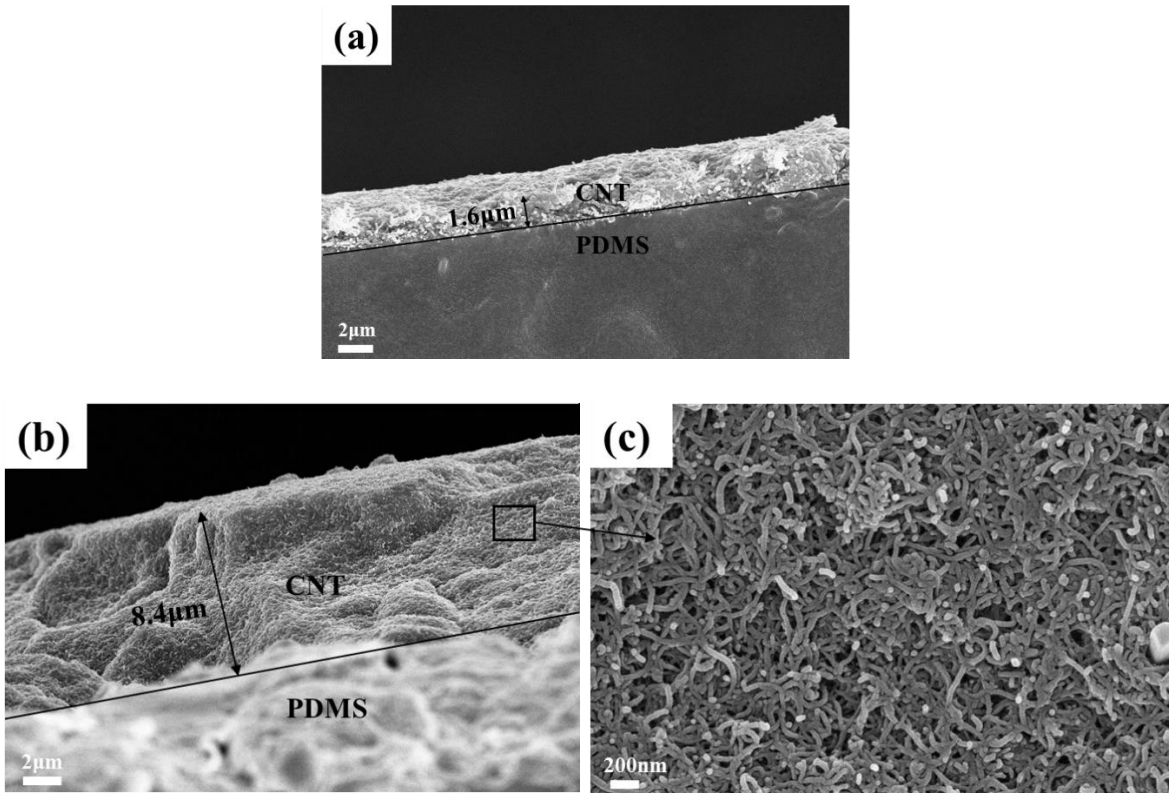

Figure 33. Cross-section SEM images of pristine CNT layers on PDMS substrate with (a) 10; (b-c) 50 printing cycles; (d) CNT layer thickness as a function of printing cycle number; Cross-section SEM images of CNT/PDMS composite with 50 printing cycles of CNT layer

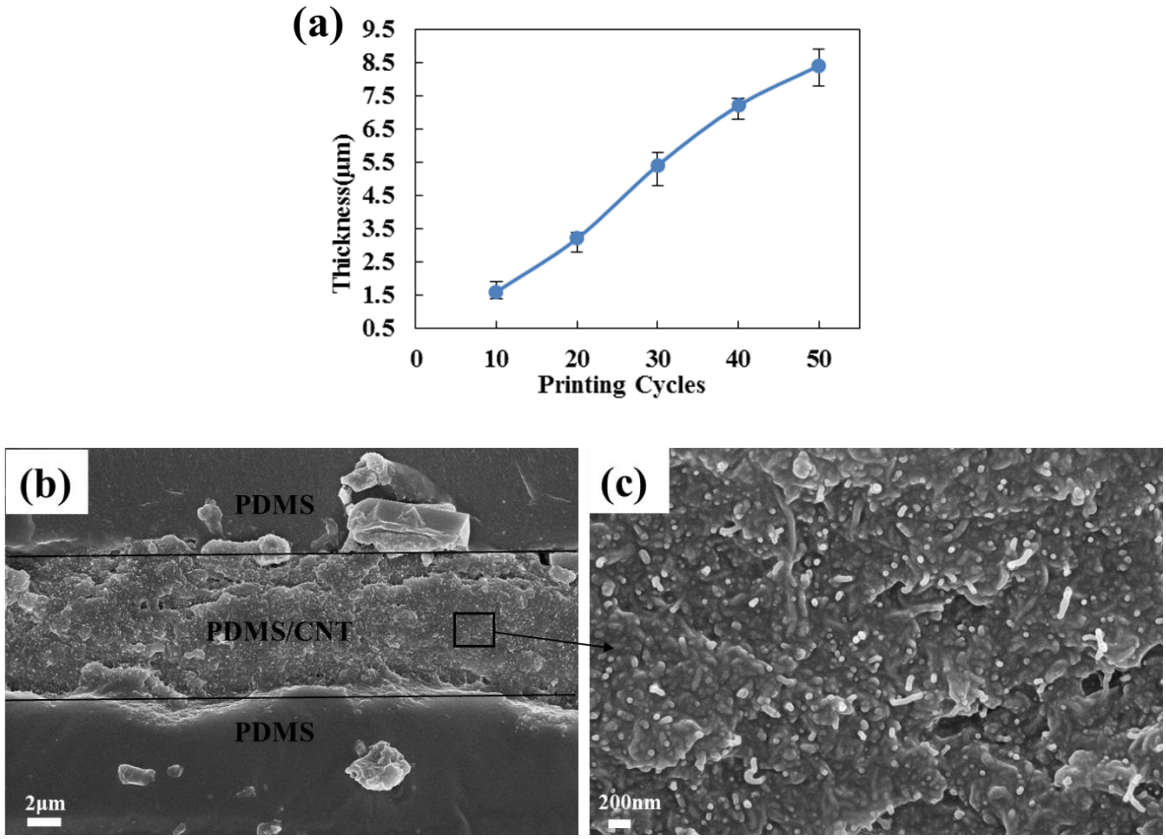

Figure 34. (a) CNT layer thickness as a function of printing cycle number; (b-c) Cross-section SEM images of CNT/PDMS composite with 50 printing cycles of CNT layer

The thickness effect of CNT layers on the strain sensing property of the composite sensors was investigated by comparing the sensors made from different printing cycles of CNT layer. The strain sensors with area of 15x50 mm^2 and thickness of 0.5mm were prepared for sensing testing, and were named as CPx, where x denotes the printing cycles of CNT layer. These composite strain sensors were characterized with regard to the applied strain under tension, and the strain sensors were stretched up to 45% strain until the plastic deformation was found. Figure 35(a) shows the representative resistance change-strain data. All the sensors exhibited similar piezoresistive responses to the strain, and with increasing strain, the electrical resistance of all the sensors

increased. The strain-dependent responses of the sensors were found to have two regions. In low strain region (less than 10%), the stretching of CNT network was just initiated in the loading direction, and there are still many CNT junctions due to the compression of transverse direction, so the resistance change was slow at the beginning of the stretching. The linear increasing of electrical resistance as the strain increases became stable after the initiation stage. In particular, the sensitivity of the fabricated sensors could be modulated by simply tailoring the printing cycles of printed CNT layer to accommodate diverse sensing requirements. As shown in Figure 35(a), the resistance of composite strain sensors with more printed CNT layers increased significantly, indicating that the sensors with more CNT layers were more sensitive to applied strain. This is possibly explained by the conducting mechanism in the CNT network [126]. At un-stretched state, strain sensors with thicker CNT layer have a higher density CNT network and more CNT joints, thus the contact resistance between CNTs dominantly determines the overall resistance. When the strain was applied, the cracking occurred in the CNT network resulting in the disconnection of most CNT joints so that the connection mode transfers to the tunneling state where a large increase of electrical resistance exists. However, for sensors with thinner CNT layer, the CNT joint is few at original state and the conducting mechanism transition is less visible so that they are insensitive to external stimulus.

Generally, the gauge factor $[K = (\Delta R/R_0) / \varepsilon]$ was calculated to determine the sensitivity of composite strain sensors [121], where R_0 is the resistance of carbon nanotube strain sensor without strain, ΔR is the resistance change under strain, ε is the strain and K is the gauge factor. For all the sensors, the electrical resistance increased linearly with the strain (R^2>0.98), and the gauge factors are almost constant after the initiation stage (Figure 35 inset). This good linearity is

of vital importance in precise sensing of strains, and the gauge factor of all sensors are plotted in Figure 35(b), suggesting that the desire controllability of gauge factors, which is beneficial to diverse applications.

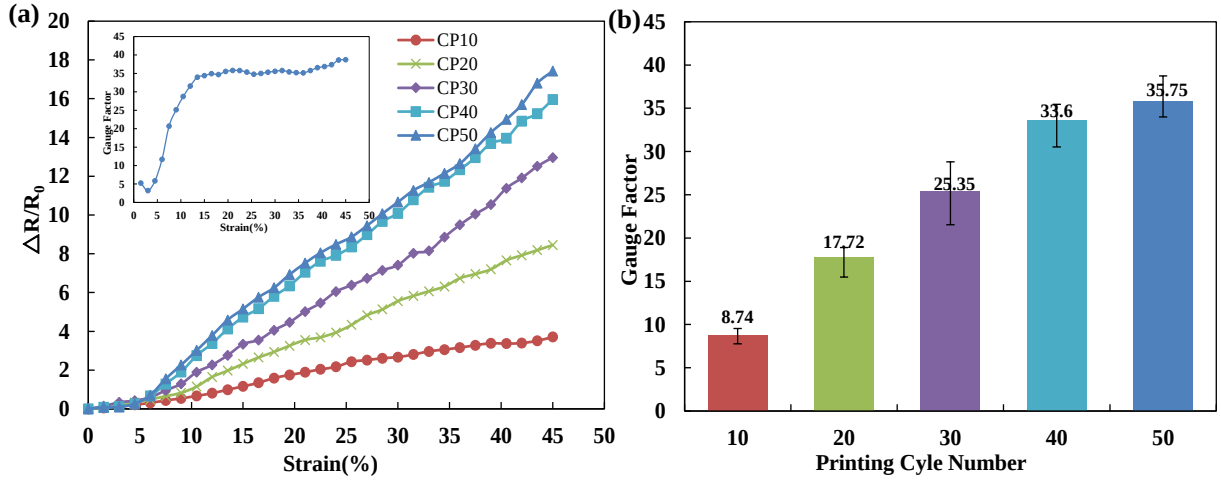

Figure 35. (a) Resistance change–strain relationship of composite sensors with different CNT layer thickness (b) Corresponding gauge factors

Three types of resistances contribute to the overall resistance of CNT networks. The first is the intrinsic resistance of CNT, R_{cnt}, the second is the contact resistance R_C (resistance between CNTs that are physically in contact), and the third is the tunneling resistance R_t (resistance between CNTs that are separated by a small insulating layer)[126]. The change of intrinsic resistance under applied strain is much smaller than the change of other two types of resistances, thus the variation of intrinsic resistance become irrelevant on the electrical behavior of the composite strain sensor. Based on this description, the overall resistance change is mainly attributed to the change of Rc and Rt:

$$\frac{\Delta R}{R_o} = \frac{\Delta R_C + \Delta R_T}{R_o} \quad (2)$$

According to the previous report, CNTs could be regarded as elastic materials[146], thus at low strain, most of the CNTs are still connected, the change of the tunneling resistance is a dominant phenomenon. Tunneling resistance is usually expressed by the equation below[147]:

$$R_T = \frac{1}{C_1}\frac{d}{\sqrt{K}}\exp(C_2\sqrt{K}d) \tag{3}$$

The constants C_1 and C_2 are $3.16\text{x}10^{10}$ and 1.0125, respectively. K is the height of the energy barrier (1ev for PDMS)[138], and d is the distance between CNT ends. At low strain, $\Delta R/R_o$ could be defined as follows:

$$\frac{\Delta R}{R_o} \approx \frac{\frac{1}{C_1}\frac{d}{\sqrt{K}}\exp(C_2\sqrt{K}d) - \frac{1}{C_1}\frac{d_0}{\sqrt{K}}\exp(C_2\sqrt{K}d_0)}{\frac{1}{C_1}\frac{d_0}{\sqrt{K}}\exp(C_2\sqrt{K}d_0)} = \frac{d}{d_0}\exp(C_2\sqrt{K}(d - d_0)) - 1 \tag{4}$$

Where d and d_0 are the distance between CNT ends under the applied strain and the un-stretched state, respectively. The d could be assumed as:

$$d = (1 + \varepsilon)d_0 \tag{5}$$

According to equation:

$$\ln(\frac{\Delta R + R_o}{R_o}) \approx \ln(1 + \varepsilon) + 1.0125d_0\varepsilon \tag{6}$$

By fitting the line, we can get d_0=3.9A,

$$\frac{\Delta R}{R_o} = (1 + \varepsilon)\exp(3.95\varepsilon) - 1 \tag{7}$$

Figure 36 shows the experimental data match well with the theoretical model used in equation (7).

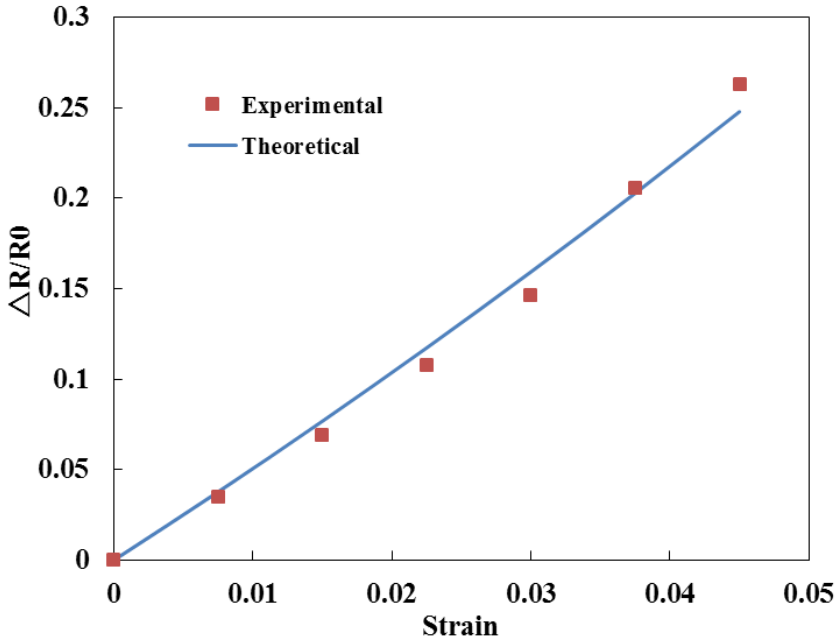

Figure 36. Experimental data and analytical solution of relationship between resistance change and strain change.

The transition from the non-sensitive to sensitive region, i.e. the strain at which the contact areas of CNT network start reducing significantly and the crack starts to form, is defined as critical strain. At high strain, the cracks generate and propagate in CNT networks under stretching, which significantly limit the electrical conduction through CNT networks. With increasing of strain, the number and width of cracks also increase, but as shown in SEM image in Figure 37, some CNT networks still bridge the cracks, preventing the entire rupture of conduction network. Figure 37 schematically depicts the resistance change mechanism under stretching in CNT networks. To understand the resistance change behavior, we developed a simple model to describe it.

Crack density could be described as:

$$\rho = A(\varepsilon - \varepsilon^{c}) \tag{8}$$

where A is a constant that equal to $A = \frac{E}{2h\sigma}$

And resistance change could be expressed approximately as

$$\frac{\Delta R}{R_o} = B\varepsilon + C\rho^n \tag{9}$$

B is the piezoelectric constant of the composites, C and n are the constants related to matrix cracking.

$$\frac{\Delta R}{R_o} = B\varepsilon + CA^n(\varepsilon - \varepsilon^c)^n \tag{10}$$

By fitting the data in Figure 36, constant B and C could be obtained as:

$$\frac{\Delta R}{R_o} = 7.89\varepsilon + 31.05(\varepsilon - \varepsilon^c)^{0.95} \tag{11}$$

The experimental data also fits well with this analytical solution at high strain, as shown in Figure 38. Therefore, the overall resistance change as strain increases could be described as:

$$\frac{\Delta R}{R_o} \approx \begin{cases} (1+\varepsilon)\exp(3.95\varepsilon) - 1 & (0 \le \varepsilon < \varepsilon^c) \\ 7.89\varepsilon + 31.05(\varepsilon - \varepsilon^c)^{0.95} & (\varepsilon \ge \varepsilon^c) \end{cases} \tag{12}$$

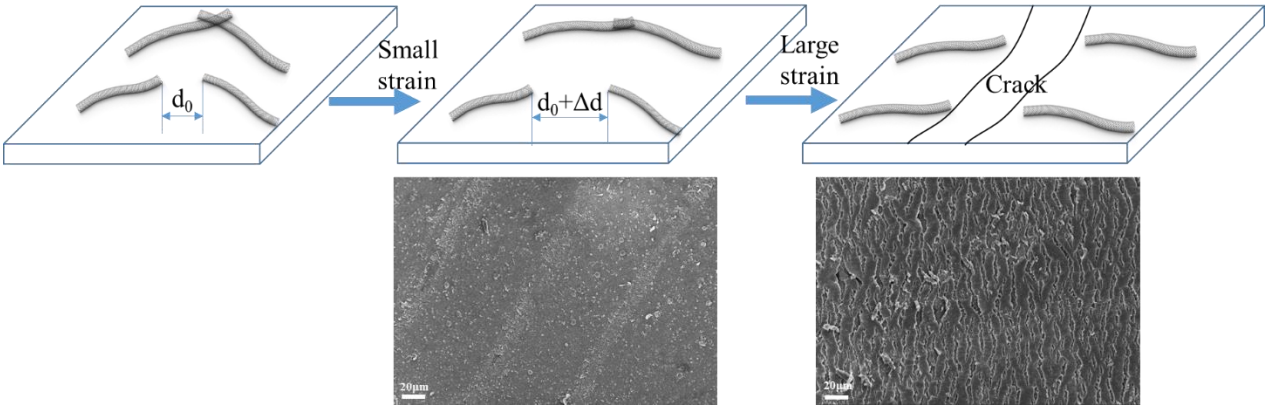

Figure 37. Resistance change mechanism under stretching in CNT networks

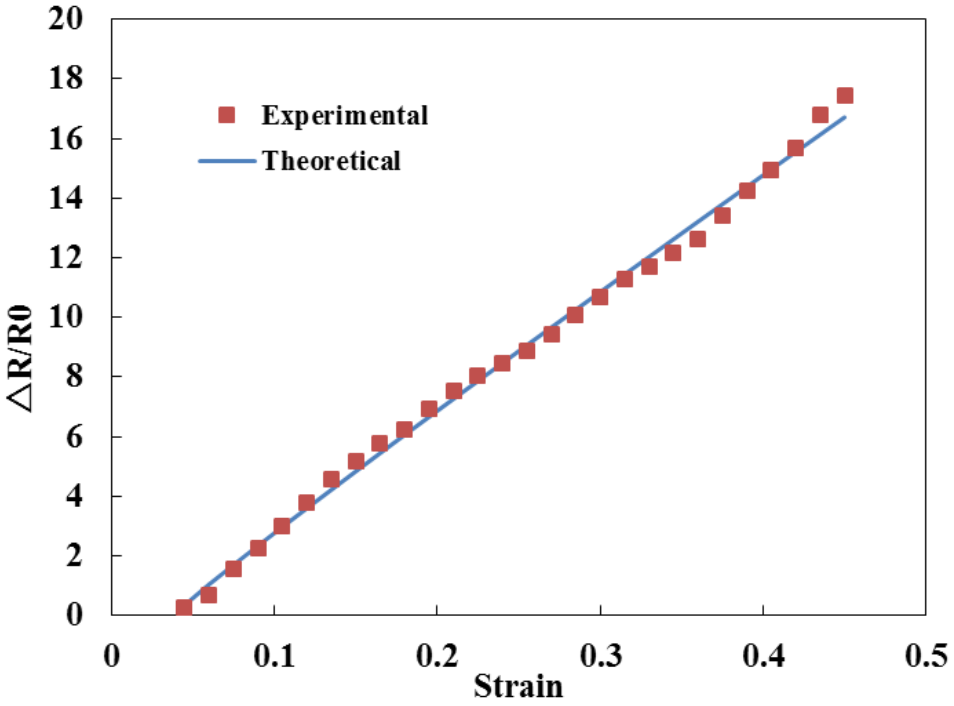

Figure 38. Experimental data and analytical solution of relationship between resistance change and strain change at high strain

The highest gauge factor obtained in this study is 35.75 of the CP50 sensors, which is higher than the value of most recently reported composite strain sensors. Moreover, the CNT/PDMS strain sensors were capable of measuring tensile strain up to 45%, which is more desirable for monitoring human motions compared to commercially available metallic strain gauges. Generally, the joint movement of human body results in less than 50% strain[137], thus the fabricated composite strain sensors holds a great promise for monitoring human motions.

To examine the response repeatability and durability of the strain sensors, repeated stretching and releasing cycles were applied to strain sensors. Figure 39(a) shows the resistance change of CP50 sensor at the first stretching/releasing response. It demonstrated that the sensors exhibited a fully recoverable electrical resistance with negligible hysteresis upon the releasing of strain. This could

be attributed to the strong interfacial bonding between the CNTs and PDMS in composite sensors, where the polymer matrix was tightly trapped in the dense CNT network. As shown in Figure 39(b), sensors under three different strain all present excellent resistance recoverability and reproducibility. Figure 39(c) shows the long-time piezo-resistive behavior of CP50 composite strain sensor during 100 stretching-releasing cycles. The electrical resistance change at 30% strain maintained constantly at the beginning couples of cycles, but over 60 cycles, the electrical resistance change starts to show a slight increase gradually. This could be interpreted by the permanent damage of the CNT conductive networks. After high number of loading-unloading cycles, the cracks in the network propagate resulting in the unrecoverable resistance change. Figure 39(d) represents the resistance change at 45% strain plotted as a function of the loading cycle numbers and the drift of resistance change is only 20% after 100 cycles, indicating a good durability for practical application.

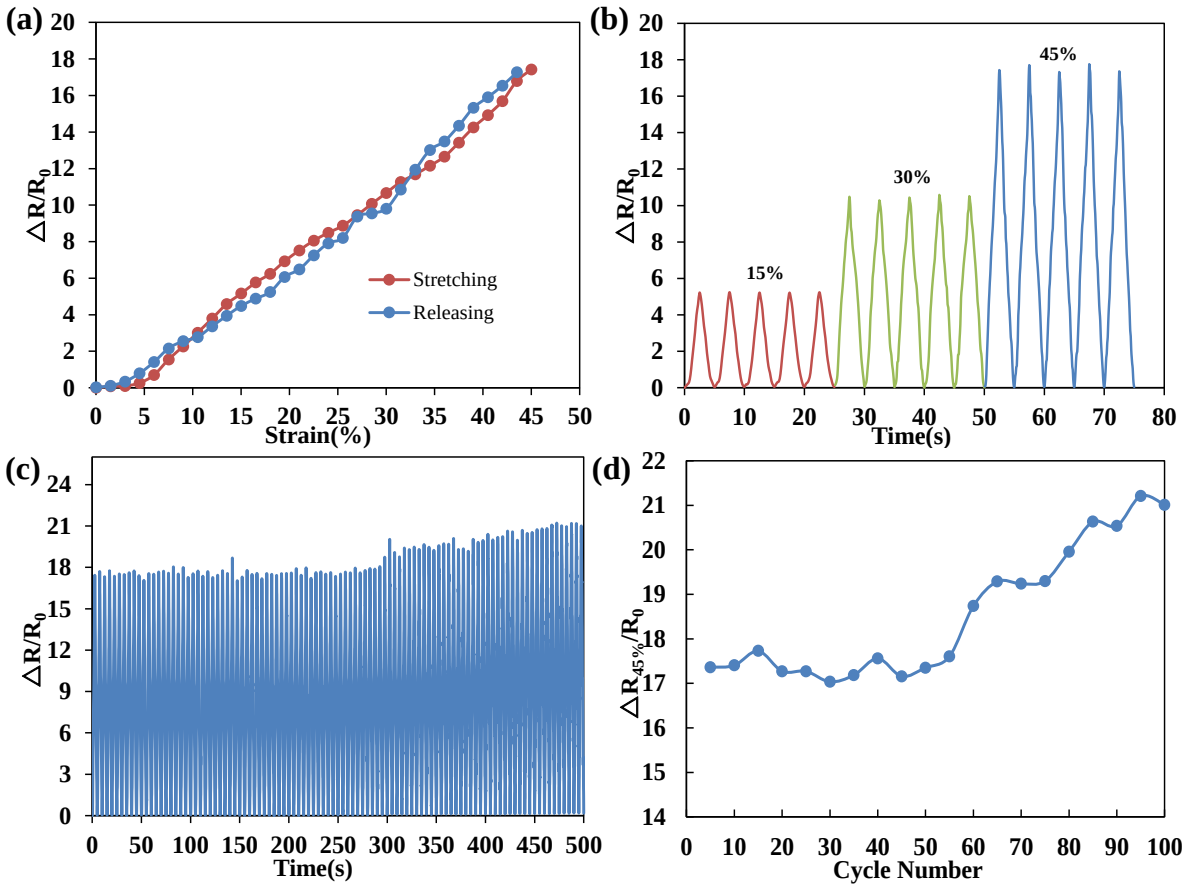

Figure 39. Pieoresistive response of CP50 (a) at first stretching/releasing cycle (b) under different strains (c) during 100 loading-unloading cycles; (d) at 45% strain plotted as a function of the loading cycle numbers

In practical application of the strain sensor, environmental factors such as temperature should be taken into consideration. Hence, we studied the dependence of piezoresistive behavior of composite strain sensors on temperature. Figure 40 shows that the resistance increases shapely as temperature increases at low temperature (less than 50), indicating a positive temperature coefficient trend. This could be explained by the difference between thermal expansion coefficient of PDMS and CNTs(for PDMS: ~3.2×10^{-4} K^{-1}, for CNT: ~1 to 2×10^{-5} K^{-1})[148, 149]. When

temperature increases, PDMS expands a lot resulting in larger distance between conductive CNTs so that the resistance increases. Interestingly, at higher temperature, the electrical resistance keeps unchanged even slightly decreases as temperature increases. This is possibly because CNTs themselves usually exhibit show a negative thermal coefficient behavior (the resistivity decreases as temperature increases)[150]. As temperature increases, the electrons at inner metallic shells of CNTs could be thermally activated to participate electric conductance. Thus, at higher temperature, there is a competition between the resistance reduction results from expansion of CNT networks and the resistance increase results from the intrinsic resistivity decrease of CNTs, which leads to a slightly changed electrical resistance.

As shown in Figure 40(inset), the gauge factor decreases when temperature increases. The most possible reason proposed for this is the weaker binding resulting from the different thermal expansion ratio between PDMS and CNTs. When the binding is weaker, load transfer between PDMS and CNT network is inefficient so that the sensors turns to be less sensitive to the applied strain[146]. In addition, the un-stretched resistance of strain sensors increases a lot when temperature increases, thus compared with this original value, the resistance change is smaller and a lower gauge factor is achieved. The deviation of gauge factor in the temperature sensitivity is as low as 13.2%, which is even lower than the deviation caused by the manufacturing and test error (~15%). Therefore, the temperature effects on sensitivity could be compensated when measuring strains using the fabricated strain sensors. However, it should be noted that a hysteretic behavior of electrical resistance recovery was observed when temperature increased. This is probably due to the sliding of CNTs inside polymer matrix caused by the difference of thermal expansion ratio. After the release of strain, the moved CNT cannot rapidly return back to their original position which leads to the hysteresis[151].

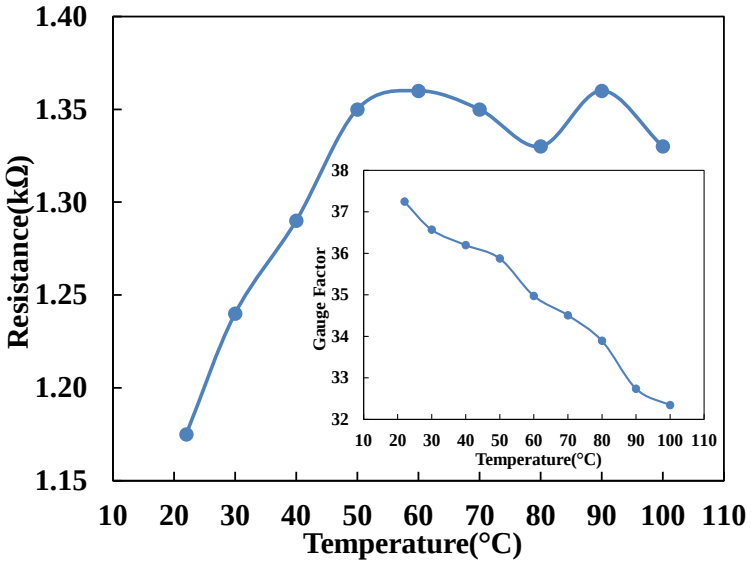

Figure 40. Dependence of piezoresistive behavior of composite strain sensors on temperature

The fabricated strain sensors can be used for wearable electronics applications, because they are flexible to be easily attached to human body parts. To examine their capability of monitoring human motion, the CP50 strain sensors were attached to human wrist to monitor diverse motions. To best of our knowledge, so far, all sensors only demo the capability of showing resistance change when human body moves, but the accuracy to quantification the muscle-induced strain was rarely reported. In this study, the strain data obtained from the correlated piezoresistive signal was compared with the actual strain information got from the camera system (the camera set up is shown in Figure 41). During the experiment, we attached 3 mm in diameter passive reflective markers to the strain sensor (4 on unidirectional-type sensor and 12 on rosette-type sensor). Kinematic data of markers location were acquired by using a 9-camera motion capture system (OptiTrack Prime 13W, NaturalPoint Inc., USA) at a frame rate of 240 FPS. We set the maximum

residual value to 2.7 mm, and completed the system calibration with a mean 3D error of 0.411 mm before the experiment.

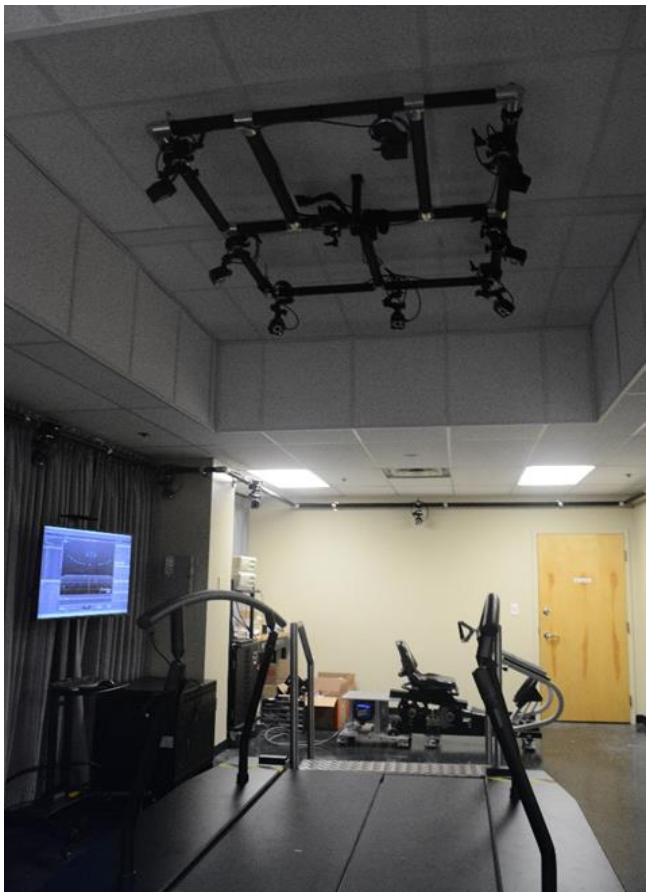

Figure 41. Camera systems for recording the strain data

As shown in Figure 42(a), we considered the relaxing straight wrist as the initial state. Three motions at different bending angles were carried out to evaluate the sensing performance of the composite strain sensor. Four markers were fixed on the top of the strain sensors and the camera system tracked the X-Y-Z locations of markers when marker moves. Figure 42(b) shows the location differences between markers when tester's wrist moves. Strains of wrist were calculated from the changes of distance between markers from initial state to bend state. The calculated strains

under different motions were shown in Figure 43(a). When the wrist of tester moves, the strain sensors recorded specific resistance signal changes (Figure 43 (b)) for each motion. The similar signal changes were observed when the same motion were repeated, which represents a good durability of fabricated sensors for monitoring motions. By using the gauge factors obtained from previous tensile tests, maximum trains for three motions were calculated as 5.49%, 13.39% and 23.65%, respectively. The strains obtained from strain sensor were slightly larger than the strain obtained from camera, as shown in Figure 44(a). This is possibly because the camera recorded strain is obtained by calculating the linear distance between the two markers, but actually the strain sensors curved a little bit when wrist bend, and the actual strain is larger than the calculated value. However, the strain sensor represents the actual strain value when wrist bend. Thus, there is a slightly difference between the camera recorded strain and strain sensor recorded strain. Figure 44(b) shows the maximum strains recorded by camera and strain sensors under diverse motions, and the difference is less than 20%, indicating that strain sensors could be used to accurately quantify the amount of muscle-induced strain.

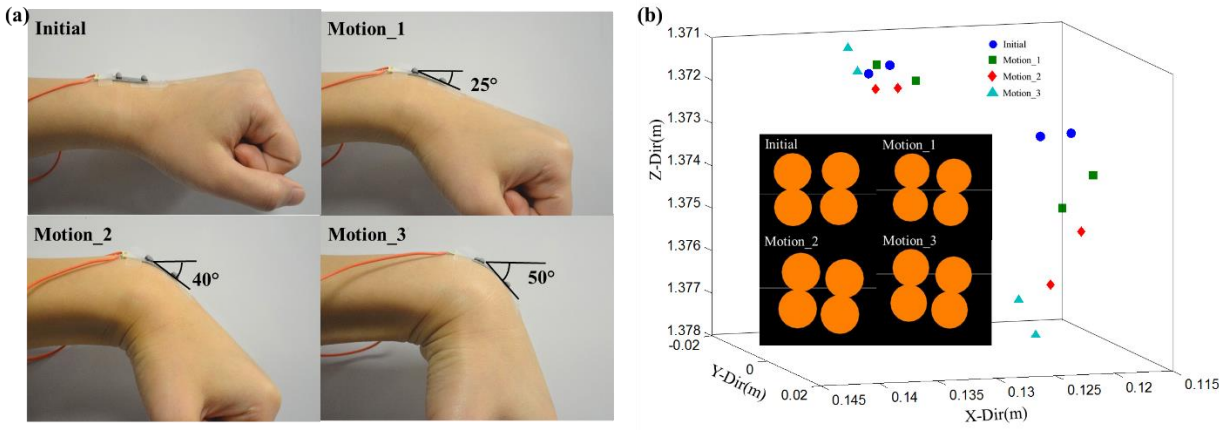

Figure 42. (a) Photographs of the unidirectional strain sensor attached to tester's wrist with three different motions; (b) location differences between markers when tester's wrist moves

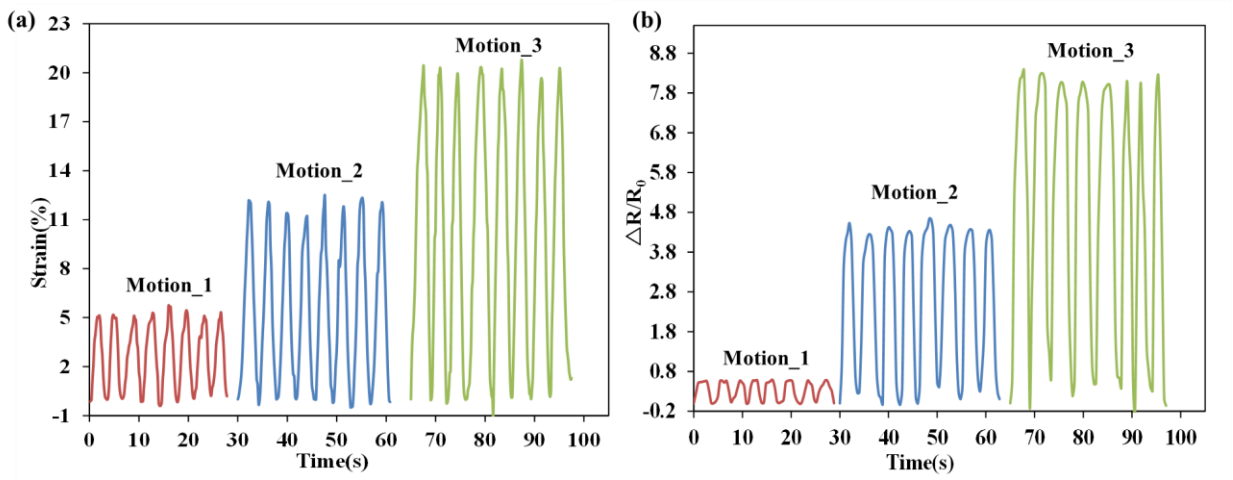

Figure 43. (a) Strain profile obtain from camera; (b) electrical resistance signal changes of strain sensor;

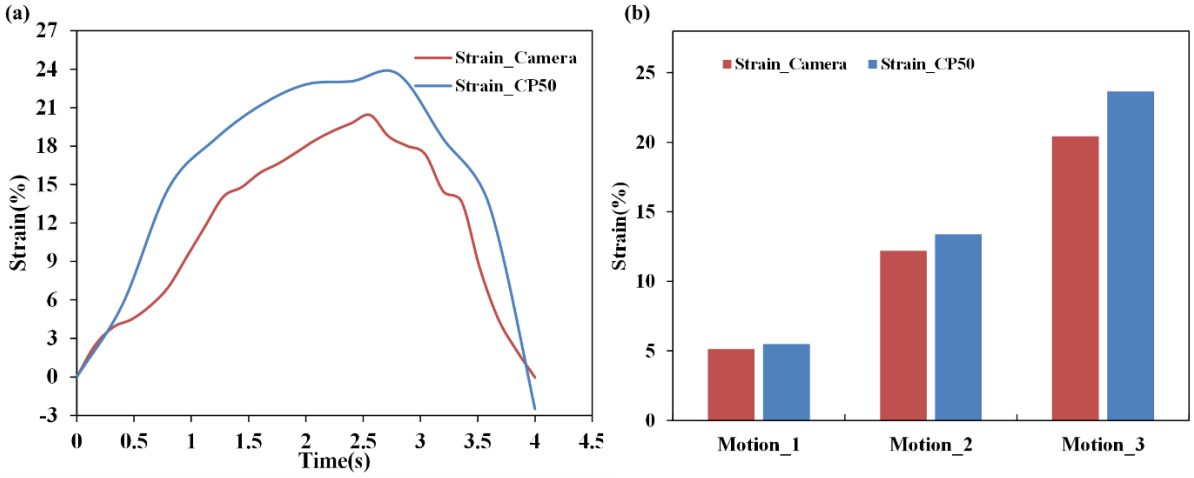

Figure 44. (a) Comparison of strain obtained by camera with strain obtained by strain sensor in first bending cycle (b) maximum strains recorded by camera and strain sensors in first bending cycle under diverse bending angles

Human body deformation is generally multidirectional, which cannot be accurately monitored by single-directional strain sensors. Due to flexibility of the SDM fabrication, muti-axial strain

sensors were fabricated to monitor complicated strain. A rosette-shaped strain sensor was fabricated with an intersecting angle of 120°. As shown in Figure 45, the fabricated rosette-shaped strain sensor was mounted on the tester's wrist. Figure 46(a) shows the strain recorded by camera of each individual strain sensors during the cyclic bending motions of wrist. Figure 46(b) shows the corresponding electrical resistance changes of each individual sensors. Maximum strains calculated from the signal changes of three individual sensors were 6.29%, 2.45% and 0.82%, respectively, which is only slightly different from the strain recorded by camera, indicating the accuracy of the strain sensors to monitor the human motions. In particular, the strain along the direction of bending is larger than other directions, which is reasonable that during the bending of wrist, the major deformation is along the bending direction. Additionally, using this multi-direction strain sensors, the strain along other direction could be identified. According to the defined coordinated system and equations, the principal strain and their angle of orientation was calculated to be 6.43% and 8.4°, enabling to monitor complicated human motions.

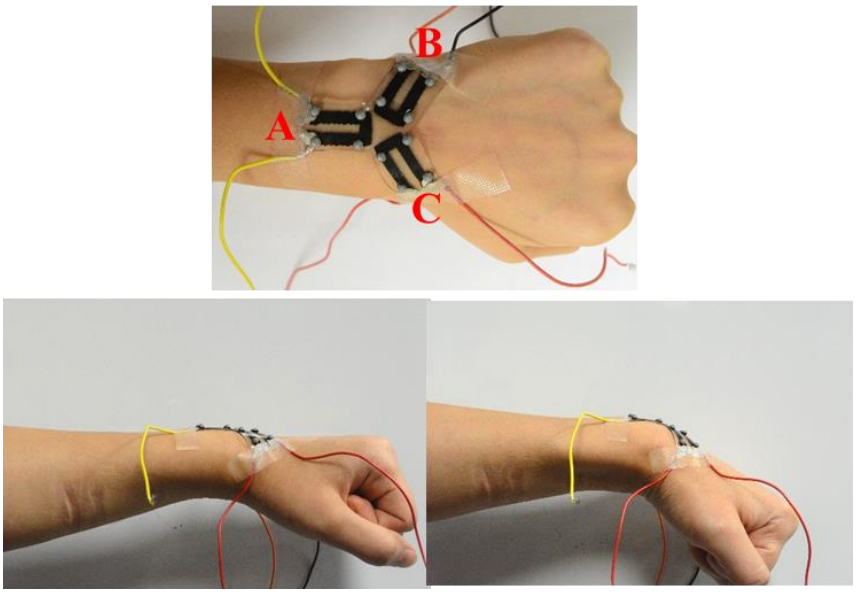

Figure 45. Photographs of the rosette-type strain sensor attached to tester's wrist

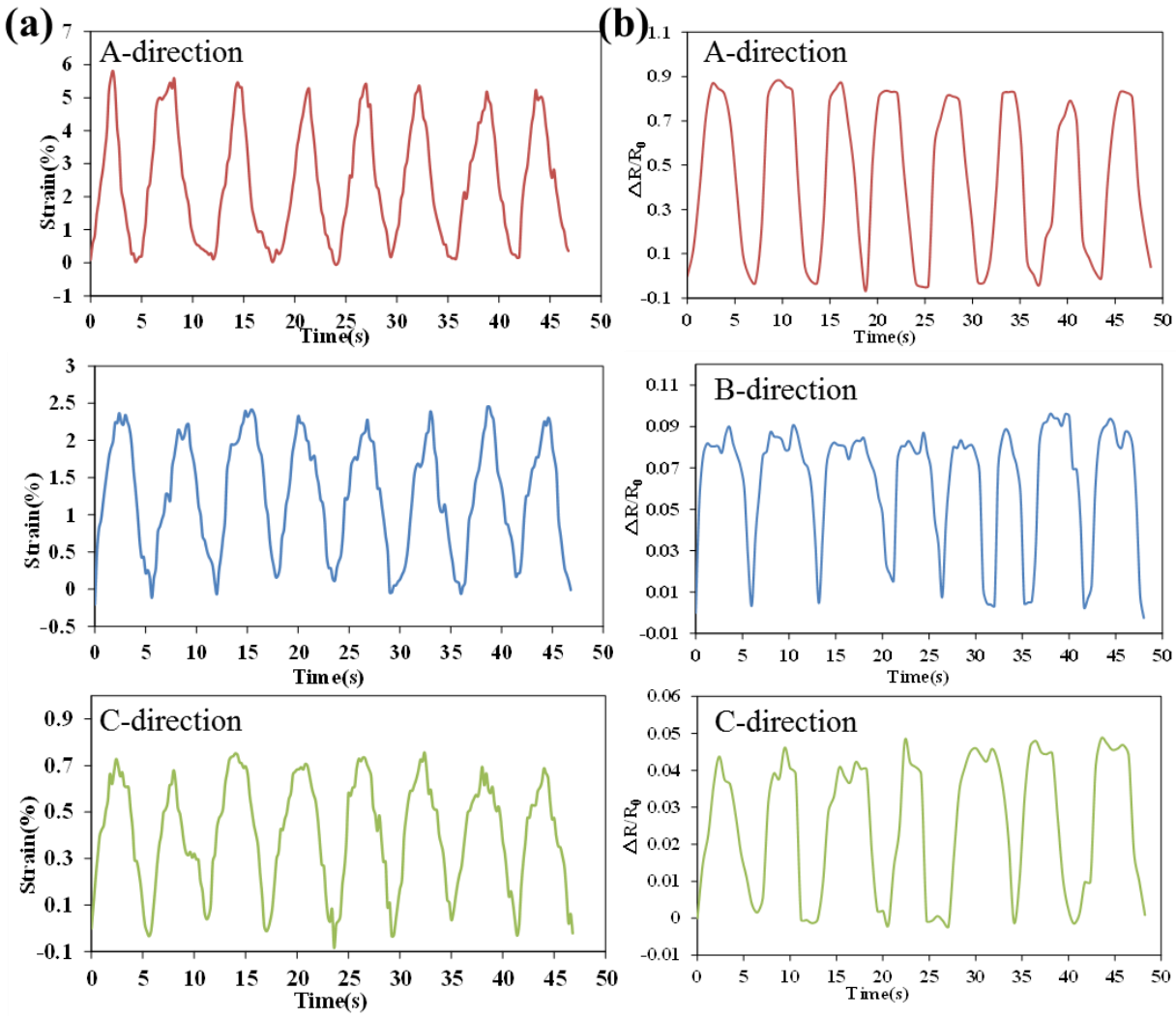

Figure 46. (a) strain recorded by camera of each individual strain sensors (b) electrical resistance changes of each individual sensors

5.4. Conclusion

In summary, CNT/PDMS strain sensors were fabricated by printing a CNT dispersion on PDMS substrate using SDM device, which is a digitally-controlled, cost-effective, additive and continuous process. The fabricated strain sensors show a high strechablity (~45%) and high

sensitivity (~35 gauge factor) as well as good linear relationship between the applied strain and electrical resistance change. Furthermore, the CNT/PDMS strain sensor showed small hysteresis and excellent durability under cyclic loading-unloading. The printing cycles of CNT layer could be controlled to tune strain gauge factor according to the requirement. We also demonstrated that using the digital printing technique, unidirectional or multidirectional strain sensors could be manufactured to monitor complicated deformation of human motion. Besides, the strains obtained from CNT/PDMS sensors were compared with the camera recorded strain, and only less than 20% deviation was found, demonstrating the great accuracy of fabricated sensors to quantify the amount of strain. The facial fabrication of this high-performance layered CNT/PDMS strain sensors, combining their high sensitivity, strechability and accuracy, paves a new way for the fabrication of wearable strain sensors for monitoring human motions.

CHAPTOR SIX: SELF-HEATING PERFORMANCE EVALUATION OF THE CNT/TPU NANOCOMPOSITES

6.1. Introduction

Carbon nanotubes(CNTs) have become prominent smart materials due to their unique electrical and thermal properties[3, 152]. They are commonly used as an electrically conductive reinforcement to prepare conductive polymer composites[86, 114, 153, 154], which can act as electric heating elements for many industrial applications, such as deicing of aircraft[155], engine preheater[156] and plane heater[90]. In electric heating elements, electrical energy can be converted into heat energy through the process of joule heating[13]. Traditionally, electrical heating elements are made by metallic materials like Kanthal or nichrome[157]. However, the metal heating devices have several drawbacks such as easy oxidization, small heating area and low energy conversion efficiency[90]. Therefore, carbon nanotube reinforced polymer composites have attracted extensive attentions for their potential application as an electrical heater due to their light weight, oxidization resistance, low manufacturing cost and high energy efficiency[12-17]. Isaji et al.[14] investigated the heating performance of carbon nanotube/polyethylene composite films, and the maximum surface temperature of their films can reach 125°C within less than 100s when electrical power was up to 1.73W. Yan et al.[17] also reported a composite film that consists of carbon nanotube and polydimethylsiloxane as electric heating elements, and a maximum temperature 150°C was obtained even at a low applied power of 0.8W. These quick heating behaviors suggested that carbon nanotube based conductive composite is a promising candidate as a high efficient electric heater.

While these CNT/SMP composites showed a quick temperature raising, some challenges in their fabrication and properties have prevented their widespread industrial applications. For instance, for SMP composites using mixed carbon nanotubes, it is difficult to disperse carbon nanotubes homogeneously, thus to obtain the desired electrical resistivity, higher loading of carbon nanotube is required, which may lead to high manufacturing cost and processing difficulties. For SMP composites using carbon nanotube buckypapers, their electrical resistivity is usually extremely low so that the electrical current may concentrate at sharp corners and may cause the local overheating problem.

Fabrication of composites using digital printing technique is an efficient way to address some of the above-mentioned problems, since it can provide process flexibility as well as well-designed composite properties[55, 158, 159]. This study developed a spray deposition modeling(SDM) technique for fabricating CNT/SMP composites with desirable self-heating and actuation properties. SDM is a digital fabrication process that similar to the conventional inkjet printing technique, but SDM is an additive manufacturing process that is capable of fabricating carbon nanotubes (CNT) layers with variable thickness and arbitrary patterns to obtain the tunable properties in defined locations. In this paper, shape memory polymer composites incorporated with printed carbon nanotube layers were manufactured and investigated. The investigations were focused on the electrical heating performance and shape recovery behaviors of obtained CNT/SMP composites.

6.2. Characterization

The surface morphology of CNT/SMP nanocomposites was examined using a scanning electron microscopy(SEM, Zeiss-Ultra 55) under an accelerating voltage of 10kV. Prior to testing, the

specimens were sputter-coated with a thin layer of platinum-gold to reduce charging artefacts for clearer view. The sheet resistance of CNT/SMP nanocomposites was measured at room temperature with a four-point probe apparatus(Signatone Quadpro system). The surface thermal images and the surface temperature of CNT/SMP composite were obtained using an infrared temperature camera(FLIR E30). The voltage was supplied by a DC power supply(Volteq HY10010EX).

6.3. Results and Discussion

6.3.1 Structure and morphology

To identify the surface morphology of the pristine CNT layers on SMP films, surface SEM images of CNT layers obtained by 50 printing cycles was shown in Figure 47(a). Pristine CNT layers were found to be uniformly deposited on the SMP substrates, which can be attributed to the homogeneous dispersion of CNT in the aqueous solution and the effectiveness of the optimized SDM process. A dense CNT network was formed by the entangled CNTs due to van der Waals forces, electrostatic forces, and $\pi - \pi$ interactions between the CNTs. The surface morphology, cross-section morphology under low and high magnification of CNT/SMP composites after the hot-pressing process were shown in Figure 47(b)-(d), respectively. In the Figure 47(b) and (d), regions with dark color indicated the SMP polymer matrix and the brighter spot indicated the distribution of CNTs. It was observed that the SMP resin fully impregnated throughout CNT networks and a continuous CNT network was established in CNT/SMP composite. The thickness of embedded CNT layers with 50 printing cycles was 3.5μm, as shown in Figure 47(c).

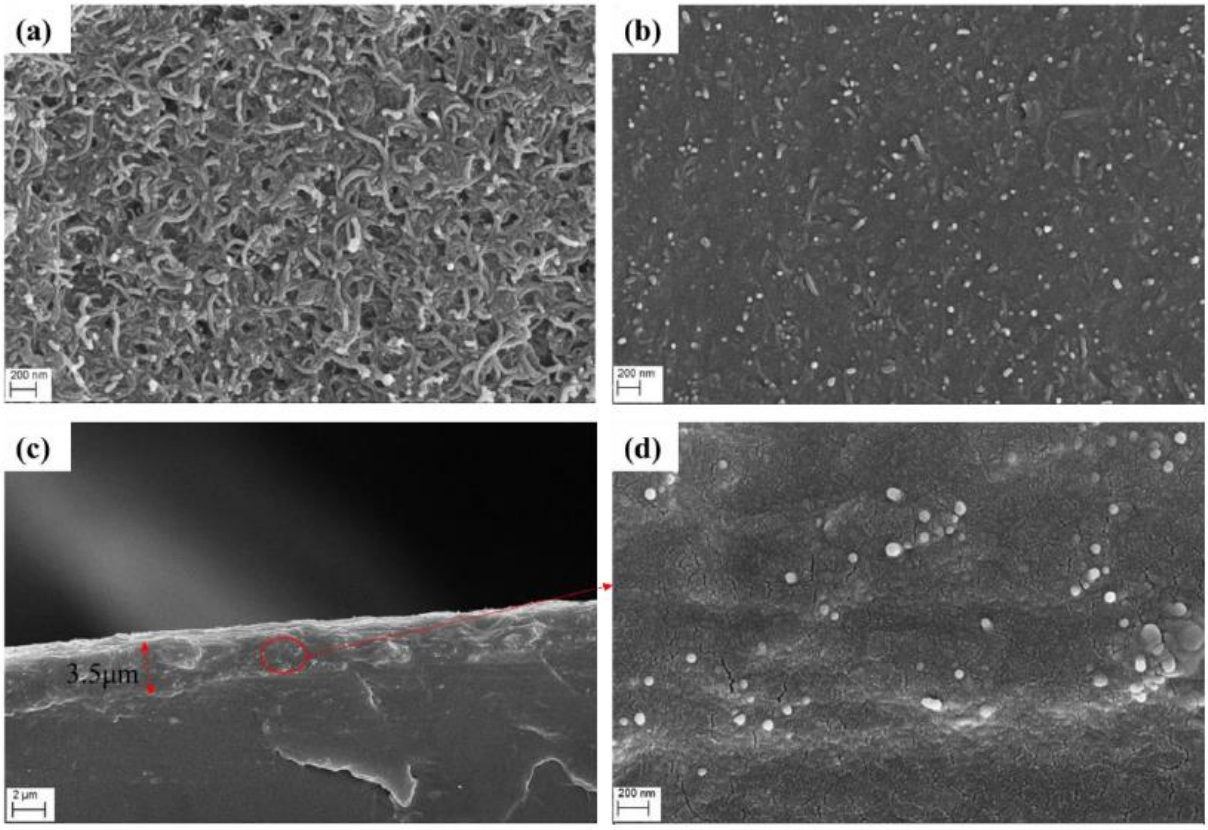

Figure 47. SEM images of (a) surface of pristine CNT layers with 50 printing cycles; (b) surface (c) cross-section under low magnification (d) cross-section under high magnification of CNT/SMP composites with 50 printed CNT layers

6.3.2 Electrical resistance analysis

The sheet resistances of printed CNT layers before resin infiltration and CNT/SMP composites were measured by four-point probe apparatus. Figure 48 showed the relation between sheet resistance and the number of printed CNT layers. When the number of printed CNT layers increases, the sheet resistance of printed CNT layers decreases in a power law. This is because that thicker CNT layers offer more continuous conductive paths to reduce electrical resistivity. Further

compacting and distribution of the nanotube network as the number of printed layer increases also contribute to the decrease of sheet resistance. With 50 layers CNT printed, the sheet resistance of CNT layers is 22.96Ω /sq, which is much lower than the value ~760Ω /sq [119] and ~78Ω /sq[120] of fabricated CNT films in previously published articles.

As shown in Figure 48, the sheet resistance of CNT/SMP composite does not show a significant increase compared with that of printed CNT layers before resin infiltration, although the SMP resin around CNT networks is insulating. It indicated that the conductive CNT networks were not impeded by the infiltrated resin. This can be explained by the conducting mechanism of CNT networks. The electrical resistance in CNT networks are mainly attributed to the intertube resistance(the resistance of tubes that are physically in contact)[126]. The infiltrated resin was just coated on the surface of CNTs and does not break the formed CNT junctions. Thus, the sheet resistance of CNT/SMP did not increase a lot compared with that of pure CNT layers and also showed a power-law decreasing. This result also indicated that the sheet resistance of CNT/SMP composite could be tuned by adjusting the printed numbers of CNT layers, thus the electric heating behaviors of CNT/SMP composite could also be controlled. Table 5 compares the electrical resistivity of our fabricated CNT films with those of reported inkjet-printed CNT films. It shows that our CNT films exhibit excellent electrical properties with less number of printing cycles due to the effectiveness of the SDM technology and dispersion method used to prepare CNT inks.

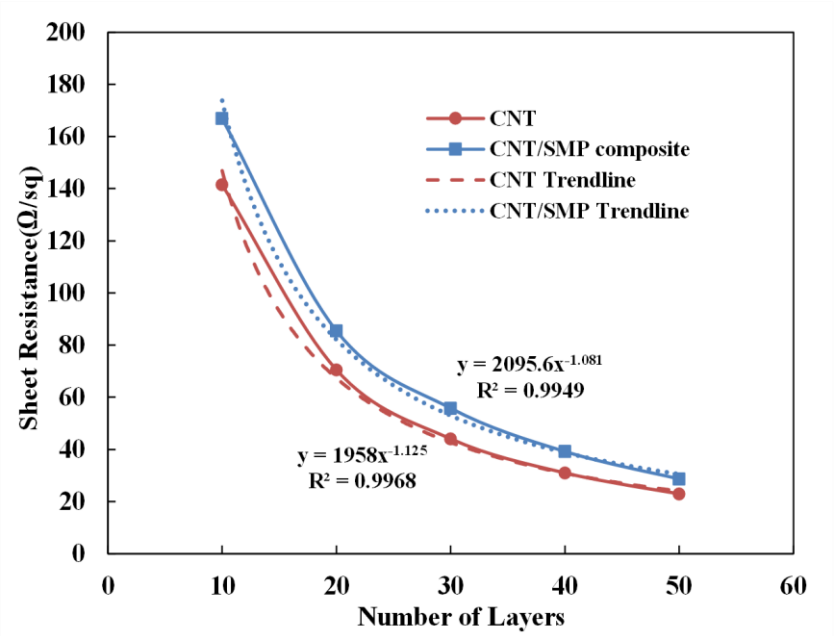

Figure 48. Sheet resistance curve of pristine CNT layers and CNT/SMP composites with different numbers of printed CNT layers

Table 5. Comparison of electrical resistivity of CNT films

Printer	Solvent	Concentration(mg/ml)	Sheet Resistivity(Ω/sq)	Ref
Dimatix	DMF	0.4	150 with 25 prints	[160]
Microjet	DMF	0.02	333 with 8 prints	[161]
Epson	water	0.2	78 with 200prints	[162]
Epson	water	0.15	760 with 12prints	[119]
SDM	water	0.5	22 with 50prints	

6.3.3 Electric heating performance analysis

Due to the flexibility of SDM fabrication method, CNT/SMP composite with different heating patterns could be obtained. In Figure 49(a), three patterned CNT/SMP composites were obtained as(I) a rectangular area(II) a semi-circle area(III) a spiral line area of printed CNT layers. Contact pads at the end of the patterns were designed for attaching the wires using silver paste. Their thermal images were obtained when certain voltages were applied. It was found that the surface temperature does not show many variations in central locations with printed CNT layers, which confirms the uniformity of fabricated CNT/SMP composites. The temperature on the edge of composites was lower due to the heat exchange between the heated composite and the unheated atmosphere. In the previous reports[12-14], all self-heating composites only had simple rectangular heating patterns, whereas in our report, using digital controlled SDM method, composites that had arbitrary heating pattern could be manufactured, which indicating that electric heating could be accurately applied at desired locations.

The fabricated CNT/SMP composite were not only designed for areas needing even temperature distribution, but also designed for areas needing thermal gradient. Figure 49(b) showed the CNT/SMP composite that was fabricated with different numbers of printed CNT layers in five districts. In the five consecutive districts from left to right, the composite contains 10, 20, 30, 40 and 50 printed CNT layers at each district, respectively. These five districts could act a series circuit with five resistors. In a series circuit, the heating power is proportional to the resistance and the square of resistor current. Since the electrical current is same for each resistor and thus, the differences in heating power between each resistor are determined by their resistance. The district with more printed CNT layers has lower resistance and lower heating power, thus has a lower

surface temperature. Under a constant voltage of 30V, the highest surface temperature observed at the location with 10 printed CNT layers is 64°C, whereas the lowest surface temperature observed at the location with 50 printed CNT layers is 52°C. Consequently, through designing the number of printed CNT layers, we observed a temperature gradient on the surface of CNT/SMP composites. Therefore, by using SDM technique, it is convenient and flexible to manufacture CNT/SMP composites that used for heating areas need uniform temperature distribution or area needs different temperature at different locations.

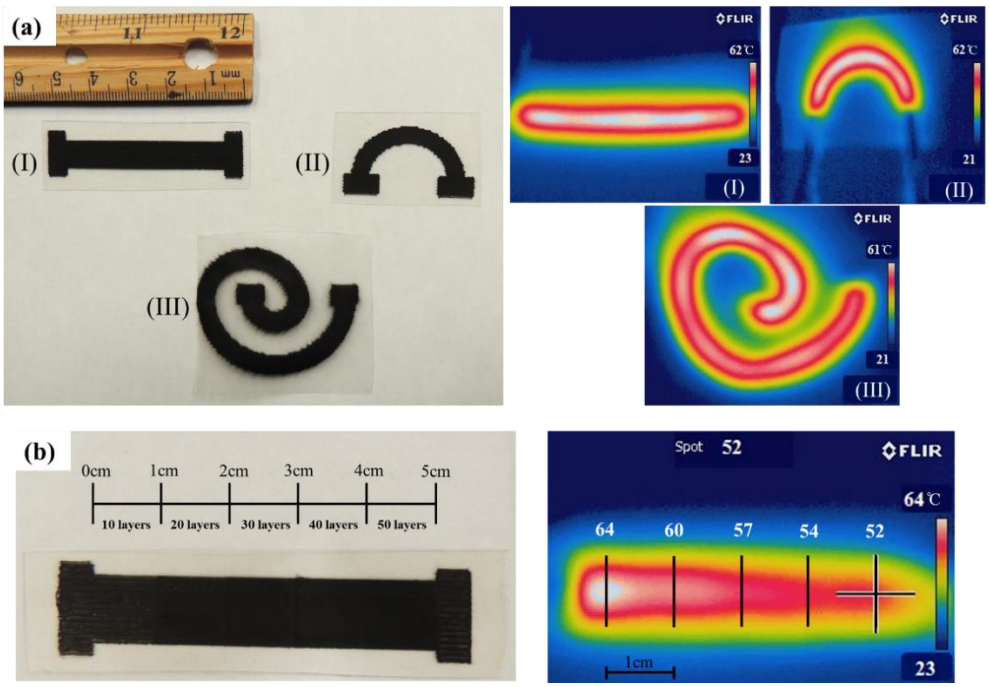

Figure 49. Left: CNT/SMP composites that has (I) rectangular (II) hemi-sphere area(III) spiral line shaped CNT layers. Right: Corresponding temperature distribution thermal images (b) Left: CNT/SMP composites that has different numbers of printed CNT layers in five districts. Right: Corresponding temperature distribution thermal images

To further investigate the electric heating performance of CNT/SMP composites, fabricated specimens were evaluated at different power densities. CNT/SMP composites with "U" shaped CNT patterns were fabricated with different numbers of printed CNT layers from 10 to 50 layers with an interval of 10 layers. For simplicity, we named the CNT/SMP composites with 10 printed CNT layers as CS10, with 20 printed CNT layers as CS20, and so on. Figure 50 shows the change in resistance of CS30 and CS50 specimens as temperature increases. Both of them showed a negative thermal coefficient effect, which means the resistance decrease as temperature increases. One possible reason for this phenomenon is the increased electron mobility as temperature increases. Additionally, the thermal expansion of polymer matrix may result in the compaction of CNT networks, which results in the decreasing of resistance[163]. Figure 51(a) shows the rising process of surface temperature of CS50 specimen under power densities. As Figure 51(a) shows, the surface temperature increased sharply in a short period of time after the voltage was applied, but as time goes, the surface temperature gradually reached to its maximum point, which is called as steady-state temperature. At the steady state, the input electrical power is balanced by the dissipated power, thus the surface temperature can keep stable at equilibrium state. The steady-state surface temperature of CS50 specimens increases when the power density increases. Time evolution of temperature increasing for CS30 was also investigated, as shown in Figure 51(b). Similar electric heating behaviors were also observed for CS30 specimens. Steady-state temperature dependence on the input electrical power for CS30 and CS50 was plotted in Figure 51(c). It was observed that the relationship between steady-state temperature and input power for these two specimens was almost identical, with a slope of 286.39°C/(W/cm^2), indicating that the final steady-state temperature of heating elements are mainly determined by the given input electrical power rather than the electrical resistance of specimens. However, the operation voltage

required to reach the steady-state surface temperature was reduced by increasing the number of printed layers. For instance, to reach temperature around 90°C, CS50 composite requires an input voltage of 40V, whereas CS30 composite requires a higher input voltage of 50V.

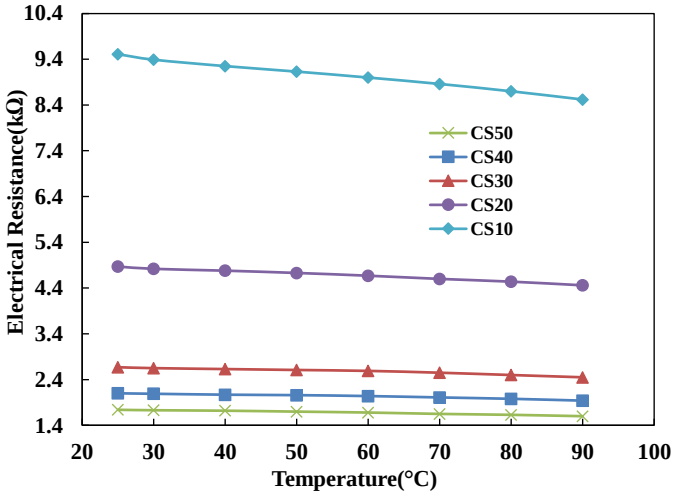

Figure 50. Temperature-dependent electrical resistance of composites different numbers of printed CNT layers.

In a heating system, the temperature is balanced between input power and heat loss including convective and radiative heat loss[164]. In our experiment, the specimens were only heated to low temperature(less than 100°C), so the radiative heat loss can be negligible[165]. Thus the temperature could be described by the following equation:

$$mc\frac{dT(t)}{dt} = VI - Q_c \tag{13}$$

where m, c, T and t are the mass, specific heat capacity, surface temperature and time, respectively. V, I and Q_c are input voltage, corresponding current and convective heat loss. Convective heat loss can be expressed by:

$$Q_c = hA(T - T_0) \tag{14}$$

where h , A and T_0 are the convective heat-transfer coefficient, surface area and initial temperature. By solving the equation(2), we got equation:

$$T_m = \frac{VI}{hA} + T_0 \tag{15}$$

where T_m is the maximum temperature at the steady state. It is obvious that the steady-state temperature is linear proportional to the input power, thus the experimental data shown in figure 51(c) is fitted with the theoretical solutions. By fitting the power density and maximum temperature curve, convective heat transfer coefficient h is obtained as 16.7 W/m^2K. Usually, heat capacity could be expressed as:

$$c = AT + B \tag{16}$$

Thus, a theoretical equation could be used to describe the heating performance of the fabricated composites:

$$m(AT + B)\frac{dT(t)}{dt} = VI - hA(T - T_0) \tag{17}$$

By fitting the experimental data in Figure 51, A and B could be obtained for CS30 as:

$$m(0.0028T + 0.065)\frac{dT(t)}{dt} = VI - hA(T - T_0) \tag{18}$$

The match between the experimental and analytical solution shows the accuracy of this model, as shown in Figure 52.

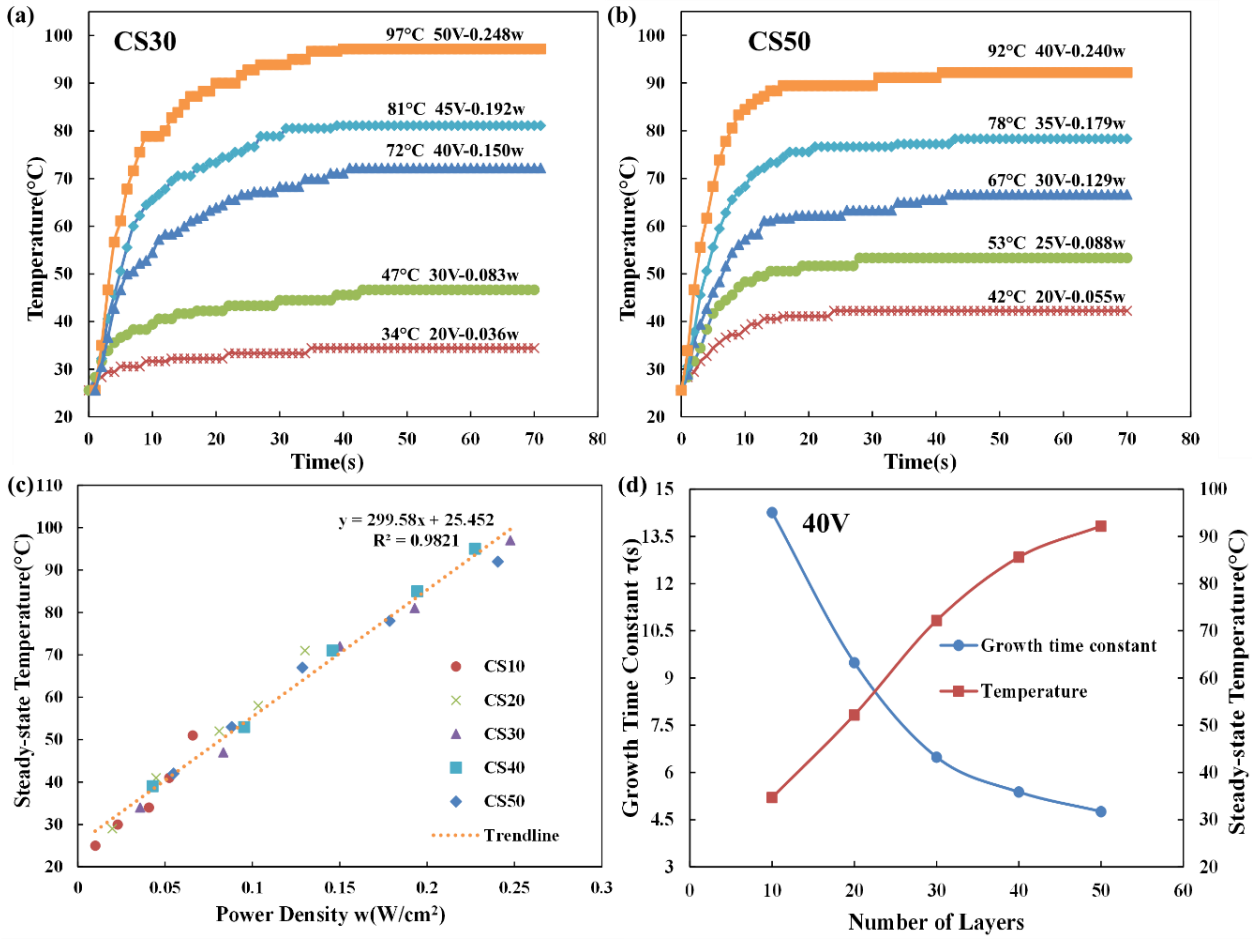

Figure 51. Time-dependent temperature of (a) CS30 and (b) CS50 composites. (c) Steady-state temperature as a function of input power density. (d) Steady-state temperature and time growth constant of composites with different numbers of printed CNT layers

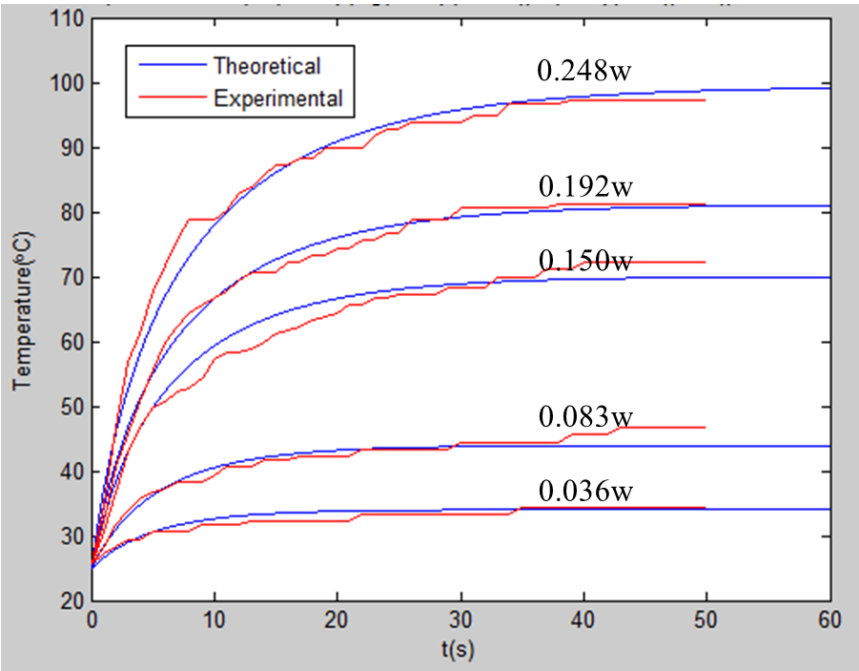

Figure 52. Experimental data and analytical solution of relationship between temperature change and time change

Abaqus software was also used to simulate the temperature increase as the time increases. In the simulation, heat convective coefficient used is 13.5 W/m^2K, which is smaller than the heat convective coefficient in analytical solution. This is because in analytical solution, conduction between CNT and polymer is neglected, thus the actual heat convective coefficient should be smaller than the value obtained from analytical solution.

The model setup of the polymer composites reinforced by carbon nanotube is shown in Figure 53. The polymer matrix will be heated when electrical power is applied to the U-shape carbon nanotube. According to the SEM images, the thickness of the carbon nanotube is around 10 μm. The thickness of the polymer matrix is around 60 μm. The carbon nanotube is embedded into the polymer matrix with one side attached to the polymer matrix and the other side is in the same plane

as the polymer surface. The dimensions of the U-shape carbon nanotube are also shown in Figure 53 .

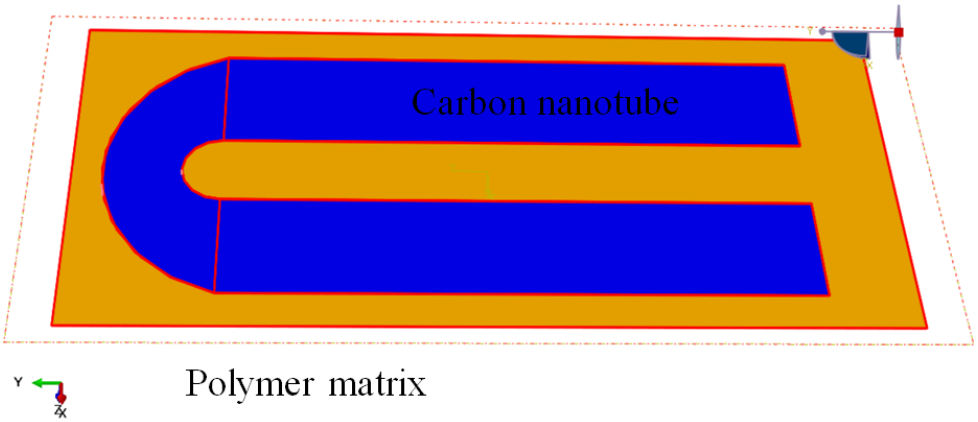

Figure 53. Model setup of the polymer composites reinforced by carbon nanotube

In the process of the heating the composites, the heat comes from the carbon nanotube and dissipate into polymer matrix and air. Between carbon nanotube and polymer matrix, the heat transfer mechanism is conduction and thermal conductivity plays a role in this process. Between the whole composites and surrounding air, the heat transfer mechanism is convection. As the temperatures of carbon nanotube and polymer matrix increases, the heat transfer between composites and air will increase to the level that equals to the heat generated by the carbon nanotube. When the equilibrium is reached, the temperatures of the composites material will be stable and keep a constant.

The heating process of the composites were studied using transient heat transfer analysis of ABAQUS. The model is composed of two parts: carbon nanotube and polymer matrix. The contact area between carbon nanotube and polymer matrix share the same nodes and therefore contact resistance is ignored in this analysis.

The mechanical and thermal properties are set as the following. The density of carbon nanotube is 1.3g/cm^3. The thermal conductivity of carbon nanotube is 3500 W/mK. The specific heat of carbon nanotube is dependent on the temperature and shown in Figure 54. For the polymer matrix, the thermal conductivity is 0.02 W/mK. The density is 1.2g/cm^3. The specific heat is 1.8 J/(g °C).

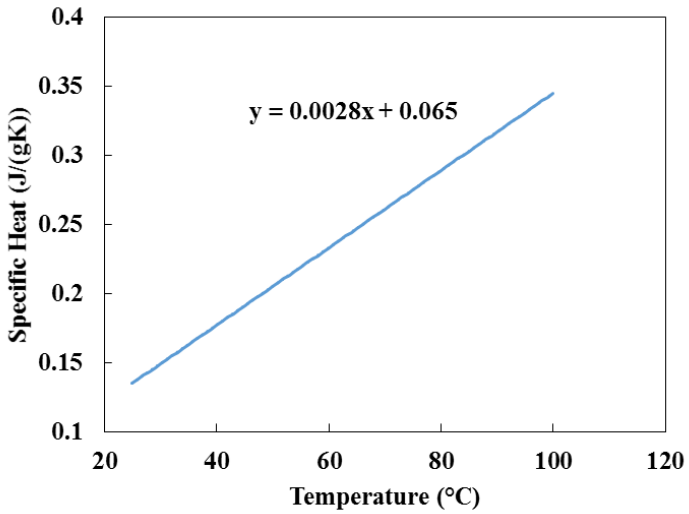

Figure 54. Specific heat of carbon nanotube dependent on temperature

The analysis type in this study is a transient heat transfer analysis with a time period of 100 s. Since there are heat convection between the composites and surrounding air, a surface film heat transfer condition is applied on both surfaces of the composites. The heat is generated in U-shape carbon nanotube. A body heat flux is applied to the U shape region throughout the simulation process. The initial temperature of the whole composites is set as room temperature 25 °C.

The simulation results of temperature evolution for the composites were shown in Figure 55. Heat flux magnitude evolution for the composites was shown in Figure 56. By using smaller heat convective coefficient, the simulated result match well with the experimental data (Figure 57 and 58), which indicating the accuracy of this capacity and heat transfer model.

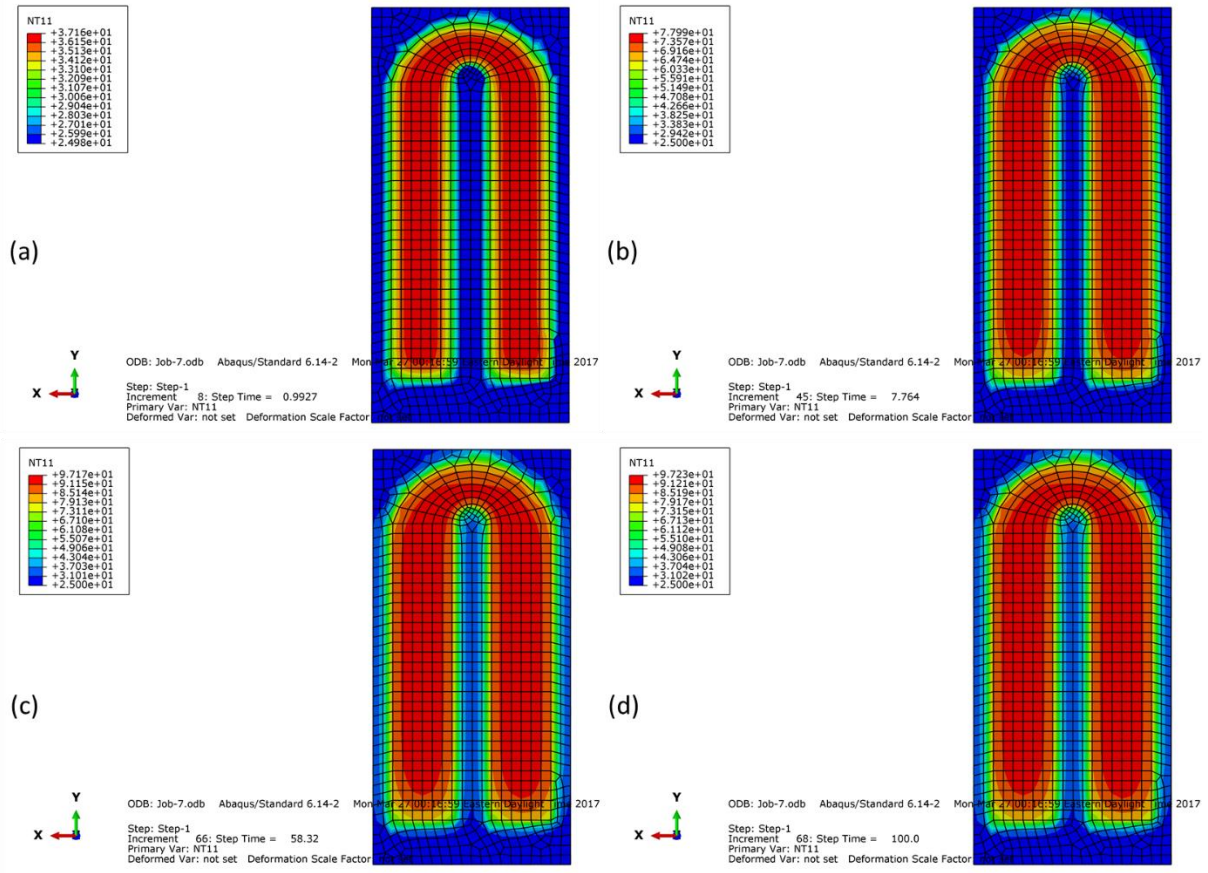

Figure 55. Temperature evolution for the composites (a) time = 0.9927 s (b) time = 7.764 s (c) time = 58.32 s (d) time =100s

The fast thermal response of CNT/SMP composite is attributed to high density networks of CNTs and excellent intrinsic properties of CNTs such as the small heat capacity and large surface area to volume ratio[166]. Additionally, under a given input voltage, the electric heating performance could be easily tuned through the design of the number of printed layer, and composites with more CNT layers could reach a higher steady-state temperature because of their lower sheet resistance. Table 6 shows a comparison of heating rate of our fabricated CNT/SMP composites to those of previously reported heater. It clearly shows that our composites have faster heating rate. This high

heating rate coupling with excellent design flexibility indicated that CNT/SMP are very promising for heating applications.

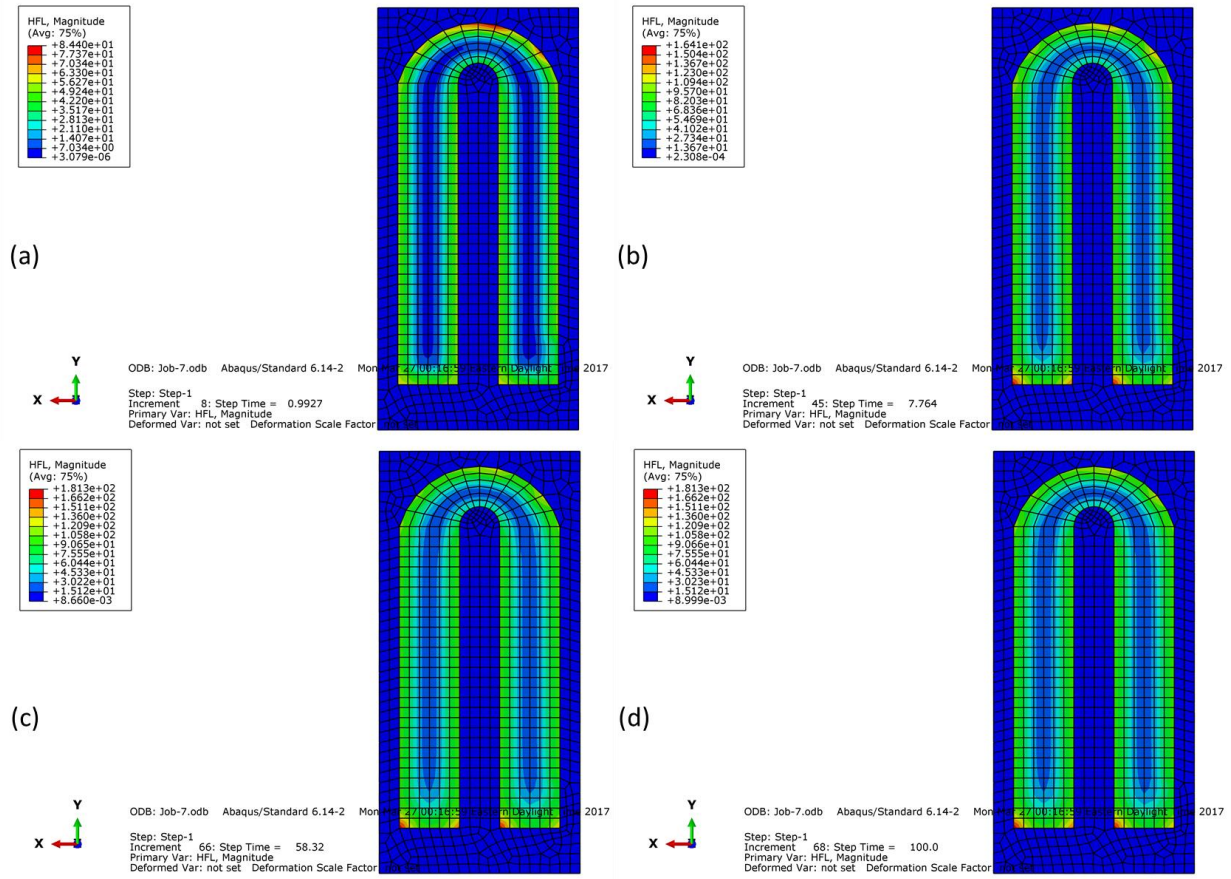

Figure 56. Heat flux magnitude evolution for the composites (a) time = 0.9927 s (b) time = 7.764 s (c) time = 58.32 s (d) time =100s

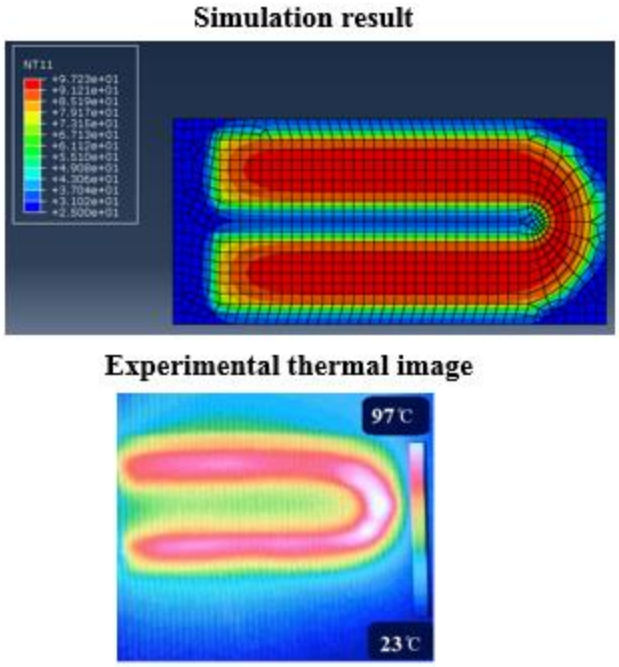

Figure 57. Simulated and experimental thermal image of steady-state temperature on the surface of carbon nanotube based electrical heating element

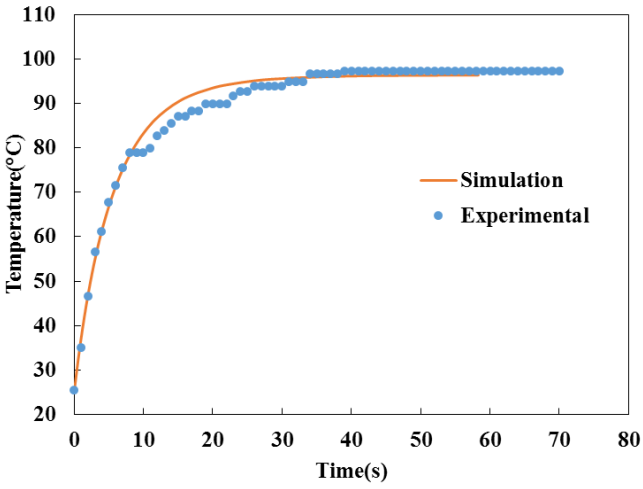

Figure 58. Simulated and experimental temperature data as time increases

Table 6. A comparison of heating rate of CNT/SMP composites

Materials	Fabrication Method	Heating rate under similar 0.2 W/cm^{2}power density	Ref
MWCNT/PDMS	Solution casting	1.67°C/s	[17]
CNT/PE	Molding	0.75°C/s	[90]
MWCNT/Epoxy	Molding	0.62°C/s	[15]
MWCNT/Aramid	Solution Casting	5°C/s	[12]
MWCNT/PE	Solution Casting	1°C/s	[14]
MWCNT/Cellulose	Dip coating	1.875°C/s	[92]
MWCNT/PDMS	Hot press	4.3°C/s	[93]
Our work	Inkjet printing	3.23°C/s	

6.4 Conclusion

This study developed a novel digitally controlled spray deposition modeling technique to incorporate CNT layers into shape memory thermoplastic polyurethane to fabricate CNT/SMP nanocomposites. This technique shows an additive characteristic and has an exquisite print path control that enables the fabrication of the desired number of CNT layers with arbitrary geometries. Due to the flexibility of this fabrication technique, the electrical heating properties of fabricated CNT/SMP composites could be easily tuned by adjusting the geometry and number of printed CNT layers. Main conclusions to be drawn as follows: (1) the fabricated composites showed a low

electrical resistance due to the high density of CNT networks and excellent intrinsic electrical properties of CNTs. With 50 CNT layers, the sheet resistance of composites could be as low as 28.7 Ω/sq. (2) homogeneously heating with various patterns and heating with a thermal gradient were realized in CNT/SMP composites through designing of printed CNT patterns. It was found that CNT/SMP composites showed a fast thermal response to the applied voltage, and a steady-state temperature of ~92ºC was achieved in less than 20s. The steady-state temperatures of the composite could be adjusted by varying the number of printed CNT layers in CNT/SMP composites as well as the input electric power. Great design space and energy efficiency could be achieved by optimizing the number of printed CNT layers in CNT/SMP composites.

CHAPTOR SEVEN: ELECTRICAL ACTUATION OF THE CNT/SHAPE MEMORY POLYMER NANOCOMPOSITES

7.1. Introduction

As a typical smart material, SMP can be deformed into a temporary shape and then recover to its original (or permanent) shape upon exposure to heat stimuli [101-103]. Therefore, besides acting as an electric heater, due to their superior structural versatility, CNT/SMPs can also be used in many other fields, including smart tooling [104], deployable medical device [105] and morphing aircraft [106]. Many efforts have been proposed focusing on the electrical actuation of CNT/SMP composites. Electro-active multi-walled carbon nanotubes filled polyurethane shape memory composites were prepared by Mahapatra et al. [107]. The resultant composites showed more than 98% shape recovery ratio and a rapid recovery time of 9s under a voltage of 40V. Lu et al. [108] investigated the shape memory behaviors of CNT nanopaper/SMP composites. Owing to the excellent electrical conductivity of nanopaper, their composites showed a fully shape recovery at a low voltage of 8.4V. While these CNT/SMP composites showed a high shape recovery ratio when electrical power was applied, some challenges in their fabrications and properties have prevented their widespread industrial applications. To date, all the fabricated CNT/SMP composites showed the same temperature thus same shape recovery ratio at different locations in composites. However, from SMP applications like smart skin or smart tooling perspective, the programmable shape recovery ratio at specified locations are desirable.

This study developed a spray deposition modeling (SDM) technique for fabricating CNT/SMP composites with desirable actuation properties. The investigations were focused on the shape recovery behaviors of obtained CNT/SMP composites.

Honeycomb structures were excellent innovation in composites industry due to the reduced weight, smooth skin and excellent fatigue resistance. The cell configuration is usually hexagons. The honeycomb structure is widely used in aerospace, automotive, building construction and energy absorption applications[167]. Common polymeric honeycomb structure are made of polypropylene, polyurethane and polycarbonate[168]. Some research groups have reported using different fabrication technique to make honeycomb structures, such as thermoforming and extrusion[169]. The use of 3D printing for fabricating honeycomb structure has promised to produce components with complex geometries according to computer designs. 3D printing offers many advantages in the fabrication of honeycomb structures, including high precision, cost effective and customized geometry[170]. As honeycomb structure can be printed in a single process without further processing such as stacking and bonding. Additionally, the cellular structure design could be modified in CAD software to render specific honeycomb structure applications.

A morphing structure can substantially change its shape and size in-flight to improve the performance or enable multiple missions[171]. One of the promising candidate designs for morphing structure is the deployable wing configuration[172]. As one representative of the intelligent shape memory materials, shape memory polymers (SMPs) gained significant interest in recent years[173]. With a specially designed structure, SMPs are able to change their deformed shapes and adapt to the conditions of their surrounding environment[103]. A typical shape memory cycle of the materials is demonstrated in Figure 59. SMP can be fixed into a temporary shape, and then recovers to its original shape by an external stimulus (e.g. heat, electricity). For morphing wings application, it is important to investigate the actuation of honeycomb structured shape memory polymer composites since these lightweight structure will benefit design a lot.

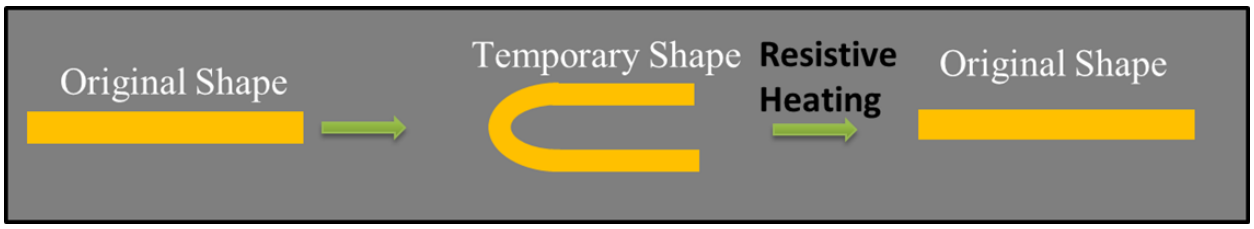

Figure 59. Schematic of the shape-memory effect

7.2. Characterization

Shape memory behavior was investigated according to bending tests, in which the specimens were firstly bent into "U" shapes at 100°C and the "U" shapes should be fixed by cooling the specimens to room temperature. For bending tests, the angle between the two sides of the bent specimen at the time of 0s was measured as θ_0. When the specimens were electrically heated, the specimens started to recover to their permanent shape, and in this process the angle between the two sides of the bent specimen θ_t was measured at variable time. The shape recovery ratio (SR) was calculated using the following equation [174, 175]

7.3. Results and Discussions

The schematics of the specimen and the test device setup are shown in Figure 60. To minimize the gravity effect, the flat surface of the specimen is fixed to be perpendicular to the ground. The physical camera is set on the top of specimens to get a top view of the shape memory recovery process, and the thermal infrared camera is set at the side of specimens to get a side view of this process.

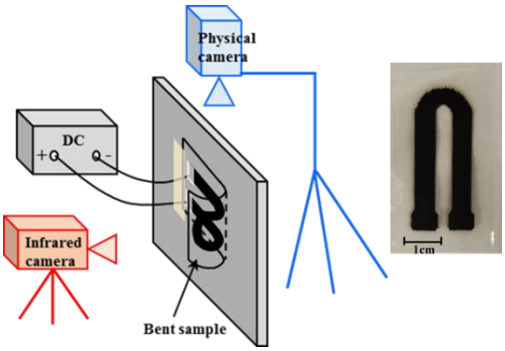

Figure 60. The schematics of the specimen and the test device setup

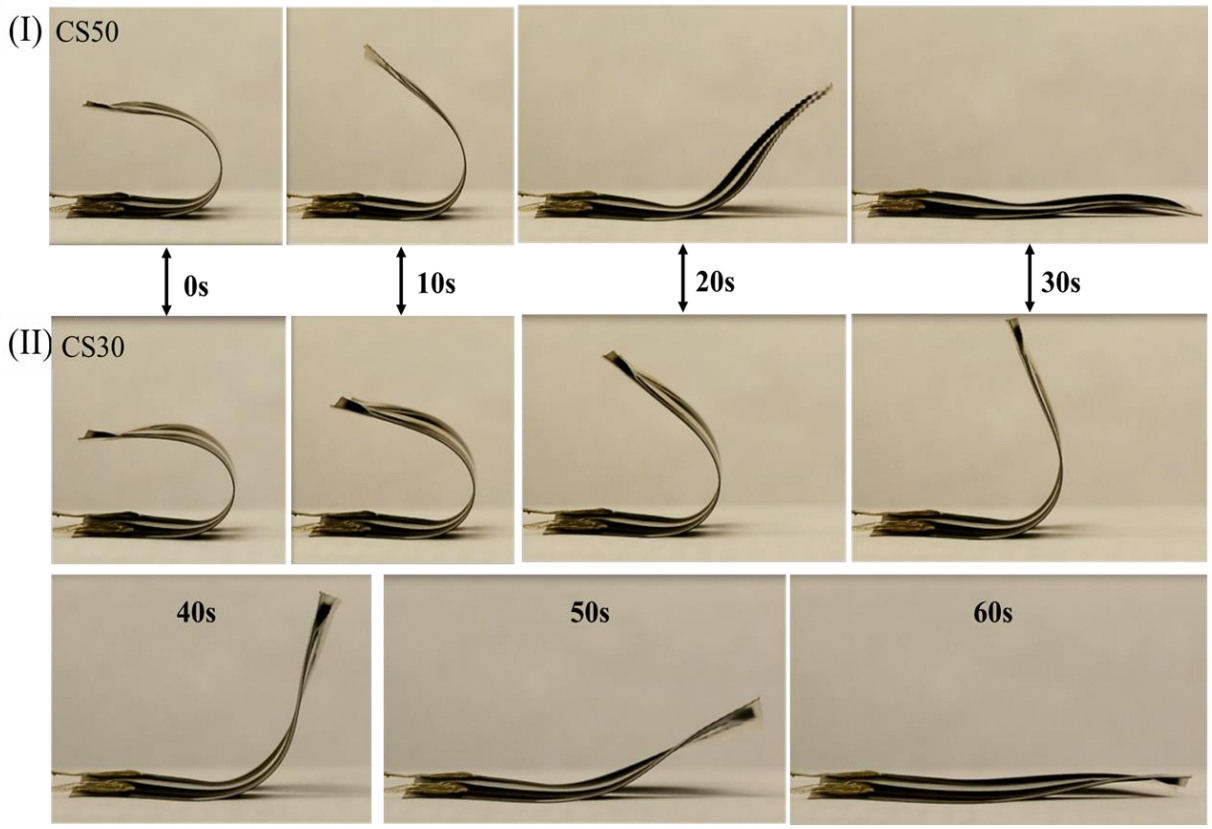

Figure 61. Shape memory process of (I) CS50 and (II) CS30 composites under 40V

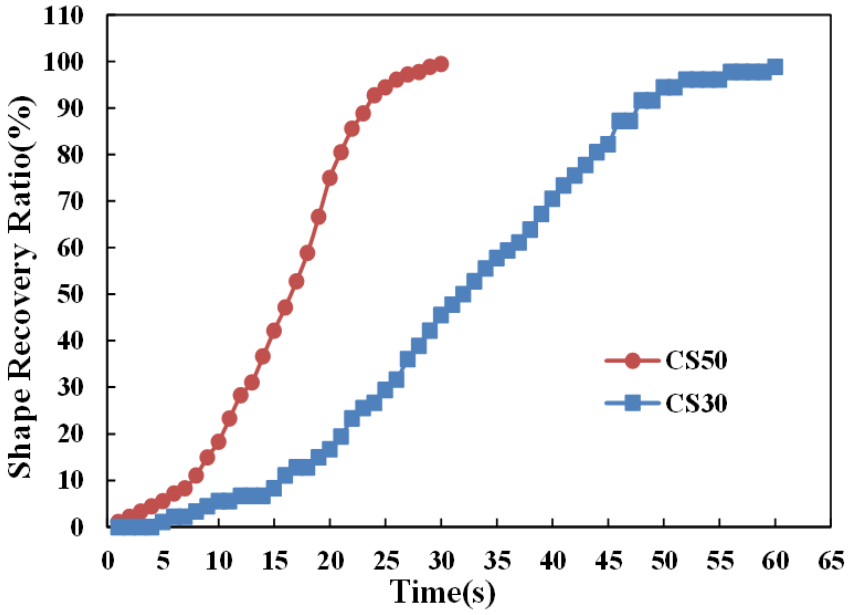

Figure 62. Shape memory ratio over time

Figure 61 shows the screenshots of the shape recovery process of CS30 and CS50 specimens under a constant voltage of 40V. Shape recovery ratios over time are shown in Figure 62. The recovery speed for the two specimens is low within the first 10s, because within this time period, the specimens have not been fully heated. It was obvious in Figure 63 that, at first 10s, the temperature keeps increasing with time. After that, CS50 was heated to 90°C that is about 35°C above its glass transition temperature (T_g).

In our study, the CNT layer is much thinner than the SMP layer so the influence of CNTs on the T_g of composites could be negligible. Since the resistance of CS50 is lower than that of CS30, thus under the same voltage, the surface temperature of CS50 specimen can reach to a higher value. It was revealed that CS50 showed faster recovery speed than CS30, and the whole recovery process for CS50 takes 30s, whereas it takes 60s for CS30. It is because when shape memory polyurethanes were heated above their T_g, their recovery torque provided by molecular movement increases as the temperature increases [176]. CS50 specimens have a higher surface temperature so that they

obtain a higher recovery torque to go back to their original shapes faster. In this experiment, both of specimens showed approximately 100% shape recovery ratio.

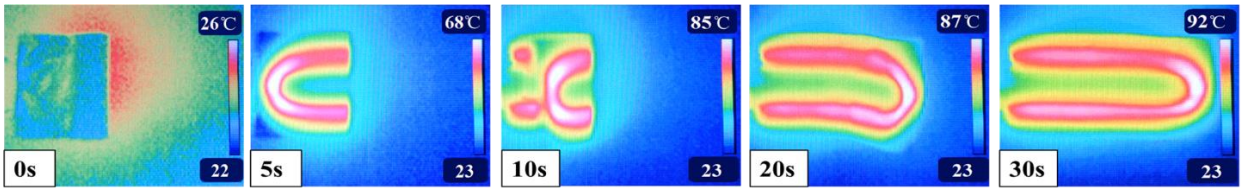

Figure 63. Snapshots of temperature distribution of CS50 composites during shape recovery process

A standard Boltzmann function can be used to analyze the shape recovery data:

$$R(t) = A_2 + \frac{A_1 - A_2}{1 + e^{(t - t_0)/\tau}}$$

By fitting the experimental data, all four constant could be obtained. Figure 64 shows that the theoretical equation fit with the experimental data.

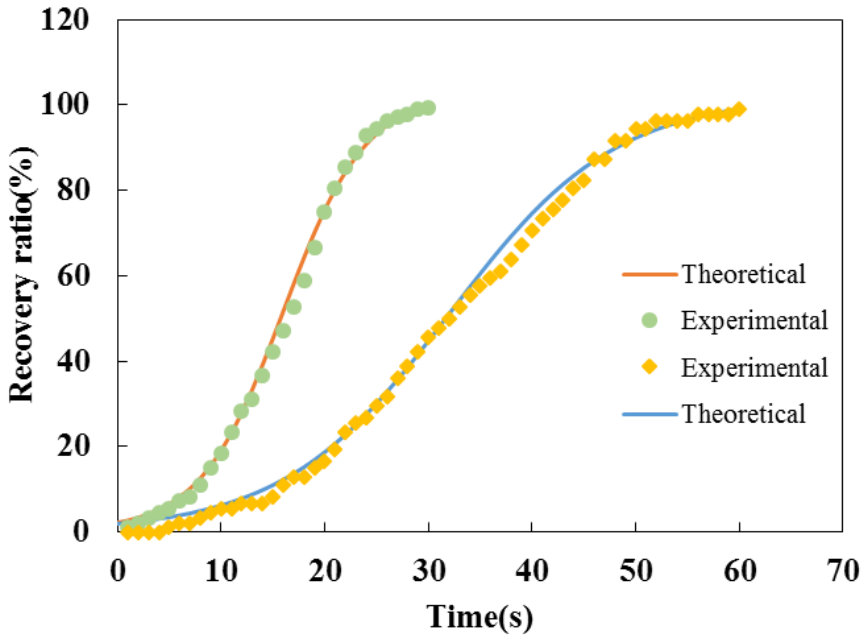

Figure 64. Fitted curve using a Boltzmann function

The 2nd derivatives of the fit curves were then calculated and plotted (Figure 65). All the plots show a similar pattern consisting of two opposite peaks. Two characteristic times were defined as introduction time and recovery time to describe the shape recovery process. The obtained induction and recovery times were plotted for nanocomposites with different number of layers (Figure 65). As we can see, by adjusting the printed number of CNT layers, the initiation and recovery speed of nanocomposites could be controlled.

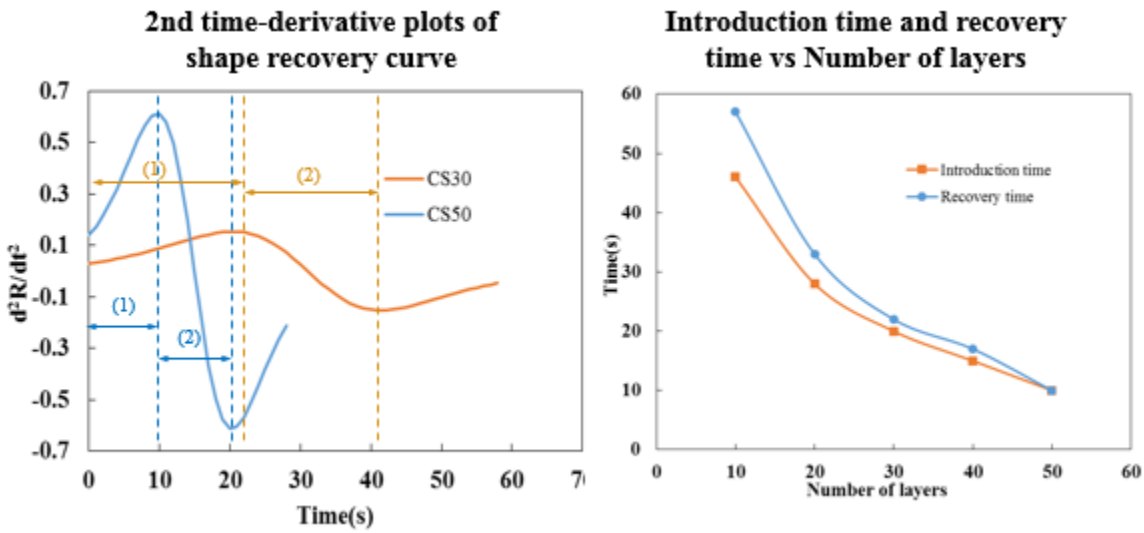

Figure 65. Left: The 2nd derivatives of the fit curves; Right: induction and recovery times of nanocomposites with different number of layers

To investigate the localized actuation of CNT/SMP composites with different shape recovery ratios, the shape recovery process of the "L" shaped CNT/SMP composite (Figure 66) was studied.

The vertical part of the “L” shaped specimen was fabricated with 50 CNT layers, and the horizontal part was fabricated with 30 CNT layers.

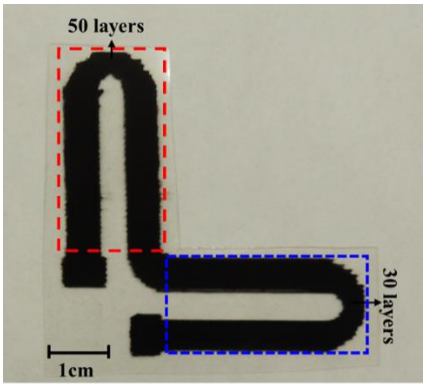

Figure 66. Picture of “L”-shaped CNT/SMP composites

Both the vertical and horizontal parts were bent to “U” shape for the actuation test, which was done under a constant voltage of 60V. Figure 67 shows the screenshots of the shape recovery process of the “L” shaped specimen. In this specimen, the part with 50 CNT layers and the part with 30 CNT layers can be treated as two series resistors. Since the electrical current is same in these two parts, higher heating power can be achieved at part with 30 CNT layers where higher electrical resistance was achieved. Therefore, the surface temperature of part with 30 CNT layers was higher than the part with 50 CNT layers.

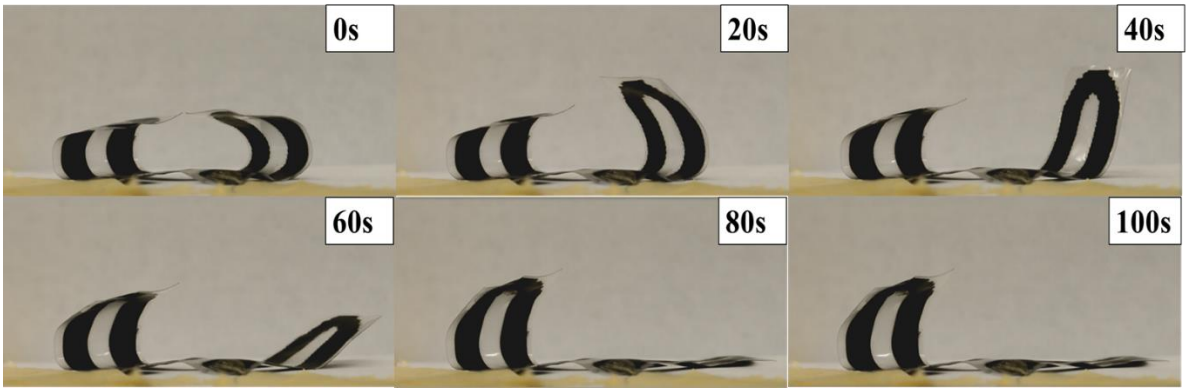

Figure 67. Snapshots of shape recovery process

As Figure 69 shows, part with 30 CNT layers was heated to 75°C that is about 20°C above its T_g, whereas the temperature of CS50 is just above its T_g. Consequently, part with 30 CNT layers was fully recovered to its original shape, but part with 50 CNT could not have enough recovery torque to fully go back to its original shape and showed a recovery ratio of 27%. Thus, it can be seen that through designing number of printed CNT layers at different locations, localized actuation of SMP composites with a desired shape recovery ratio could be performed, which gives great design flexibility for smart skin or tooling applications that needs different deformations at different locations.

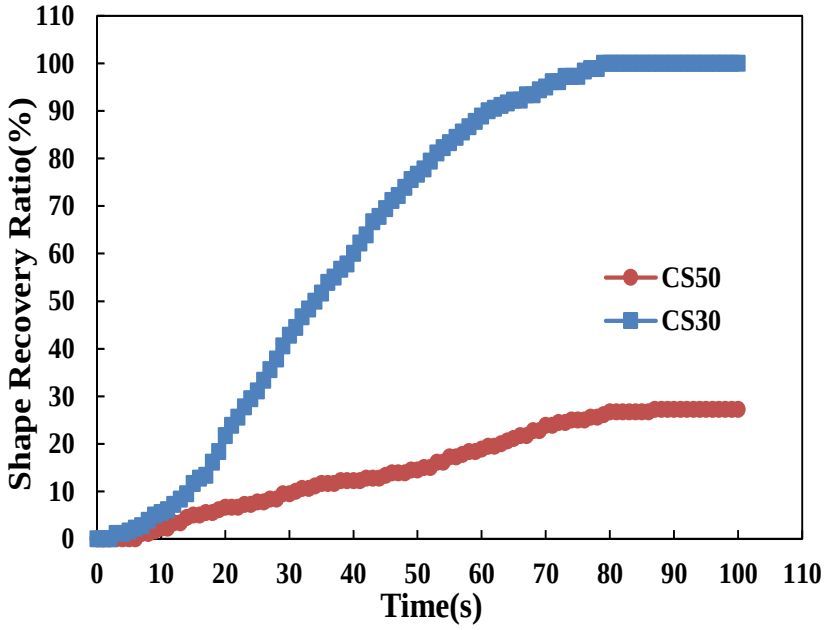

Figure 68. Shape recovery ratio over time

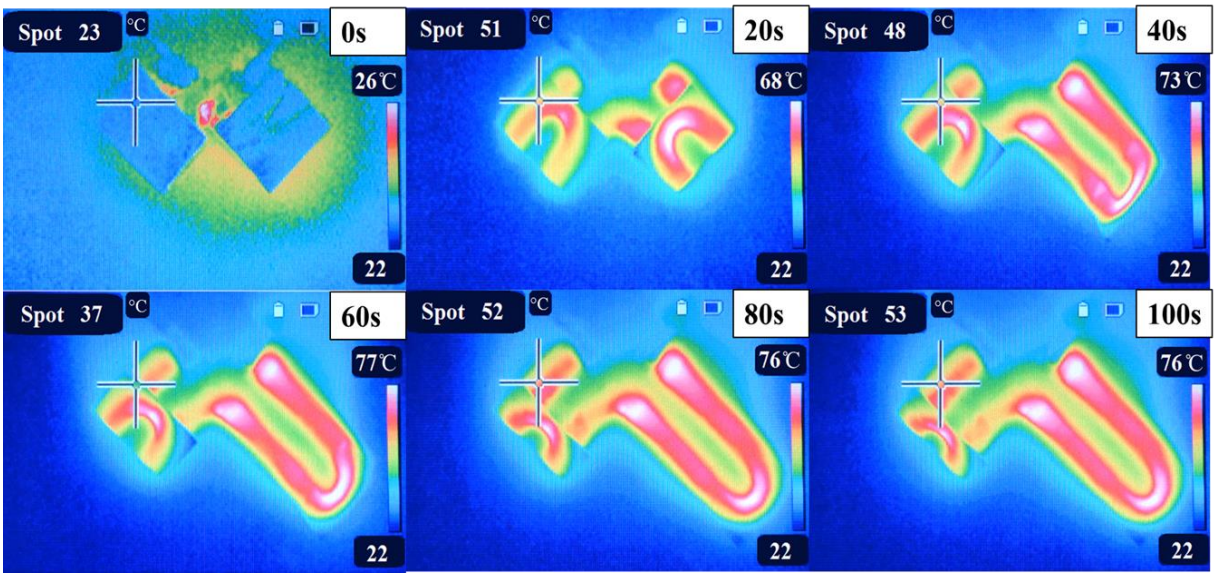

Figure 69. Snapshots of temperature distribution of the composites during shape recovery process

Then, the actuation of CNT/SMP honeycomb structure was investigated. In this study, shape memory polyurethane filament was developed through extrusion process. Single-screw extruder was carefully designed with controlled speed and temperature to produce the polyurethane filament. A commercially available fused deposition modeling 3D printer was used to print the SMP substrate with honeycomb structure. Carbon nanotube inks were then sprayed on the SMP substrate. A basic honeycomb structure design was used in this study. Figure 70 shows the honeycomb structure configuration, with the dimension of 80mm x 30mm x 1mm. and Figure 71 shows the fabricated SMP composites after stretching to 10% strain.

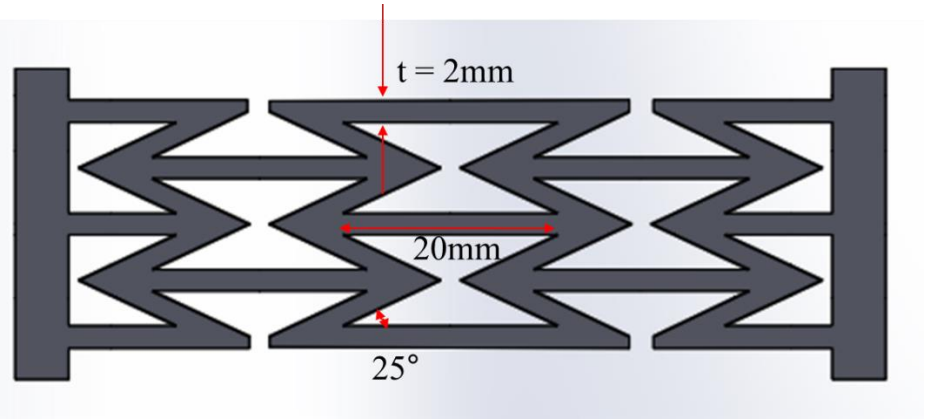

Figure 70. Schematics of honeycomb structure

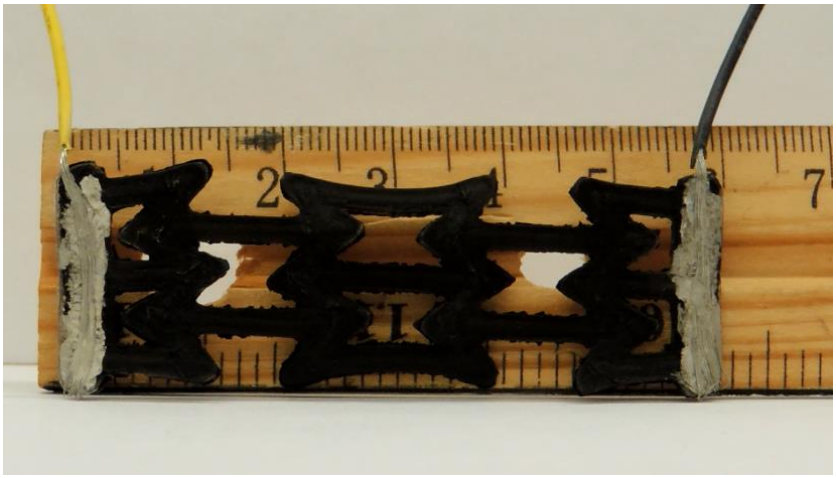

Figure 71. Fabricated SMP composites after stretching to 10% strain.

Figure 72 shows that the SMP nanocomposite was successfully actuated under 50V. The shape recovery ratio reach to 100% in less than 90s, and thermal image also shows the temperature increase to 60°C above its glass transition temperature, which induced the shape recovery process. The successful actuation of the honeycomb structure bring huge possibility for the fabrication of morphing wing with reduced weight.

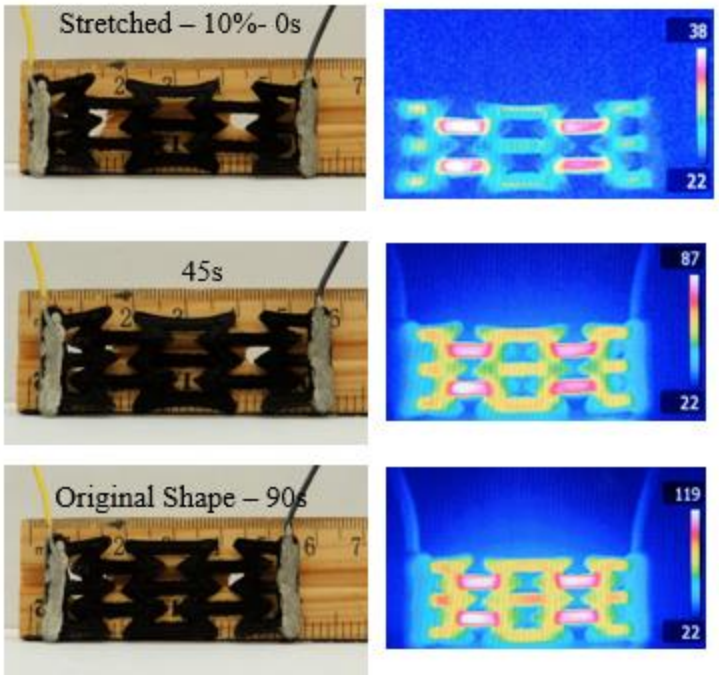

Figure 72. Snapshots of shape recovery process and temperature distribution of fabricated nanocomposite with honeycomb structure

7.4. Conclusion

The shape recovery effect of CNT/SMP composites can be triggered by their resistive heating without an external heater and the composite can reach a full shape recovery within 30s. Particularly, by incorporating different numbers of printed CNT layers into SMP at specified locations, localized actuation of SMP with the desired shape recovery ratio could be achieved. Especially, electrical actuation of honeycomb structure SMP composites was successfully realized. The fabricated composites with honeycomb structure could be potentially used for lightweight morphing wings. In combination of the excellent electrical properties of CNTs and shape memory effect of SMPs, the developed CNT/SMP composite could be a promising candidate for various heating and actuation applications.

CHAPTOR EIGHT: CONCLUSION AND FUTURE WORK

8.1. Conclusion

This paper presented a simple and accurate route to fabricate arbitrarily shaped carbon nanotube patterns onto polyurethane substrate based on a single-step spray deposition modeling(SDM) technique. The presented method greatly simplifies the fabrication process and improves its efficiency and flexibility.

As a prototype of application, CNT based strain sensors was manufactured and tested showing consistent resistance change under tensile strains. Up to a maximum strain amplitude of 40%, the strain-dependent resistance showed good linearity. Strain sensing behavior under cyclic loading of CNT based strain sensors was studied. The relations between resistance change and strain of carbon nanotubes indicated that the carbon nanotube strain sensors had high sensitivity at high strain level, with gauge factor 11, which is higher than that of usually used metal foil strain sensor. At low strain level(1%), CNT based strain sensors showed good recoverability after cyclic loading. SDM approach is able to control the sensing properties of the printed strain sensor by simply changing layers of printings. The technique is highly applicable for scaling up with high productivity. Due to the flexibility of this SDM fabrication method, strain sensors with different sizes and complicated geometries could also be obtained.

Self-heating performance of CNT based films was also investigated. The electrical resistivity and self-temperature-control heating properties of printed CNT films were strongly dependent upon numbers of printed CNT layers. The resistivity showed an exponential decrease as the number of layers increased. With 50 layers printing of CNTs, the sheet resistivity of carbon nanotubes could be as low as $105\,\Omega / sq$. When 30V voltage was applied to the CNT based films, the surface

temperature of film reached the maximum 107°C and became stable at time shorter than 60 s. The maximum temperature of the films could be controlled by adjusting the number of printed CNT layers. The quick heating and wide adjustability of temperature suggested its good application to high efficient heat pattern. The shape recovery effect of CNT/SMP composites can be triggered by their resistive heating without an external heater and the composite can reach a full shape recovery within 30s. Particularly, by incorporating different numbers of printed CNT layers into SMP at specified locations, localized actuation of SMP with desired shape recovery ratio could be achieved. Furthermore, honeycomb structured CNT/SMP composites were also successfully actuated through electrical stimulus and a fully recovery of their original shape was observed in less than 90s.

8.2. Future Plan

Attaching strain sensors onto curved surface is very difficult. Our SDM machine is very promising to print carbon nanotube on a curved surface. Our SDM machine now has a fixed platform, but a rotating axis will be adding onto platform so that the substrate could rotate while printing.

The conductive films for self-heating requires a low electrical resistivity to provide a suitable current at a relative low voltage. To decrease the resistivity of printed CNT layers, carbon nanotube ink need to be improved. Chemical modification such as acid functionalized is efficient to improve the dispersion of carbon nanotube in the inks thus decrease the resistivity. Solvent like ethanol and acetone with higher evaporation rate will be used to make CNT network denser. Since faster evaporation of solvent reduced the flow effect of CNT suspension, and CNT will combine tightly with each other. Adding other nanoparticle was reported to reduce the joint resistance of CNTs. Ink with variable materials will also be investigated in the future.

REFERENCES

1. M. Ouyang, J.-L. Huang, and C.M. Lieber, *Fundamental electronic properties and applications of single-walled carbon nanotubes.* Accounts of Chemical Research, 2002. **35**(12): p. 1018-1025.
2. E.W. Wong, P.E. Sheehan, and C.M. Lieber, *Nanobeam mechanics: elasticity, strength, and toughness of nanorods and nanotubes.* Science, 1997. **277**(5334): p. 1971-1975.
3. E. Pop, D. Mann, Q. Wang, K. Goodson, and H. Dai, *Thermal conductance of an individual single-wall carbon nanotube above room temperature.* Nano letters, 2006. **6**(1): p. 96-100.
4. R. Setton, P. Bernier, and S. Lefrant, *Carbon molecules and materials*. 2002: CRC Press.
5. S.K. Malhotra, K. Goda, and M.S. Sreekala, *Part One Introduction to Polymer Composites.* 2012.
6. L. Cai, L. Song, P. Luan, Q. Zhang, N. Zhang, Q. Gao, D. Zhao, X. Zhang, M. Tu, and F. Yang, *Super-stretchable, transparent carbon nanotube-based capacitive strain sensors for human motion detection.* Scientific reports, 2013. **3**.
7. H. Liu, Y. Li, K. Dai, G. Zheng, C. Liu, C. Shen, X. Yan, J. Guo, and Z. Guo, *Electrically conductive thermoplastic elastomer nanocomposites at ultralow graphene loading levels for strain sensor applications.* Journal of Materials Chemistry C, 2016. **4**(1): p. 157-166.
8. J. Zhu, S. Wei, J. Ryu, and Z. Guo, *Strain-sensing elastomer/carbon nanofiber "metacomposites".* The Journal of Physical Chemistry C, 2011. **115**(27): p. 13215-13222.
9. Q. He, T. Yuan, X. Zhang, S. Guo, J. Liu, J. Liu, X. Liu, L. Sun, S. Wei, and Z. Guo, *Heavy duty piezoresistivity induced strain sensing natural rubber/carbon black nanocomposites*

reinforced with different carbon nanofillers. Materials Research Express, 2014. **1**(3): p. 035029.

10. R. Zhang, H. Deng, R. Valenca, J. Jin, Q. Fu, E. Bilotti, and T. Peijs, *Carbon nanotube polymer coatings for textile yarns with good strain sensing capability.* Sensors and Actuators A: Physical, 2012. **179**: p. 83-91.
11. I. Kang, M.J. Schulz, J.H. Kim, V. Shanov, and D. Shi, *A carbon nanotube strain sensor for structural health monitoring.* Smart materials and structures, 2006. **15**(3): p. 737.
12. Y.G. Jeong and G.W. Jeon, *Microstructure and performance of multiwalled carbon nanotube/m-aramid composite films as electric heating elements.* ACS applied materials & interfaces, 2013. **5**(14): p. 6527-6534.
13. K. Chu, D. Kim, Y. Sohn, S. Lee, C. Moon, and S. Park, *Electrical and thermal properties of carbon-nanotube composite for flexible electric heating-unit applications.* IEEE Electron Device Letters, 2013. **34**(5): p. 668-670.
14. S. Isaji, Y. Bin, and M. Matsuo, *Electrical conductivity and self-temperature-control heating properties of carbon nanotubes filled polyethylene films.* Polymer, 2009. **50**(4): p. 1046-1053.
15. H. Chu, Z. Zhang, Y. Liu, and J. Leng, *Self-heating fiber reinforced polymer composite using meso/macropore carbon nanotube paper and its application in deicing.* Carbon, 2014. **66**: p. 154-163.
16. J. Yan and Y.G. Jeong, *Highly elastic and transparent multiwalled carbon nanotube/polydimethylsiloxane bilayer films as electric heating materials.* Materials & Design, 2015. **86**: p. 72-79.

17. J. Yan and Y.G. Jeong, *Synergistic effect of hybrid carbon fillers on electric heating behavior of flexible polydimethylsiloxane-based composite films.* Composites Science and Technology, 2015. **106**: p. 134-140.

18. S.H. Huang, P. Liu, A. Mokasdar, and L. Hou, *Additive manufacturing and its societal impact: a literature review.* The International Journal of Advanced Manufacturing Technology, 2013. **67**(5-8): p. 1191-1203.

19. A. Standard, *F2792, Standard Terminology for Additive Manufacturing Technologies*. 2012, ASTM International, West Conshohocken, Pa, USA.

20. C.W. Hull, *Apparatus for production of three-dimensional objects by stereolithography*. 1986, Google Patents.

21. G.N. Levy, R. Schindel, and J.-P. Kruth, *Rapid manufacturing and rapid tooling with layer manufacturing (LM) technologies, state of the art and future perspectives.* CIRP Annals-Manufacturing Technology, 2003. **52**(2): p. 589-609.

22. E. Kroll and D. Artzi, *Enhancing aerospace engineering students' learning with 3D printing wind-tunnel models.* Rapid Prototyping Journal, 2011. **17**(5): p. 393-402.

23. K.V. Wong and A. Hernandez, *A review of additive manufacturing.* ISRN Mechanical Engineering, 2012. **2012**.

24. D.B. Short, *Use of 3D Printing by Museums: Educational Exhibits, Artifact Education, and Artifact Restoration.* 3D Printing and Additive Manufacturing, 2015. **2**(4): p. 209-215.

25. S.V. Murphy and A. Atala, *3D bioprinting of tissues and organs.* Nature biotechnology, 2014. **32**(8): p. 773-785.

26. F. Rengier, A. Mehndiratta, H. von Tengg-Kobligk, C.M. Zechmann, R. Unterhinninghofen, H.-U. Kauczor, and F.L. Giesel, *3D printing based on imaging data:*

review of medical applications. International journal of computer assisted radiology and surgery, 2010. **5**(4): p. 335-341.

27. A.K. Sood, R. Ohdar, and S. Mahapatra, *Parametric appraisal of mechanical property of fused deposition modelling processed parts.* Materials & Design, 2010. **31**(1): p. 287-295.
28. E.M. Sachs, J.S. Haggerty, M.J. Cima, and P.A. Williams, *Three-dimensional printing techniques*. 1993, Google Patents.
29. B. Utela, D. Storti, R. Anderson, and M. Ganter, *A review of process development steps for new material systems in three dimensional printing (3DP).* Journal of Manufacturing Processes, 2008. **10**(2): p. 96-104.
30. F.P. Melchels, J. Feijen, and D.W. Grijpma, *A review on stereolithography and its applications in biomedical engineering.* Biomaterials, 2010. **31**(24): p. 6121-6130.
31. Y. Cho, I. Lee, and D.-W. Cho, *Laser scanning path generation considering photopolymer solidification in micro-stereolithography.* Microsystem technologies, 2005. **11**(2-3): p. 158-167.
32. C. Heller, M. Schwentenwein, G. Russmueller, F. Varga, J. Stampfl, and R. Liska, *Vinyl esters: low cytotoxicity monomers for the fabrication of biocompatible 3D scaffolds by lithography based additive manufacturing.* Journal of Polymer Science Part A: Polymer Chemistry, 2009. **47**(24): p. 6941-6954.
33. D. Gu, W. Meiners, K. Wissenbach, and R. Poprawe, *Laser additive manufacturing of metallic components: materials, processes and mechanisms.* International materials reviews, 2012. **57**(3): p. 133-164.
34. I. Gibson and D. Shi, *Material properties and fabrication parameters in selective laser sintering process.* Rapid Prototyping Journal, 1997. **3**(4): p. 129-136.

35. R. Goodridge, M. Shofner, R. Hague, M. McClelland, M. Schlea, R. Johnson, and C. Tuck, *Processing of a Polyamide-12/carbon nanofibre composite by laser sintering.* Polymer Testing, 2011. **30**(1): p. 94-100.

36. T. Billiet, M. Vandenhaute, J. Schelfhout, S. Van Vlierberghe, and P. Dubruel, *A review of trends and limitations in hydrogel-rapid prototyping for tissue engineering.* Biomaterials, 2012. **33**(26): p. 6020-6041.

37. Xin Wang, Qian Yang, Zuowan Zhou, and Jihua Gou, *Processing and characterization of helical carbon nanotube paper based thermoplastic nanocomposite films*, in *CAMX*. 2014: Orlando, FL.

38. X. Yan, J. Gu, G. Zheng, J. Guo, A.M. Galaska, J. Yu, M.A. Khan, L. Sun, D.P. Young, and Q. Zhang, *Lowly loaded carbon nanotubes induced high electrical conductivity and giant magnetoresistance in ethylene/1-octene copolymers.* Polymer, 2016. **103**: p. 315-327.

39. Y.-S. Tang, J. Kong, J.-W. Gu, and G.-Z. Liang, *Reinforced cyanate ester resins with carbon nanotubes: surface modification, reaction activity and mechanical properties analyses.* Polymer-Plastics Technology and Engineering, 2009. **48**(4): p. 359-366.

40. H. Chen, M.B. Müller, K.J. Gilmore, G.G. Wallace, and D. Li, *Mechanically strong, electrically conductive, and biocompatible graphene paper.* Adv. Mater, 2008. **20**(18): p. 3557-3561.

41. J. Gu, C. Xie, H. Li, J. Dang, W. Geng, and Q. Zhang, *Thermal percolation behavior of graphene nanoplatelets/polyphenylene sulfide thermal conductivity composites.* Polymer Composites, 2014. **35**(6): p. 1087-1092.

42. J. Gu, N. Li, L. Tian, Z. Lv, and Q. Zhang, *High thermal conductivity graphite nanoplatelet/UHMWPE nanocomposites.* RSC Advances, 2015. **5**(46): p. 36334-36339.

43. Fei Liang, Xin Wang, Yunjun Xu, Bob Mabbott, and Jihua Gou, *Polyurethane nanocomposites coatings with enhanced mechanical and thermal properties*, in *CAMX*. 2014: Orlando,FL.

44. J. Gu, C. Liang, J. Dang, W. Dong, and Q. Zhang, *Ideal dielectric thermally conductive bismaleimide nanocomposites filled with polyhedral oligomeric silsesquioxane functionalized nanosized boron nitride.* RSC Advances, 2016. **6**(42): p. 35809-35814.

45. H. Lu, X. Wang, Y. Yao, J. Gou, D. Hui, B. Xu, and Y. Fu, *Synergistic Effect of Siloxane Modified Aluminum Nanopowders and Carbon Fiber on Electrothermal Efficiency of Polymeric Shape Memory Nanocomposite.* Composites Part B: Engineering, 2015.

46. H. Zhan, F. Cheng, Y. Chen, K.W. Wong, J. Mei, D. Hui, W.M. Lau, and Y. Liu, *Transfer printing for preparing nanostructured PDMS film as flexible SERS active substrate.* Composites Part B: Engineering, 2016. **84**: p. 222-227.

47. A.R.T. Perez, D.A. Roberson, and R.B. Wicker, *Fracture surface analysis of 3D-printed tensile specimens of novel ABS-based materials.* Journal of Failure Analysis and Prevention, 2014. **14**(3): p. 343-353.

48. M. Shofner, K. Lozano, F. Rodríguez-Macías, and E. Barrera, *Nanofiber-reinforced polymers prepared by fused deposition modeling.* Journal of applied polymer science, 2003. **89**(11): p. 3081-3090.

49. J. Hector Sandoval and R.B. Wicker, *Functionalizing stereolithography resins: effects of dispersed multi-walled carbon nanotubes on physical properties.* Rapid Prototyping Journal, 2006. **12**(5): p. 292-303.

50. D. Lin, S. Jin, F. Zhang, C. Wang, Y. Wang, C. Zhou, and G.J. Cheng, *3D stereolithography printing of graphene oxide reinforced complex architectures.* Nanotechnology, 2015. **26**(43): p. 434003.

51. S.-z. Guo, X. Yang, M.-C. Heuzey, and D. Therriault, *3D printing of a multifunctional nanocomposite helical liquid sensor.* Nanoscale, 2015. **7**(15): p. 6451-6456.

52. Y. Zhang, H. Li, X. Yang, T. Zhang, K. Zhu, W. Si, Z. Liu, and H. Sun, *Additive manufacturing of carbon nanotube-photopolymer composite radar absorbing materials.* Polymer Composites, 2016.

53. Z. Rymansaib, P. Iravani, E. Emslie, M. Medvidović-Kosanović, M. Sak-Bosnar, R. Verdejo, and F. Marken, *All-Polystyrene 3D-Printed Electrochemical Device with Embedded Carbon Nanofiber-Graphite-Polystyrene Composite Conductor.* Electroanalysis, 2016.

54. S.R. Athreya, K. Kalaitzidou, and S. Das, *Processing and characterization of a carbon black-filled electrically conductive Nylon-12 nanocomposite produced by selective laser sintering.* Materials Science and Engineering: A, 2010. **527**(10): p. 2637-2642.

55. F. Ning, W. Cong, J. Qiu, J. Wei, and S. Wang, *Additive manufacturing of carbon fiber reinforced thermoplastic composites using fused deposition modeling.* Composites Part B: Engineering, 2015. **80**: p. 369-378.

56. D. Yugang, Z. Yuan, T. Yiping, and L. Dichen, *Nano-TiO2-modified photosensitive resin for RP.* Rapid Prototyping Journal, 2011. **17**(4): p. 247-252.

57. Z. Weng, J. Wang, T. Senthil, and L. Wu, *Mechanical and thermal properties of ABS/montmorillonite nanocomposites for fused deposition modeling 3D printing.* Materials & Design, 2016. **102**: p. 276-283.

58. M. He, Y. Zhao, B. Wang, Q. Xi, J. Zhou, and Z. Liang, *3D Printing Fabrication of Amorphous Thermoelectric Materials with Ultralow Thermal Conductivity.* Small, 2015. **11**(44): p. 5889-5894.

59. U. Vohrer, I. Kolaric, M. Haque, S. Roth, and U. Detlaff-Weglikowska, *Carbon nanotube sheets for the use as artificial muscles.* Carbon, 2004. **42**(5): p. 1159-1164.

60. R.L. Whitby, T. Fukuda, T. Maekawa, S.L. James, and S.V. Mikhalovsky, *Geometric control and tuneable pore size distribution of buckypaper and buckydiscs.* Carbon, 2008. **46**(6): p. 949-956.

61. D. Wang, P. Song, C. Liu, W. Wu, and S. Fan, *Highly oriented carbon nanotube papers made of aligned carbon nanotubes.* Nanotechnology, 2008. **19**(7): p. 075609.

62. Y. Kim, N. Minami, W. Zhu, S. Kazaoui, R. Azumi, and M. Matsumoto, *Langmuir–Blodgett films of single-wall carbon nanotubes: layer-by-layer deposition and in-plane orientation of tubes.* Japanese journal of applied physics, 2003. **42**(12R): p. 7629.

63. Q. Wang and H. Moriyama, *Carbon Nanotube-Based Thin Films: Synthesis and Properties*. 2011: INTECH Open Access Publisher.

64. S. Kim, X. Wang, J.H. Yim, W.C. Tsoi, J.-s. Kim, and S. Lee, *Efficient organic solar cells based on spray-patterned single wall carbon nanotube electrodes.* Journal of Photonics for Energy, 2012. **2**(1): p. 021010-1-021010-9.

65. F.N. Ishikawa, H.-k. Chang, K. Ryu, P.-c. Chen, A. Badmaev, L. Gomez De Arco, G. Shen, and C. Zhou, *Transparent electronics based on transfer printed aligned carbon nanotubes on rigid and flexible substrates.* ACS nano, 2008. **3**(1): p. 73-79.

66. N. Gershenfeld, *How to make almost anything.* Foreign Affairs, 2012. **91**(6): p. 43-57.

67. X. Cao, H. Chen, X. Gu, B. Liu, W. Wang, Y. Cao, F. Wu, and C. Zhou, *Screen printing as a scalable and low-cost approach for rigid and flexible thin-film transistors using separated carbon nanotubes.* ACS nano, 2014. **8**(12): p. 12769-12776.

68. H. Okimoto, T. Takenobu, K. Yanagi, Y. Miyata, H. Shimotani, H. Kataura, and Y. Iwasa, *Tunable Carbon Nanotube Thin-Film Transistors Produced Exclusively via Inkjet Printing.* Advanced materials, 2010. **22**(36): p. 3981-3986.

69. R.P. Tortorich and J.-W. Choi, *Inkjet printing of carbon nanotubes.* Nanomaterials, 2013. **3**(3): p. 453-468.

70. Z. Li, P. Dharap, S. Nagarajaiah, E.V. Barrera, and J. Kim, *Carbon nanotube film sensors.* Advanced materials, 2004. **16**(7): p. 640-643.

71. Z. Zhang, H. Wei, Y. Liu, and J. Leng, *Self-sensing properties of smart composite based on embedded buckypaper layer*. Structural Health Monitoring, 2015: p. 1475921714568405.

72. M. Amjadi, Y.J. Yoon, and I. Park, *Ultra-stretchable and skin-mountable strain sensors using carbon nanotubes–Ecoflex nanocomposites.* Nanotechnology, 2015. **26**(37): p. 375501.

73. X. Cao, X. Wei, G. Li, C. Hu, K. Dai, J. Guo, G. Zheng, C. Liu, C. Shen, and Z. Guo, *Strain sensing behaviors of epoxy nanocomposites with carbon nanotubes under cyclic deformation.* Polymer, 2017. **112**: p. 1-9.

74. X. Li, C. Levy, and L. Elaadil, *Multiwalled carbon nanotube film for strain sensing.* Nanotechnology, 2008. **19**(4): p. 045501.

75. Y. Li, W. Wang, K. Liao, C. Hu, Z. Huang, and Q. Feng, *Piezoresistive effect in carbon nanotube films.* Chinese Science Bulletin, 2003. **48**(2): p. 125-127.

76. D. Lee, H.P. Hong, M.J. Lee, C.W. Park, and N.K. Min, *A prototype high sensitivity load cell using single walled carbon nanotube strain gauges.* Sensors and Actuators A: Physical, 2012. **180**: p. 120-126.

77. R. Rahimi, M. Ochoa, W. Yu, and B. Ziaie, *Highly Stretchable and Sensitive Unidirectional Strain Sensor via Laser Carbonization.* ACS applied materials & interfaces, 2015. **7**(8): p. 4463-4470.

78. C. Lee, L. Jug, and E. Meng, *High strain biocompatible polydimethylsiloxane-based conductive graphene and multiwalled carbon nanotube nanocomposite strain sensors.* Applied Physics Letters, 2013. **102**(18): p. 183511.

79. J.-H. Kong, N.-S. Jang, S.-H. Kim, and J.-M. Kim, *Simple and rapid micropatterning of conductive carbon composites and its application to elastic strain sensors.* Carbon, 2014. **77**: p. 199-207.

80. T. Yamada, Y. Hayamizu, Y. Yamamoto, Y. Yomogida, A. Izadi-Najafabadi, D.N. Futaba, and K. Hata, *A stretchable carbon nanotube strain sensor for human-motion detection.* Nature nanotechnology, 2011. **6**(5): p. 296-301.

81. J. Zhou, H. Yu, X. Xu, F. Han, and G. Lubineau, *Ultrasensitive, Stretchable Strain Sensors Based on Fragmented Carbon Nanotube Papers.* ACS Applied Materials & Interfaces, 2017. **9**(5): p. 4835-4842.

82. F. Michelis, L. Bodelot, Y. Bonnassieux, and B. Lebental, *Highly reproducible, hysteresis-free, flexible strain sensors by inkjet printing of carbon nanotubes.* Carbon, 2015. **95**: p. 1020-1026.

83. Y. Song, J.-I. Lee, S. Pyo, Y. Eun, J. Choi, and J. Kim, *A highly sensitive flexible strain sensor based on the contact resistance change of carbon nanotube bundles.* Nanotechnology, 2016. **27**(20): p. 205502.

84. P. Costa, C. Silvia, J. Viana, and S.L. Mendez, *Extruded thermoplastic elastomers styrene–butadiene–styrene/carbon nanotubes composites for strain sensor applications.* Composites Part B: Engineering, 2014. **57**: p. 242-249.

85. R. Zhang, H. Deng, R. Valenca, J. Jin, Q. Fu, E. Bilotti, and T. Peijs, *Strain sensing behaviour of elastomeric composite films containing carbon nanotubes under cyclic loading.* Composites Science and Technology, 2013. **74**: p. 1-5.

86. H. Liu, J. Gao, W. Huang, K. Dai, G. Zheng, C. Liu, C. Shen, J. Guo, X. Yan, and Z. Guo, *Electrically Conductive Strain Sensing Polyurethane Nanocomposites with Synergistic Carbon Nanotubes and Graphene Bifillers.* Nanoscale, 2016.

87. R. Socher, B. Krause, S. Hermasch, R. Wursche, and P. Pötschke, *Electrical and thermal properties of polyamide 12 composites with hybrid fillers systems of multiwalled carbon nanotubes and carbon black.* Composites Science and Technology, 2011. **71**(8): p. 1053-1059.

88. K. Chu, D. Kim, Y. Sohn, S. Lee, C. Moon, and S. Park, *Electrical and thermal properties of carbon-nanotube composite for flexible electric heating-unit applications.* Electron Device Letters, IEEE, 2013. **34**(5): p. 668-670.

89. J.-E. An and Y.G. Jeong, *Structure and electric heating performance of graphene/epoxy composite films.* European Polymer Journal, 2013. **49**(6): p. 1322-1330.

90. P. Tang, R. Zhang, R. Shi, and Y. Bin, *Synergetic effects of carbon nanotubes and carbon fibers on electrical and self-heating properties of high-density polyethylene composites.* Journal of Materials Science, 2015. **50**(4): p. 1565-1574.

91. H.K. Park, S.M. Kim, J.S. Lee, J.-H. Park, Y.-K. Hong, C.H. Hong, and K.K. Kim, *Flexible plane heater: Graphite and carbon nanotube hybrid nanocomposite.* Synthetic Metals, 2015. **203**: p. 127-134.

92. T.-W. Lee, S.-E. Lee, and Y.G. Jeong, *Carbon nanotube/cellulose papers with high performance in electric heating and electromagnetic interference shielding.* Composites Science and Technology, 2016. **131**: p. 77-87.

93. K. Chu and S.-H. Park, *Electrical heating behavior of flexible carbon nanotube composites with different aspect ratios.* Journal of Industrial and Engineering Chemistry, 2016. **35**: p. 195-198.

94. X. Liu, H. Li, Q. Zeng, Y. Zhang, H. Kang, H. Duan, Y. Guo, and H. Liu, *Electro-active shape memory composites enhanced by flexible carbon nanotube/graphene aerogels.* Journal of Materials Chemistry A, 2015. **3**(21): p. 11641-11649.

95. H. Lu, J. Yin, B. Xu, J. Gou, D. Hui, and Y. Fu, *Synergistic effects of carboxylic acid-functionalized carbon nanotube and nafion/silica nanofiber on electrical actuation efficiency of shape memory polymer nanocomposite.* Composites Part B: Engineering, 2016. **100**: p. 146-151.

96. H. Lu, Y. Yao, J. Yin, and L. Lin, *Functionally graded carbon nanotube and nafion/silica nanofibre for electrical actuation of carbon fibre reinforced shape memory polymer.* Pigment & Resin Technology, 2016. **45**(2): p. 93-98.

97. F.-P. Du, E.-Z. Ye, W. Yang, T.-H. Shen, C.-Y. Tang, X.-L. Xie, X.-P. Zhou, and W.-C. Law, *Electroactive shape memory polymer based on optimized multi-walled carbon nanotubes/polyvinyl alcohol nanocomposites.* Composites Part B: Engineering, 2015. **68**: p. 170-175.

98. J. Chen, Z.-x. Zhang, W.-b. Huang, J.-h. Yang, Y. Wang, Z.-w. Zhou, and J.-h. Zhang, *Carbon nanotube network structure induced strain sensitivity and shape memory behavior changes of thermoplastic polyurethane.* Materials & Design, 2015. **69**: p. 105-113.

99. N. Ahmed, A. Kausar, and B. Muhammad, *Shape memory properties of electrically conductive multi-walled carbon nanotube-filled polyurethane/modified polystyrene blends.* Journal of Plastic Film & Sheeting, 2016. **32**(3): p. 272-292.

100. M.-J. He, W.-X. Xiao, H. Xie, C.-J. Fan, L. Du, X.-Y. Deng, K.-K. Yang, and Y.-Z. Wang, *Facile fabrication of ternary nanocomposites with selective dispersion of multi-walled carbon nanotubes to access multi-stimuli-responsive shape-memory effects.* Materials Chemistry Frontiers, 2017.

101. H. Meng and G. Li, *A review of stimuli-responsive shape memory polymer composites.* Polymer, 2013. **54**(9): p. 2199-2221.

102. S. Shabahang, G. Tao, J.J. Kaufman, Y. Qiao, L. Wei, T. Bouchenot, A.P. Gordon, Y. Fink, Y. Bai, and R.S. Hoy, *Controlled fragmentation of multimaterial fibres and films via polymer cold-drawing.* Nature, 2016.

103. H. Lu, X. Wang, Y. Yao, J. Gou, D. Hui, B. Xu, and Y. Fu, *Synergistic effect of siloxane modified aluminum nanopowders and carbon fiber on electrothermal efficiency of polymeric shape memory nanocomposite.* Composites Part B: Engineering, 2015. **80**: p. 1-6.

104. M.C. Everhart, J.B. Stahl, E.W. Traxler, and E. Havens. *Shape memory polymer configurative tooling*. in *Smart Structures and Materials*. 2004. International Society for Optics and Photonics.

105. W. Sokolowski, A. Metcalfe, S. Hayashi, L.H. Yahia, and J. Raymond, *Medical applications of shape memory polymers.* Biomedical Materials, 2007. **2**(1): p. S23.

106. J. Sun, Q. Guan, Y. Liu, and J. Leng, *Morphing aircraft based on smart materials and structures: A state-of-the-art review.* Journal of Intelligent Material Systems and Structures, 2016: p. 1045389X16629569.

107. S.S. Mahapatra, S.K. Yadav, H.J. Yoo, M.S. Ramasamy, and J.W. Cho, *Tailored and strong electro-responsive shape memory actuation in carbon nanotube-reinforced hyperbranched polyurethane composites.* Sensors and Actuators B: Chemical, 2014. **193**: p. 384-390.

108. H. Lu, Y. Liu, J.J. Gou, J. Leng, and S. Du, *Surface coating of multi-walled carbon nanotube nanopaper on shape-memory polymer for multifunctionalization.* Composites Science and Technology, 2011. **71**(11): p. 1427-1434.

109. K. Yu, Y. Liu, and J. Leng, *Shape memory polymer/CNT composites and their microwave induced shape memory behaviors.* RSC Advances, 2014. **4**(6): p. 2961-2968.

110. M.F. De Volder, S.H. Tawfick, R.H. Baughman, and A.J. Hart, *Carbon nanotubes: present and future commercial applications.* Science, 2013. **339**(6119): p. 535-539.

111. J.R. Wood, Q. Zhao, M.D. Frogley, E.R. Meurs, A.D. Prins, T. Peijs, D.J. Dunstan, and H.D. Wagner, *Carbon nanotubes: from molecular to macroscopic sensors.* Physical Review B, 2000. **62**(11): p. 7571.

112. W. Qiu, Q. Li, Z.-K. Lei, Q.-H. Qin, W.-L. Deng, and Y.-L. Kang, *The use of a carbon nanotube sensor for measuring strain by micro-Raman spectroscopy.* Carbon, 2013. **53**: p. 161-168.

113. M. Amjadi, Y.J. Yoon, and I. Park, *Ultra-stretchable and skin-mountable strain sensors using carbon nanotubes? Ecoflex nanocomposites.* Nanotechnology, 2015. **26**(37): p. 375501.

114. D. Ding, H. Wei, J. Zhu, Q. He, X. Yan, S. Wei, and Z. Guo, *Strain sensitive polyurethane nanocomposites reinforced with multiwalled carbon nanotubes.* Energy and Environment Focus, 2014. **3**(1): p. 85-93.

115. C.-X. Liu and J.-W. Choi, *Patterning conductive PDMS nanocomposite in an elastomer using microcontact printing.* Journal of Micromechanics and Microengineering, 2009. **19**(8): p. 085019.

116. T. Sekitani, H. Nakajima, H. Maeda, T. Fukushima, T. Aida, K. Hata, and T. Someya, *Stretchable active-matrix organic light-emitting diode display using printable elastic conductors.* Nature materials, 2009. **8**(6): p. 494-499.

117. M. Vatani, M. Vatani, and J. Choi, *Multi-layer stretchable pressure sensors using ionic liquids and carbon nanotubes.* Applied Physics Letters, 2016. **108**(6): p. 061908.

118. D. Lee, H.P. Hong, C.J. Lee, C.W. Park, and N.K. Min, *Microfabrication and characterization of spray-coated single-wall carbon nanotube film strain gauges.* Nanotechnology, 2011. **22**(45): p. 455301.

119. O.-S. Kwon, H. Kim, H. Ko, J. Lee, B. Lee, C.-H. Jung, J.-H. Choi, and K. Shin, *Fabrication and characterization of inkjet-printed carbon nanotube electrode patterns on paper.* Carbon, 2013. **58**: p. 116-127.

120. P. Chen, H. Chen, J. Qiu, and C. Zhou, *Inkjet printing of single-walled carbon nanotube/RuO2 nanowire supercapacitors on cloth fabrics and flexible substrates.* Nano Research, 2010. **3**(8): p. 594-603.

121. N. Lu, C. Lu, S. Yang, and J. Rogers, *Highly Sensitive Skin-Mountable Strain Gauges Based Entirely on Elastomers.* Advanced Functional Materials, 2012. **22**(19): p. 4044-4050.

122. X. Song, S. Liu, Z. Gan, Q. Lv, H. Cao, and H. Yan, *Controllable fabrication of carbon nanotube-polymer hybrid thin film for strain sensing.* Microelectronic Engineering, 2009. **86**(11): p. 2330-2333.

123. T. Kim, H. Song, J. Ha, S. Kim, D. Kim, S. Chung, J. Lee, and Y. Hong, *Inkjet-printed stretchable single-walled carbon nanotube electrodes with excellent mechanical properties.* Applied Physics Letters, 2014. **104**(11): p. 113103.

124. C. Farcau, N.M. Sangeetha, H. Moreira, B. Viallet, J. Grisolia, D. Ciuculescu-Pradines, and L. Ressier, *High-sensitivity strain gauge based on a single wire of gold nanoparticles fabricated by stop-and-go convective self-assembly.* ACS nano, 2011. **5**(9): p. 7137-7143.

125. G. Choi, J.W. Lee, J.Y. Cha, Y.-J. Kim, Y.-S. Choi, M.J. Schulz, C.K. Moon, K.T. Lim, S.Y. Kim, and I. Kang, *A Spray-On Carbon Nanotube Artificial Neuron Strain Sensor for Composite Structural Health Monitoring.* Sensors, 2016. **16**(8): p. 1171.

126. W. Obitayo and T. Liu, *A review: carbon nanotube-based piezoresistive strain sensors.* Journal of Sensors, 2012. **2012**.

127. L. Supriya, S. Unal, T.E. Long, and R.O. Claus, *Assembly of conductive Au films on poly (urethane urea) elastomers using a solution-based approach.* Chemistry of materials, 2006. **18**(10): p. 2506-2512.

128. J.C. Anike, A. Bajar, and J.L. Abot, *Time-dependent effects on the coupled mechanical-electrical response of carbon nanotube yarns under tensile loading.* C, 2016. **2**(1): p. 3.

129. Q. Fan, Z. Qin, S. Gao, Y. Wu, J. Pionteck, E. Mäder, and M. Zhu, *The use of a carbon nanotube layer on a polyurethane multifilament substrate for monitoring strains as large as 400%*. Carbon, 2012. **50**(11): p. 4085-4092.

130. C. Mattmann, F. Clemens, and G. Tröster, *Sensor for measuring strain in textile.* Sensors, 2008. **8**(6): p. 3719-3732.

131. L.M. Castano and A.B. Flatau, *Smart fabric sensors and e-textile technologies: a review.* Smart Materials and Structures, 2014. **23**(5): p. 053001.

132. R.-H. Kim, D.-H. Kim, J. Xiao, B.H. Kim, S.-I. Park, B. Panilaitis, R. Ghaffari, J. Yao, M. Li, and Z. Liu, *Waterproof AlInGaP optoelectronics on stretchable substrates with applications in biomedicine and robotics.* Nature materials, 2010. **9**(11): p. 929-937.

133. D. Son, J. Lee, S. Qiao, R. Ghaffari, J. Kim, J.E. Lee, C. Song, S.J. Kim, D.J. Lee, and S.W. Jun, *Multifunctional wearable devices for diagnosis and therapy of movement disorders.* Nature Nanotechnology, 2014. **9**(5): p. 397-404.

134. S. Park, M. Vosguerichian, and Z. Bao, *A review of fabrication and applications of carbon nanotube film-based flexible electronics.* Nanoscale, 2013. **5**(5): p. 1727-1752.

135. S. Jung, J.H. Kim, J. Kim, S. Choi, J. Lee, I. Park, T. Hyeon, and D.H. Kim, *Reverse-Micelle-Induced Porous Pressure-Sensitive Rubber for Wearable Human–Machine Interfaces.* Advanced Materials, 2014. **26**(28): p. 4825-4830.

136. H. Zhao and J. Bai, *Highly Sensitive Piezo-Resistive Graphite Nanoplatelet–Carbon Nanotube Hybrids/Polydimethylsilicone Composites with Improved Conductive Network Construction.* ACS applied materials & interfaces, 2015. **7**(18): p. 9652-9659.

137. Y. Tang, Z. Zhao, H. Hu, Y. Liu, X. Wang, S. Zhou, and J. Qiu, *Highly Stretchable and Ultrasensitive Strain Sensor Based on Reduced Graphene Oxide Microtubes–Elastomer Composite.* ACS applied materials & interfaces, 2015. **7**(49): p. 27432-27439.

138. M. Amjadi, A. Pichitpajongkit, S. Lee, S. Ryu, and I. Park, *Highly stretchable and sensitive strain sensor based on silver nanowire–elastomer nanocomposite.* ACS nano, 2014. **8**(5): p. 5154-5163.

139. H. Tian, Y. Shu, Y.-L. Cui, W.-T. Mi, Y. Yang, D. Xie, and T.-L. Ren, *Scalable fabrication of high-performance and flexible graphene strain sensors.* Nanoscale, 2014. **6**(2): p. 699-705.

140. Y. Wang, L. Wang, T. Yang, X. Li, X. Zang, M. Zhu, K. Wang, D. Wu, and H. Zhu, *Wearable and highly sensitive graphene strain sensors for human motion monitoring.* Advanced Functional Materials, 2014. **24**(29): p. 4666-4670.

141. D.J. Lipomi, M. Vosgueritchian, B.C. Tee, S.L. Hellstrom, J.A. Lee, C.H. Fox, and Z. Bao, *Skin-like pressure and strain sensors based on transparent elastic films of carbon nanotubes.* Nature nanotechnology, 2011. **6**(12): p. 788-792.

142. X. Wang, J. Sparkman, and J. Gou, *Strain sensing of printed carbon nanotube sensors on polyurethane substrate with spray deposition modeling.* Composites Communications, 2017. **3**: p. 1-6.

143. D. Maji, S. Lahiri, and S. Das, *Study of hydrophilicity and stability of chemically modified PDMS surface using piranha and KOH solution.* Surface and Interface analysis, 2012. **44**(1): p. 62-69.

144. K.-S. Koh, J. Chin, J. Chia, and C.-L. Chiang, *Quantitative studies on PDMS-PDMS interface bonding with piranha solution and its swelling effect.* Micromachines, 2012. **3**(2): p. 427-441.

145. A. Shimoni, S. Azoubel, and S. Magdassi, *Inkjet printing of flexible high-performance carbon nanotube transparent conductive films by "coffee ring effect".* Nanoscale, 2014. **6**(19): p. 11084-11089.

146. M. Amjadi, K.U. Kyung, I. Park, and M. Sitti, *Stretchable, Skin-Mountable, and Wearable Strain Sensors and Their Potential Applications: A Review.* Advanced Functional Materials, 2016.

147. B. De Vivo, P. Lamberti, G. Spinelli, V. Tucci, L. Vertuccio, and V. Vittoria, *Simulation and experimental characterization of polymer/carbon nanotubes composites for strain sensor applications.* Journal of Applied Physics, 2014. **116**(5): p. 054307.

148. B.E. Schubert and D. Floreano, *Variable stiffness material based on rigid low-melting-point-alloy microstructures embedded in soft poly (dimethylsiloxane)(PDMS).* Rsc Advances, 2013. **3**(46): p. 24671-24679.

149. F. Wu and H. Cheng, *Structure and thermal expansion of multi-walled carbon nanotubes before and after high temperature treatment.* Journal of Physics D: Applied Physics, 2005. **38**(24): p. 4302.

150. M. Barberio, M. Camarca, P. Barone, A. Bonanno, A. Oliva, and F. Xu, *Electric resistivity of multi-walled carbon nanotubes at high temperatures.* Surface science, 2007. **601**(13): p. 2814-2818.

151. C.-X. Liu and J.-W. Choi, *Analyzing resistance response of embedded PDMS and carbon nanotubes composite under tensile strain.* Microelectronic Engineering, 2014. **117**: p. 1-7.

152. P.R. Bandaru, *Electrical properties and applications of carbon nanotube structures.* Journal of nanoscience and nanotechnology, 2007. **7**(4-5): p. 1239-1267.

153. H. Lu and W.M. Huang, *Synergistic effect of self-assembled carboxylic acid-functionalized carbon nanotubes and carbon fiber for improved electro-activated polymeric shape-memory nanocomposite.* Applied Physics Letters, 2013. **102**(23): p. 231910.

154. X. Guan, G.-Q. Zheng, K. Dai, C. Liu, X. Yan, C. Shen, and Z. Guo, *Carbon Nanotubes-Adsorbed Electrospun PA66 Nanofiber Bundles with Improved Conductivity and Robust Flexibility.* ACS applied materials & interfaces, 2016.

155. W. Zhao, M. Li, Z. Zhang, and H. Peng. *Carbon nanotube based composites film heater for de-icing application*. in *14th European Conference on Composite Materials*. 2010.

156. R. Musat and E. Helerea. *Characteristics of the PTC heater used in automotive HVAC systems*. in *Doctoral Conference on Computing, Electrical and Industrial Systems*. 2010. Springer.

157. D. Janas and K.K. Koziol, *Rapid electrothermal response of high-temperature carbon nanotube film heaters.* Carbon, 2013. **59**: p. 457-463.

158. J. Wei, J. Wang, S. Su, S. Wang, J. Qiu, Z. Zhang, G. Christopher, F. Ning, and W. Cong, *3D printing of an extremely tough hydrogel.* Rsc Advances, 2015. **5**(99): p. 81324-81329.

159. X. Wang, M. Jiang, Z. Zhou, J. Gou, and D. Hui, *3D printing of polymer matrix composites: A review and prospective.* Composites Part B: Engineering.

160. L. Yang, R. Zhang, D. Staiculescu, C. Wong, and M.M. Tentzeris, *A novel conformal RFID-enabled module utilizing inkjet-printed antennas and carbon nanotubes for gas-detection applications.* IEEE Antennas and Wireless Propagation Letters, 2009. **8**: p. 653-656.

161. J.-W. Song, J. Kim, Y.-H. Yoon, B.-S. Choi, J.-H. Kim, and C.-S. Han, *Inkjet printing of single-walled carbon nanotubes and electrical characterization of the line pattern.* Nanotechnology, 2008. **19**(9): p. 095702.

162. P. Chen, H. Chen, J. Qiu, and C. Zhou, *Inkjet printing of single-walled carbon nanotube/RuO 2 nanowire supercapacitors on cloth fabrics and flexible substrates.* Nano Research, 2010. **3**(8): p. 594-603.

163. H. Lu, Y. Liu, J. Gou, J. Leng, and S. Du, *Electrical properties and shape-memory behavior of self-assembled carbon nanofiber nanopaper incorporated with shape-memory polymer.* Smart materials and Structures, 2010. **19**(7): p. 075021.

164. J.J. Bae, S.C. Lim, G.H. Han, Y.W. Jo, D.L. Doung, E.S. Kim, S.J. Chae, T.Q. Huy, N. Van Luan, and Y.H. Lee, *Heat dissipation of transparent graphene defoggers.* Advanced Functional Materials, 2012. **22**(22): p. 4819-4826.

165. J. Li, J. Liang, X. Jian, W. Hu, J. Li, and Q. Pei, *A Flexible and Transparent Thin Film Heater Based on a Silver Nanowire/Heat-resistant Polymer Composite.* Macromolecular Materials and Engineering, 2014. **299**(11): p. 1403-1409.

166. P. Liu, L. Liu, K. Jiang, and S. Fan, *Carbon-Nanotube-Film Microheater on a Polyethylene Terephthalate Substrate and Its Application in Thermochromic Displays.* Small, 2011. **7**(6): p. 732-736.

167. Y. Yap and W. Yeong, *Shape recovery effect of 3D printed polymeric honeycomb: This paper studies the elastic behaviour of different honeycomb structures produced by PolyJet technology.* Virtual and Physical Prototyping, 2015. **10**(2): p. 91-99.

168. R. Stewart, *At the core of lightweight composites.* Reinforced Plastics, 2009. **53**(3): p. 30-35.

169. R.D. Schultheiss, *Method and apparatus for producing honeycomb structure*. 1966, Google Patents.

170. X. Wang, M. Jiang, Z. Zhou, J. Gou, and D. Hui, *3D printing of polymer matrix composites: A review and prospective.* Composites Part B: Engineering, 2017. **110**: p. 442-458.

171. S.P. Joshi, Z. Tidwell, W.A. Crossley, and S. Ramakrishnan, *Comparison of morphing wing strategies based upon aircraft performance impacts.* sea, 2004. **7**: p. 2.32.

172. D.H. Lee and T.A. Weisshaar, *Aeroelastic studies on a folding wing configuration.* AIAA Paper, 2005. **1996**: p. 2005.

173. X. Wang, J. Sparkman, and J. Gou, *Electrical actuation and shape memory behavior of polyurethane composites incorporated with printed carbon nanotube layers.* Composites Science and Technology, 2017.

174. Z. Tang, D. Sun, D. Yang, B. Guo, L. Zhang, and D. Jia, *Vapor grown carbon nanofiber reinforced bio-based polyester for electroactive shape memory performance.* Composites Science and Technology, 2013. **75**: p. 15-21.

175. X. Feng, G. Zhang, S. Zhuo, H. Jiang, J. Shi, F. Li, and H. Li, *Dual responsive shape memory polymer/clay nanocomposites.* Composites Science and Technology, 2016. **129**: p. 53-60.

176. H. Shen, Y. Xu, F. Liang, J. Gou, and B. Mabbott, *Recovery torque modeling of carbon fiber reinforced shape memory polymer nanocomposites.* Applied Physics Letters, 2013. **103**(20): p. 201903.

APPENDIX: LIST OF RELEVANT PUBLICATIONS

This dissertation is based in part on the following publications:

1. H. Lu, X. Wang, Y. Yao, J. Gou, D. Hui, B. Xu, and Y. Fu, Synergistic Effect of Siloxane Modified Aluminum Nanopowders and Carbon Fiber on Electrothermal Efficiency of Polymeric Shape Memory Nanocomposite. Composites Part B: Engineering, 2015.
2. X. Wang, J. Sparkman, and J. Gou, Strain sensing of printed carbon nanotube sensors on polyurethane substrate with spray deposition modeling. Composites Communications, 2017. 3: p. 1-6.
3. X. Wang, M. Jiang, Z. Zhou, J. Gou, and D. Hui, 3D printing of polymer matrix composites: A review and prospective. Composites Part B: Engineering.
4. X. Wang, J. Sparkman, and J. Gou, Electrical actuation and shape memory behavior of polyurethane composites incorporated with printed carbon nanotube layers. Composites Science and Technology, 2017.